

**Study of the Effects of Wind Power and
Vortex-Induced Vibrations to Establish
Fatigue Design Criteria for High-Mast Poles**

Jay Puckett, Ph.D., P.E.
Professor

Rebecca Johnson
Graduate Research Assistant

Michael Barker, Ph.D., P.E.
Professor

Civil and Architectural Engineering
University of Wyoming

August 2011

Acknowledgements

The authors would like to thank the Mountain-Plains Consortium for their support of this work. We would like to thank the several department of transportation for their cooperation and collaboration in sharing inspection data.

Disclaimer

The contents of this report reflect the views of the authors, who are responsible for the facts and the accuracy of the information presented. This document is disseminated under the sponsorship of the Department of Transportation, University Transportation Centers Program, in the interest of information exchange. The United States Government assumes no liability for the contents or use thereof.

North Dakota State University does not discriminate on the basis of age, color, disability, gender expression/identity, genetic information, marital status, national origin, public assistance status, sex, sexual orientation, status as a U.S. veteran, race or religion. Direct inquiries to the Vice President for Equity, Diversity and Global Outreach, 205 Old Main, (701)231-7708.

ABSTRACT

Traffic signal and high-mast poles are used by transportation agencies to control and illuminate intersections; their structural design is governed by national specifications. High-mast poles are luminaire supports located near highway interchanges that range from 80 to 180 feet in height. These tall flexible structures are susceptible to wind vibration which may lead to fatigue cracking near discontinuities and base connections.

In a previous related study conducted by the University of Wyoming (Phase I), fatigue cracking of traffic signal poles was determined to be related to the average wind speed (Price 2009). However, high-mast data did not indicate the same direct average wind speed fatigue cracking relationship behavior. In this continuing work, the research goal is to gain a more complete understanding of the relation between wind speed and high-mast pole cracking. Surveys were sent to more state bridge engineers to further the data collection of Phase I.

It is hypothesized that the cracking of high-mast poles is caused not as much by direct wind speed, rather it is caused by the resonant displacements of vortex-induced vibrations (VIV). The Canadian Standards Association (CSA) code models VIV and was, therefore, selected to complete Phase II of this research. It was used to create a spreadsheet which predicts amplitudes of vibration of a high-mast pole located in Laramie, Wyoming. The output data were compared to field data of a local pole. This sheet was further used to predict base stresses and fatigue life as a function of local wind data.

The Phase II analysis process produced high-amplitude predictions compared with local field data; therefore, self-limiting concepts were studied in Phase III. A self-limiting concept for an oscillating member hypothesizes that the natural properties of the pole and the fluid interaction keep amplifications under a predictable maximum.

TABLE OF CONTENTS

1. INTRODUCTION.....	1
1.1 Background	1
1.2 Document Organization	2
1.2.1 Phase I: Fatigue Damage in Traffic-Signal Poles Related to Wind Power Potential	2
1.2.2 Phase II: Estimating Vortex-Induced Fatigue in High-Mast Poles	2
1.2.3 Phase III: Self-Limiting Vortex-Induced Vibrations.....	2
2. PHASE I: FATIGUE DAMAGE IN LTS RELATED TO WIND POWER.....	3
2.1 Wind Power Classification Maps	3
2.2 University of Wyoming Study	5
2.3 Additional Data	6
2.3.1 Iowa.....	6
2.3.2 Pennsylvania	7
2.3.3 Delaware	8
2.3.4 Nevada	8
2.3.5 Idaho.....	8
2.3.6 Missouri	9
2.3.7 Florida	10
2.3.8 Colorado.....	11
2.4 Analysis of Additional Data	12
2.4.1 Reliability of WPC Estimation.....	13
2.5 Summary and Recommendations	13
3. PHASE II: ESTIMATING VORTEX-INDUCED FATIGUE IN HIGH-MAST POLES.....	15
3.1 Vortex-Induced Vibrations	15
3.1.1 Definition	15
3.1.2 Iowa State University Study.....	17
3.1.3 University of Wyoming Study	18
3.2 AASHTO Specifications	20
3.3 CSA Specifications.....	21
3.4 Application of CSA Specifications	23
3.4.1 Input	24
3.4.2 Looping Process	25
3.5 Estimated Fatigue Life	27
3.6 Example Computations for Laramie Pole	29
3.6.1 Displacement Estimation	30
3.6.2 Fatigue Life Estimation.....	35
3.6.3 Comparison to NCHRP 469 Method	36
3.7 Summary and Recommendations	38

4. PHASE III: SELF-LIMITING VORTEX-INDUCED VIBRATION	39
4.1 Self-Limiting Vibrations	39
4.2 Conceptual Framework for Design	39
4.2.1 High-Mast Pole Self-Limiting Dimensionless Variables	42
4.3 Theoretical Models	44
4.4 Experimental Research	44
4.4.1 Empirical Models	49
4.4.2 Empirical Models for Laramie and Oklahoma Poles	51
4.4.3 Stress Range Estimations from Self-Limiting VIV Amplitudes	52
4.5 Summary and Recommendations	54
5. SUMMARY AND RECOMMENDATIONS	55
5.1 Summary	55
5.2 Recommendations	55
6. BIBLIOGRAPHY	57
7. APPENDIX	59
7.1 Wind Power Classification Maps	59
7.2 Laramie High-Mast Pole Specifications	66
7.3 Oklahoma High-Mast Pole Specifications	67
7.4 CSA Canadian Highway Bridge Design Code Relevant Sections	68
7.5 CSA Canadian Highway Bridge Design Commentary Relevant Sections	73

LIST OF TABLES

Table 2.1	Classes of Wind Power Density at 10m and 50m ^a (Elliott, Holladay, Barchet, Foote, & Sandusky, 1986)	3
Table 2.2	Summary of Cracked Pole WPC	12
Table 3.1	Natural Frequencies of Wyoming Pole (Ahearn, 2010)	20
Table 3.2	Damping Ratios of Wyoming Pole (Ahearn, 2010)	20
Table 3.3	Local High-Mast Pole General Values	30
Table 3.4	Local High-Mast Pole Dynamic Values	30
Table 3.5	T1 Results for Laramie Pole	32
Table 3.6	T2 Results for Laramie Pole	35
Table 3.7	Fatigue Life Estimations for Laramie Pole	36
Table 4.1	Dimensionless Variables	41
Table 4.2	Separate Variables	41
Table 4.3	Mass Ratios for Laramie Pole	42
Table 4.4	Mass Ratios for Oklahoma Pole	42
Table 4.5	Skop-Griffin Values for Laramie Pole	43
Table 4.6	Skop-Griffin Values for Oklahoma Pole	43
Table 4.7	Skop-Griffin Values for Critical Height of Laramie Pole	43
Table 4.8	Skop-Griffin Values for Critical Height of Oklahoma Pole	43
Table 4.9	Peak Amplitude Ratio Data (Williamson & Govardhan, 2004)	48

LIST OF FIGURES

Figure 1.1 S-N Curve (AASHTO, 2010)..... 1

Figure 2.1 Certainty Ratings of WPC in the United States (Elliott, Holladay, Barchet, Foote, & Sandusky, 1986)..... 5

Figure 2.2 Mast Arm Cracking Probability (Price, 2009) 6

Figure 2.3 Iowa High-Mast Cracking Locations 7

Figure 2.4 Pennsylvania Traffic-Signal Pole Cracking Locations 8

Figure 2.5 Idaho Traffic-Signal Cracking Locations..... 9

Figure 2.6 Missouri Traffic-Signal Crack Locations..... 10

Figure 2.7 Florida High-Mast Cracking Locations..... 11

Figure 2.8 Colorado LTS Cracking Locations 12

Figure 3.1 Regimes of fluid flow across circular cylinder (Lienard, 1966) 16

Figure 3.2 Strouhal number vs. Reynolds number (Techet, 2005)..... 17

Figure 3.3 Vortex shedding frequency with wind velocity 17

Figure 3.4 Modes of Vibration 18

Figure 3.5 Location of Laramie High-Mast Poles 19

Figure 3.6 Typical Pluck Test Acceleration Data (Ahearn, 2010) 19

Figure 3.7 Length of in-phase VIV on a high-mast pole..... 22

Figure 3.8 Transfer Method Process..... 24

Figure 3.9 Mode Shapes for Transfer Sheet 25

Figure 3.10 Transfer Sheet Process 27

Figure 3.11 Laramie Wind Data Distribution..... 28

Figure 3.12 Mode 1 Results for T1 of Laramie Pole..... 31

Figure 3.13 Mode 2 Results for T1 of Laramie Pole..... 31

Figure 3.14 Mode 3 Results for T1 of Laramie Pole..... 32

Figure 3.15 Field Data for Laramie Pole (Ahearn, 2010)..... 33

Figure 3.16 Mode 1 Results for T2 of Laramie Pole..... 34

Figure 3.17	Mode 2 Results for T2 of Laramie Pole.....	34
Figure 3.18	Mode 3 Results for T2 of Laramie Pole.....	35
Figure 4.1	Basic System Variables.....	39
Figure 4.2	Basic System Variables (continued)	40
Figure 4.3	Basic System Variables (continued)	40
Figure 4.4	Griffin-Plot with Early Skop-Griffin Parameter (Griffin, 1980).....	45
Figure 4.5	Displacement Amplitude for Flexible Cylinders in a Wind Tunnel (Griffin, 1984).....	46
Figure 4.6	Griffin-Plot with Data (Williamson & Govardhan, 2004)	47
Figure 4.7	Maximum Amplitude of VIV as a function of Damping (Blevins, 1984)	49
Figure 4.8	Empirical Models for Laramie High-Mast.....	51
Figure 4.9	Empirical Models for Oklahoma High-Mast	52
Figure 4.10	Empirical Model Peak Base Stress for Laramie High-Mast	53
Figure 4.11	Empirical Model Peak Base Stress for Oklahoma High-Mast.....	53
Figure 7.1	Iowa WPC (Elliott, Holladay, Barchet, Foote, & Sandusky, 1986).....	59
Figure 7.2	Pennsylvania WPC (Elliott, Holladay, Barchet, Foote, & Sandusky, 1986).....	60
Figure 7.3	Idaho WPC (Elliott, Holladay, Barchet, Foote, & Sandusky, 1986).....	61
Figure 7.4	Missouri WPC (Elliott, Holladay, Barchet, Foote, & Sandusky, 1986).....	62
Figure 7.5	Florida WPC (Elliott, Holladay, Barchet, Foote, & Sandusky, 1986)	63
Figure 7.6	Colorado WPC (EIS, 2004).....	64
Figure 7.7	Colorado WPC (Elliott, Holladay, Barchet, Foote, & Sandusky, 1986).....	65

1. INTRODUCTION

1.1 Background

High-mast poles are used by transportation agencies to light highway intersections. Their height can range from 80 to 160 feet. Traffic signal poles and high-mast poles are susceptible to vibration from wind, which can lead to fatigue cracking. The American Association of State Highway and Transportation Officials (AASHTO) Luminaire and Traffic Signal Specifications provide provisions that must be met by the owners and manufacturers of the structures in order to ensure safety and quality of the product. Due to the failure of high-mast poles and traffic-signals in certain areas of the country, changes were made in the third edition to yield the Fourth Edition (AASHTO 2001). In some cases, these changes require an increase in size of the structure in order to provide higher fatigue resistance. The increase in size directly causes an increase in cost. Recently, the fifth edition was released, but there were few changes in this procedure (AASHTO 2009).

The failure of high-mast poles can be a result of fatigue cracks that form in the tube wall near the weld toe. Fatigue cracking occurs when the weld is subjected to cyclic loading, which can be caused by the oscillations of vortex-induced vibrations. The welds of each high-mast are given a detailed category label, A through E', which defines its fatigue resistance, including its constant-amplitude fatigue threshold (CAFT). The CAFT is the stress at which the weld can experience an infinite amount of cycles without cracking. It is determined by the loading and cracking of many welds, which are then plotted on the S-N curve to establish Figure 1.1.

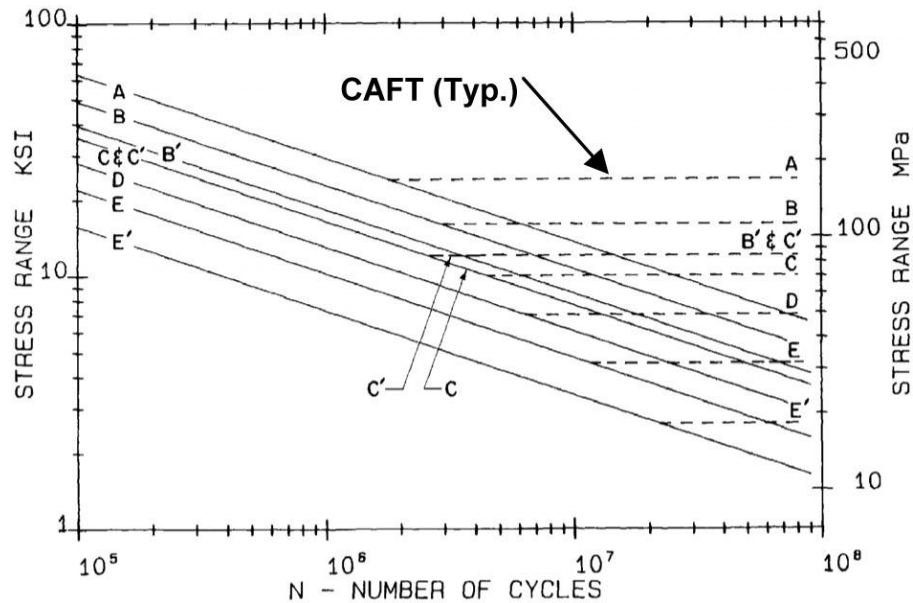


Figure 1.1 S-N Curve (AASHTO 2010)

The section is proportioned so that the stress range due to wind loads is under the CAFT resistance; thereby providing an infinite fatigue life. AASHTO 2009 is based upon this philosophy. This report is largely based upon the thesis by Johnson (2011).

1.2 Document Organization

The research presented has been developed in three phases. They are each diverse in their methods and results and are, therefore, given their own chapter for ease of reading. Each of the chapters includes a literature review and conclusion section, which are brought together at the final conclusion of the report. The following summarizes what is discussed in each phase.

1.2.1 Phase I: Fatigue Damage in Traffic-Signal Poles Related to Wind Power Potential

Phase I introduces a previous University of Wyoming (UW) study (Price 2009). Price recognized that the current AASHTO code does not vary luminaire and traffic signal (LTS) specifications based on location. He predicted that cracking is related to high wind power areas. By surveying the state bridge engineers across the country, he was able to create a database of cracking locations. These were compared to Wind Power Classification (WPC) maps, which showed that traffic-signal pole cracking is related to high WPC, but that high-mast cracking is not. Price hypothesized that high-mast cracking is related to a resonant wind speed, which can create high-stress situations. It was recommended that more data be collected to test this possibility as well as the certainty of the traffic-pole cracking prediction (Price 2009).

More surveys were sent out to state bridge engineers inquiring of LTS cracking and locations. These data were analyzed in a manner similar to Price's data and yielded similar results; cracking of traffic signal poles is directly related to high WPC, whereas cracking of high-masts is not. The investigation of cracking being caused by resonant wind speeds was further investigated in Phase II.

1.2.2 Phase II: Estimating Vortex-Induced Fatigue in High-Mast Poles

Phase II begins with a summary of the phenomenon of vortex-induced vibrations (VIV). The current specifications for the design of high-mast poles in the United States and Canada are reviewed, specifically, sections pertaining to VIV. The Canadian Standards Association (CSA) design specifications are incorporated into a computer analysis tool called a transfer sheet herein. The sheet requires input of structural, dynamic, and local wind data for the high-mast pole being analyzed. An output report is then created, which includes critical velocity, maximum displacement, base moment, and an estimation of fatigue life. This analysis tool transfer sheet is validated with data collected on a local Laramie pole from another UW Study (Ahearn 2010). The analysis tool was applied to a database of high-mast pole examples.

During the literature review of Phase II, it was discovered that there is currently much discussion on the subject of self-limiting displacement of cylindrical systems subject to such demand, which was further investigated in Phase III. This approach has not been studied previously with application to high-mast poles related to the LTS.

1.2.3 Phase III: Self-Limiting Vortex-Induced Vibrations

Phase III begins with a summary of recent research in the self-limiting displacement area, which suggests that a maximum displacement of a mass and damping system can be estimated based on structural characteristics. Several relevant empirical equations are reviewed and compared with field data. The research is split into a theoretical, experimental, and empirical approach. Possible high-mast design recommendations are discussed.

2. PHASE I: FATIGUE DAMAGE IN LTS RELATED TO WIND POWER

2.1 Wind Power Classification Maps

U.S. Wind Power Classification Maps were created through an initiative of the Federal Wind Energy Program to provide an atlas of wind power information to the country. Data collection, which began in 1979, now streams from 975 stations across the country and is housed at the National Climatic Data Center. The maps created, usually separated by state, designate a WPC to specific areas. The WPC is determined by the measured wind power density of the area, or areas nearby. Wind power density is the effective power of wind at a specific location and is proportional to the third moment of the wind speed distribution and air density. A mean wind speed is also associated with each WPC determined by, "...specifying a Rayleigh wind speed distribution and a standard sea level air density (1.22 kg/ m³)," (Elliott, Holladay, Barchet, Foote, & Sandusky 1986). Decrease in air density with elevation is accounted for by applying an increase to the mean Rayleigh speed to maintain the same wind power density. Table 2.1 contains each WPC and its associated wind power density and mean wind speed (Elliott, Holladay, Barchet, Foote, & Sandusky 1986).

Table 2.1 Classes of Wind Power Density at 10m and 50m^a (Elliott, Holladay, Barchet, Foote, & Sandusky 1986)

Wind Power Class *	10 m (33 ft)		50 m (164 ft)	
	Wind Power Density (W/m ²)	Speed ^(b) m/s (mph)	Wind Power Density (W/m ²)	Speed ^(b) m/s (mph)
1	0	0	0	0
2	100	4.4 (9.8)	200	5.6 (12.5)
3	150	5.1 (11.5)	300	6.4 (14.3)
4	200	5.6 (12.5)	400	7.0 (15.7)
5	250	6.0 (13.4)	500	7.5 (16.8)
6	300	6.4 (14.3)	600	8.0 (17.9)
7	400	7.0 (15.7)	800	8.8 (19.7)
	1000	9.4 (21.1)	2000	11.9 (26.6)

(a) Vertical extrapolation of wind speed based on the 1/7 power law.

(b) Mean wind speed is based on Rayleigh speed distribution of equivalent mean wind power density. Wind speed is for standard sea-level conditions. To maintain the same power density, speed increases 3%/1000 m (5%/5000 ft) elevation.

The reliability of WPC estimation for an area depends on three factors: the abundance and quality of wind data, the complexity of the terrain, and the geographical variability of the resource (Elliott, Holladay, Barchet, Foote, & Sandusky 1986). By these standards, each area is also designated a Certainty Rating. The Certainty Rating ranges from Rating 1: The Lowest Degree of Certainty, to Rating 4: The Highest Degree of Certainty. The Wind Energy Resource Atlas defines the degrees of certainty as follows:

Rating 1. The lowest degree of certainty.

A combination of the following conditions exists:

No data exist in the vicinity of the cell.

The terrain is highly complex.

Various meteorological and topographical indicators suggest a high level of variability of the resource within the cell.

Rating 2. A low-intermediate degree of certainty.

One of the following conditions exists:

Few or no data exist in or near the cell, but the small variability of the resource and the low complexity of the terrain suggest that the wind resource will not differ substantially from the resource in nearby areas with data.

Limited data exist in the vicinity of the cell, but the terrain is highly complex or the mesoscale variability of the resource is large.

Rating 3. A high-intermediate degree of certainty.

One of the following conditions exists:

There are limited wind data in the vicinity of the cell, but the low complexity of terrain and the small mesoscale variability of the resource indicate little departure from the wind resource in nearby areas with data.

Considerable wind data exist but in moderately complex terrain and/or in areas where moderate variability of the resource is likely to occur.

Rating 4. The highest degree of certainty.

Quantitative data exist at exposed sites in the vicinity of the cell and can be confidently applied to exposed areas in the cell because of the low complexity of terrain and low spatial variability of the resource.

(Elliott, Holladay, Barchet, Foote, & Sandusky 1986)

Figure 2.1 shows the Certainty Ratings for WPC estimations across the United States. Lower certainty ratings are more common in the western United States due to the lack of data collection and complexity of terrain. Even highly populated areas, such as San Francisco, California, and Denver, Colorado have lower certainty ratings because of the, "...large spatial variability in the wind resource," (Elliott, Holladay, Barchet, Foote, & Sandusky 1986).

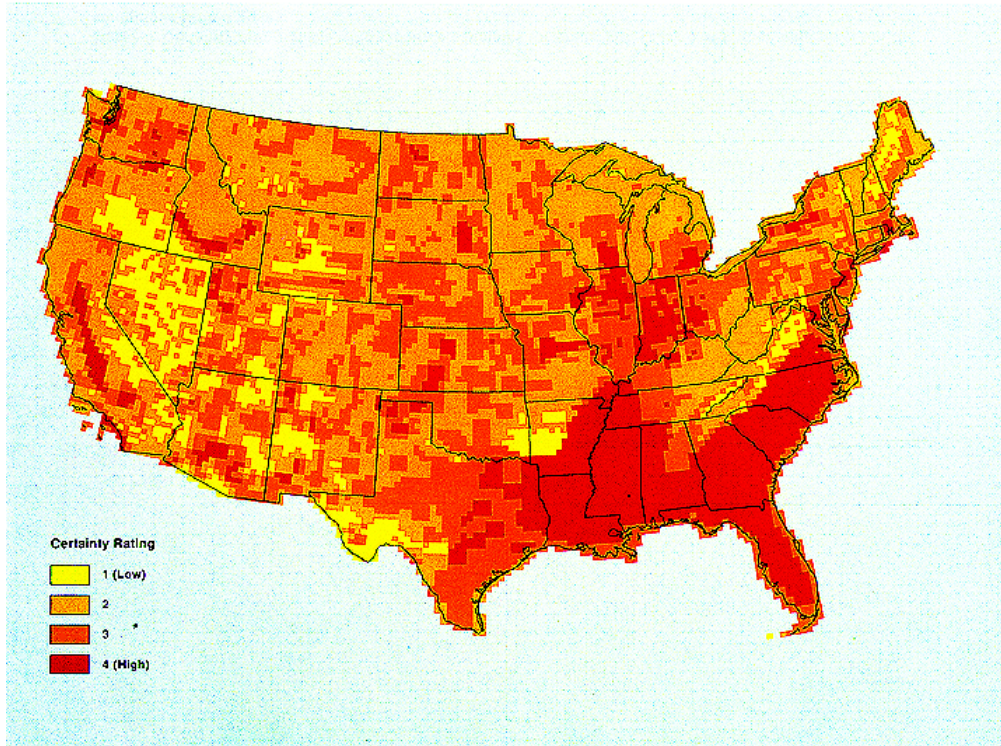


Figure 2.1 Certainty Ratings of WPC in the United States (Elliott, Holladay, Barchet, Foote, & Sandusky 1986)

2.2 University of Wyoming Study

In a previous study conducted by the UW (Phase I), data were collected to validate the use of wind power maps to predict fatigue damage of traffic signals. In order to collect national data, surveys were sent to state bridge engineers inquiring about failed traffic signals and high masts. Other information was also requested, such as structure age, length, and diameter. Twenty responses were received. Only some contained detailed data as many states are just beginning formal inspection programs. The states whose data were analyzed were Wyoming, Kansas, Michigan, New Mexico, and Iowa. Wyoming, Alaska, Kansas, and Michigan provided the most complete sets of data, which included cracking descriptions, locations, and structural details.

The results showed both WPC and age were correlating factors to fatigue cracking of the traffic-signals. However, Price stated, “The conclusions and recommendations presented herein are based on the limited data samples collected and should be verified through additional research with additional data.” The results are summarized in Figure 2.2. Note that the points in each wind power class represent many data points (Price 2009).

The objective of the study was to provide recommendations of change to the AASHTO requirements. One recommendation was to create a national database for all cantilever structures to continue the collection of data. More important was the recommendation that would allow areas with a lower wind speed to be placed in an additional fatigue category that would require more economically sized traffic-signal poles. That is, areas with lower average wind speeds would not require the same size traffic signals as those with high average wind speeds, or perhaps the fatigue limit state could be rationally eliminated from concern.

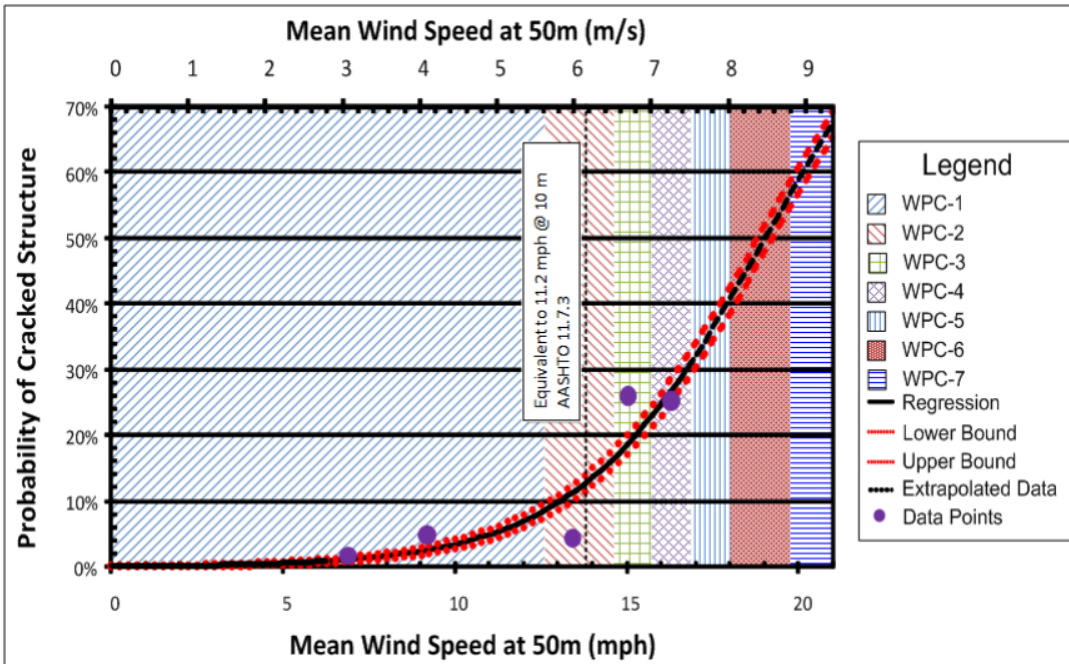


Figure 2.2 Mast Arm Cracking Probability (Price 2009)

During Phase I, 700 high-mast poles inspection reports were collected along with the traffic-signal pole reports. The reports were analyzed in the same way; however, the high-mast poles did not show the same direct relationship of fatigue to high WPC as the traffic signals. Therefore, the recommendations to AASHTO for the traffic-signal poles could not be given for the high-mast structures. It has been hypothesized that the cracking of high-mast poles is caused by the phenomena of vortex shedding, which is not caused by high velocity winds (Chang, Phares, Sarkar, & Wipf 2009). More data were needed in order to further research any connection of fatigue cracking in high-mast poles to WPC. Therefore, in this current study, more surveys were sent to state bridge engineers. These results are elaborated in Section 0.

2.3 Additional Data

To continue the data collection of Phase I, surveys were re-sent to states that failed to reply to Price. Data were received back from Iowa, Pennsylvania, Delaware, Nevada, Idaho, Missouri, Florida, and Colorado. Full reports, which include pole locations and cracking types, were received from Idaho, Missouri, Florida and Colorado; whereas, only brief summaries were received from the other states.

2.3.1 Iowa

Mr. Brakke (personal communication, July 23, 2009), a member of the Iowa Department of Transportation (IADOT), responded with a summary email giving information on cracking in high-mast poles in the state. The email did not contain information on cracking of traffic signal arms. The IADOT owns 233 high-mast poles statewide, each vary from 100 to 180 feet tall. Of the poles, 197 are made from weathered steel and 36 are galvanized. A 140-foot pole collapsed near Sioux City in November of 2003, along with the finding of 17 other cracked high masts in the area. Three cracked poles were located near Clear Lake. Figure 2.3 illustrates the locations of these cracking locations.

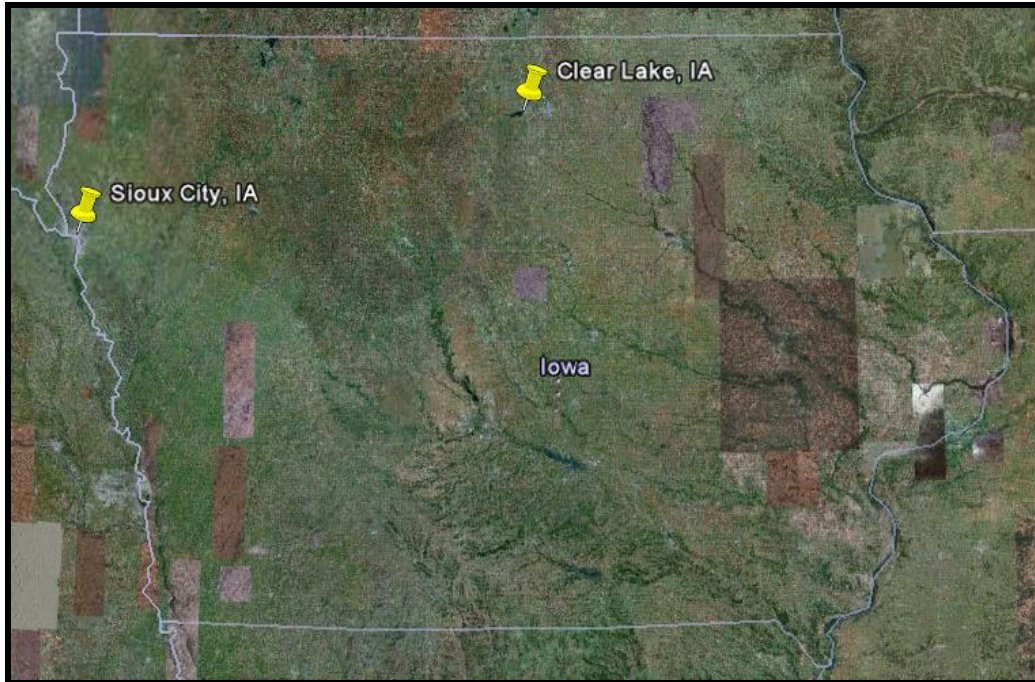


Figure 2.3 Iowa High-Mast Cracking Locations

2.3.2 Pennsylvania

Mr. Gordon (personal communication, September 11, 2009), of the Pennsylvania DOT, responded with a summary email giving information on cracking in both high-mast and traffic-signal poles. While the state does not have an inspection program in place, two traffic-signal pole cracks have been documented. The first crack location described by Gordon occurred in December, 2003. It was a traffic-signal pole located in Hazelton. The cracking was, "...considered to be caused by fatigue and was likely a result of a wall thickness which was too thin." The second cracking location was on a traffic-signal pole located in Bedford. As described by Gordon, the pole was, "...in service for only a few months and suffered an anchor bolt failure in December of 2008. The pole's anchor bolts experienced fatigue due to extensive galloping, which was not reported to the designers." Figure 2.4 is a map sent by Gordon, which illustrates the two traffic-signal failures with black ovals. It was reported that there have been no high-mast pole fatigue cracking.

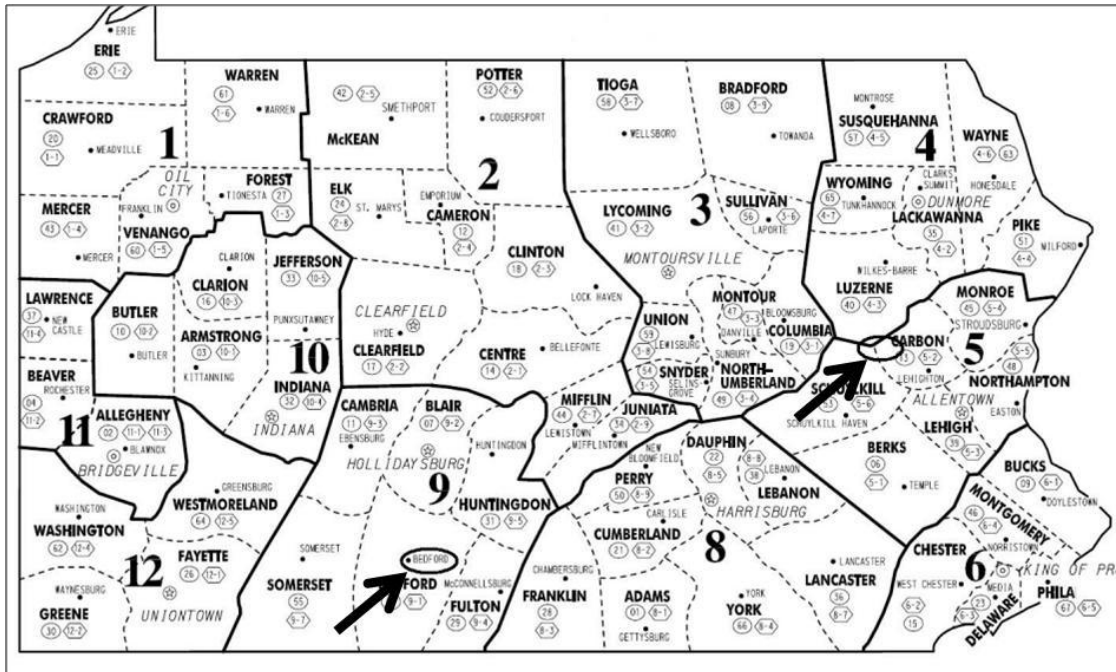


Figure 2.4 Pennsylvania Traffic-Signal Pole Cracking Locations

2.3.3 Delaware

Mr. Arndt (personal communication, July 23, 2009), of the Delaware DOT, responded with a summary email giving information on cracking in both high-mast and traffic-signal poles. There were no cracks reported for traffic-signal poles. Arndt predicts that this is due to the frequent changing of the poles and the state’s use of shorter arms for the traffic-signal poles, which reduces the lever arm. Of the 150 high-mast poles across the state, Arndt reports that most are in relatively good condition.

2.3.4 Nevada

Mr. Stefonowicz (personal communication, August 5, 2009), of the Nevada DOT, responded with a summary email giving information on cracking in both high-mast and traffic-signal poles. Stefonowicz reported that there has been no fatigue cracking for either type of luminaire. He also stated, “Due to the lack of such issues, we have been hesitant to adopt the fatigue design requirements for all of our structures. We’ll certainly be interested in the results of your study.”

2.3.5 Idaho

Collins Engineers, Inc. (personal communication, February 4, 2010) performs inspections on the high-mast and traffic-signal poles in Idaho. They sent a sheet with cracking information for both, which included crack type and location. There was no cracking reported for the high-mast poles inspected. The locations of traffic-signal pole cracking were mapped onto Google Earth, and are illustrated in Figure 2.5.

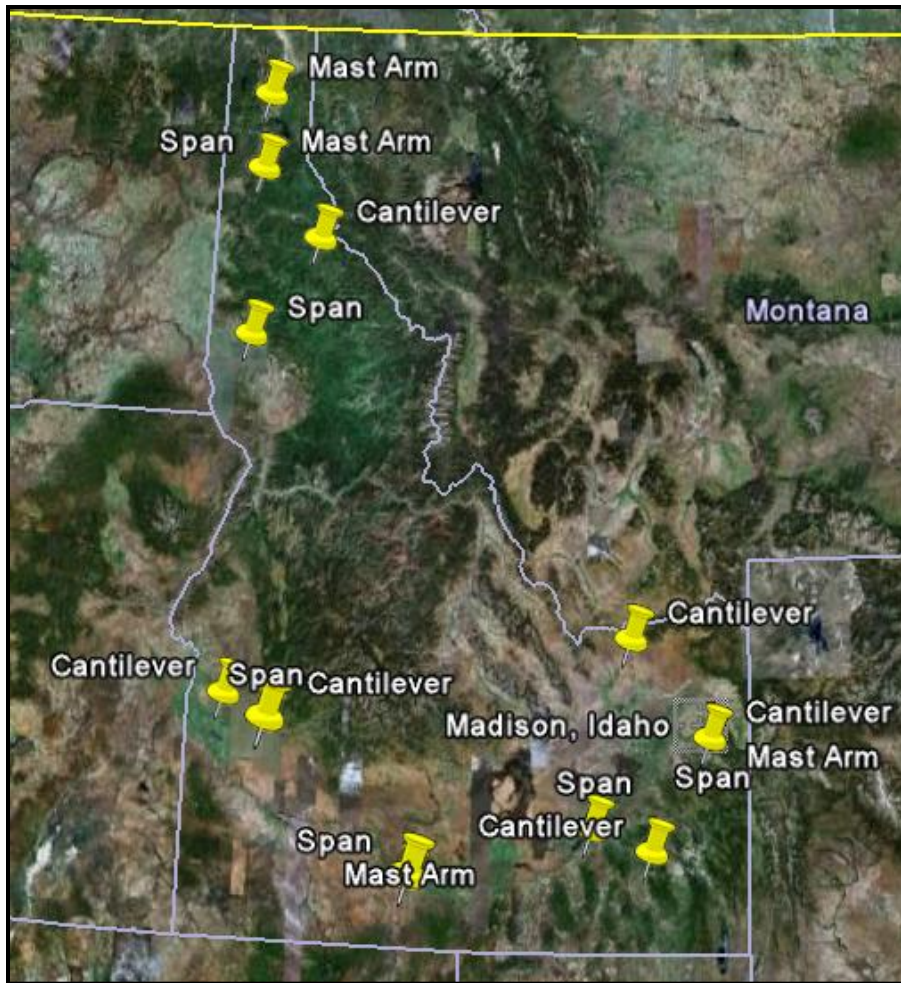


Figure 2.5 Idaho Traffic-Signal Cracking Locations

2.3.6 Missouri

Collins Engineers, Inc. (personal communication, July 22, 2009) performs inspections on the high-mast and traffic-signal poles in Missouri. Data collected from a survey of high-mast and traffic-signal poles taken in June of 2009 were sent as a response for the survey, which included crack type and location. The report showed that cracks have been located only in traffic-signal poles. The data sent were mapped in Google Earth and are illustrated in Figure 2.6.

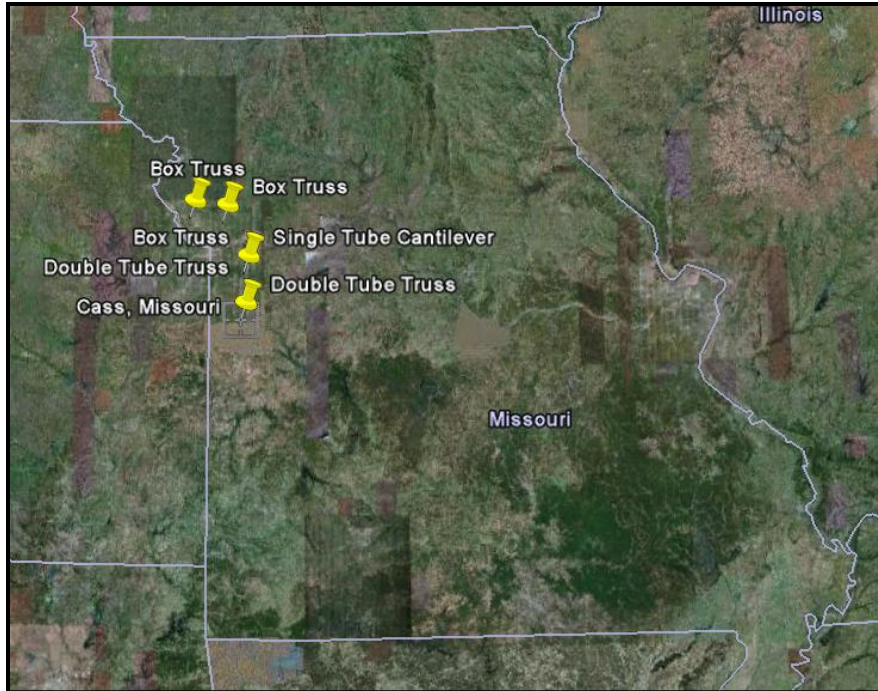


Figure 2.6 Missouri Traffic-Signal Crack Locations

2.3.7 Florida

Data collected from the Florida Turnpike Enterprise’s survey of high-mast poles were sent from Ms. Meyer (personal communication, February 2, 2010), the engineer of maintenance operations, as a response for the survey. No information was given about traffic-signal poles. The data sent were in a KML format, which can be viewed in Google Earth, and included crack type and location. Figure 2.7 illustrates the locations of the cracked poles. All of the current cracking is caused by corrosion and section loss, but it was stated that these corrosion issues could lead to fatigue cracking in the future.

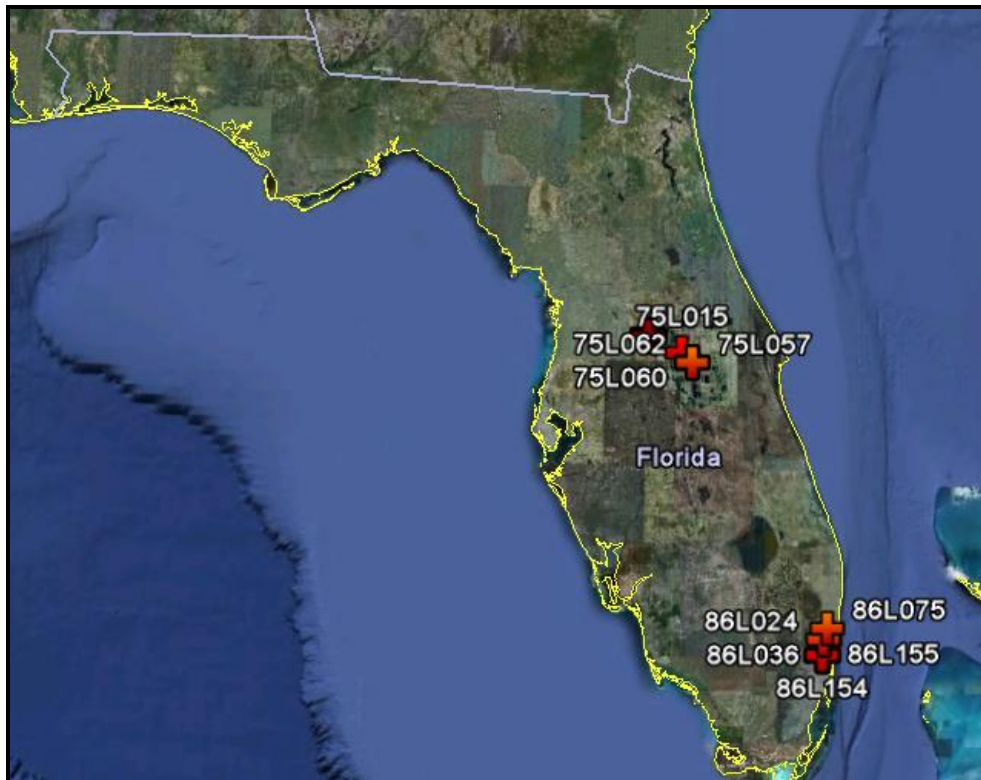


Figure 2.7 Florida High-Mast Cracking Locations

2.3.8 Colorado

Mr. Nord (personal communication, May 18, 2010), of the Colorado DOT, responded to the survey with a very detailed report. The report included crack type and location for high-mast and traffic-signal poles in the state. The data were mapped onto Google Earth, which is illustrated in Figure 2.8.

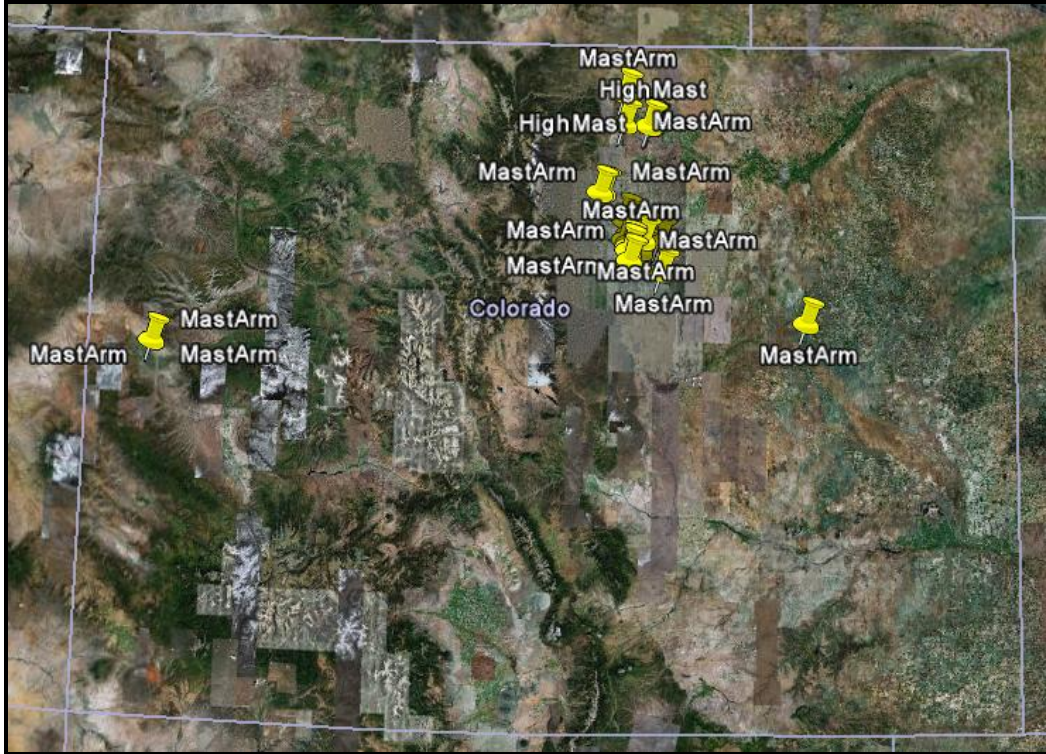


Figure 2.8 Colorado LTS Cracking Locations

2.4 Analysis of Additional Data

Each of the state’s cracking locations were compared to WPC maps. The WPC maps of each state are provided in the Appendix, Section 0. Table 2.2 describes the results for each state that had reported cracking in the second survey.

Table 2.2 Summary of Cracked Pole WPC

WPC	Traffic-Signal					High-Mast				
	1	2	3	4	5	1	2	3	4	5
Iowa								1	1	
Pennsylvania									2	
Idaho		4		11	13					
Missouri		5								
Florida						12	8			
Colorado	39*		1			6				

**see section 2.4.1 for data explanation*

2.4.1 Reliability of WPC Estimation

The classification of WPC reliability is discussed in Section 0. Colorado is specifically mentioned in the Wind Energy Resource Atlas as having a low degree of certainty due to its spatial variability and complexity of terrain (Elliott, Holladay, Barchet, Foote, & Sandusky 1986). A newer WPC map found on the Wind Energy Development Programmatic EIS website was used for the determination of Colorado cracked poles' WPC (EIS 2004). This newer map, which is provided in Appendix 0, has a much lower WPC's than the Wind Energy Resource Atlas map. As shown in Figure 2.8, the locations of cracked traffic-signal poles in Colorado are centralized to the Front Range area. Since this area is not reported as a high WPC, the age of the poles may play a part in their cracking; however, due to the discrepancy in maps and low degree of certainty of Colorado, the high amount of traffic-signal cracking locations in WPC 1 may still be accredited to fatigue caused by high average winds.

2.5 Summary and Recommendations

Price predicted that traffic-signal pole fatigue cracking caused by wind would most likely occur in high WPC areas (Price 2009). Table 2.2, excluding the Colorado data, follows this prediction.

Price predicted that high-mast pole cracking caused by wind would not necessarily occur in high WPC areas because it may be caused by vortex-induced vibrations (Price, 2009). Table 2.2 seems to follow this prediction; however, all of the cracking in Florida was due to corrosion, not wind. The cracked high-mast poles in Colorado are located in low WPC areas. Most of these locations are in northern Colorado, which as shown in Figure 2.1, has a higher WPC Certainty Rating than the Denver area.

The data collections of Phase I, as well as predictions of Price, have shown that the cracking of high-mast poles may not be caused by high WPC areas, but rather areas where vortex-induced vibrations may cause relatively high fatigue stress ranges. Therefore, further investigation on vortex-induced vibrations was continued in Phase II.

3. PHASE II: ESTIMATING VORTEX-INDUCED FATIGUE IN HIGH-MAST POLES

3.1 Vortex-Induced Vibrations

3.1.1 Definition

It is hypothesized that cracking of high-mast poles is primarily related to vortices shed at frequencies near the natural frequency of the structure. This phenomenon is known as vortex shedding. Amplified response due to vortex shedding is termed vortex-induced vibration (VIV). When structures are non-aerodynamic, or bluff bodies, wind flow around them can separate, which creates vortices. Figure 3.1 illustrates vortex shedding over a range of Reynolds numbers. A Reynolds number between 300 and 3×10^5 causes a fully turbulent vortex street. The Reynolds number is a function of fluid velocity, structure diameter, and the coefficient of kinematic fluid viscosity. Reynolds numbers values for high-mast poles can range from 10,000 to 200,000 (Ahearn 2010). When the vortices are shed in an organized, alternating fashion, a lift force begins to act on the body creating oscillations perpendicular to the flow direction. It is commonly acknowledged that the frequency, in hertz, of the alternating lift force can be estimated as follows:

$$f = \frac{SV}{D} \quad (1)$$

where S is the Strouhal number, V is the fluid velocity, and D is the width perpendicular to flow (Blevins, 1984). The Strouhal number is a function of both the shape of the structure and the Reynolds number. For this research, the Strouhal number of a high-mast was estimated to be about 0.18 for the Reynolds numbers of interest. The Strouhal number's dependence on the Reynolds number is illustrated in Figure 3.2.

When the vortex shedding frequency approaches the natural frequency of the structure, resonance occurs and vibrations build, creating a situation of amplified response (NCHRP 2002). If the oscillating force varies in frequency once lock-in has been reached, the vortex shedding tends to persist at the natural frequency for a certain wind speed range, as shown in Figure 3.3 **Error! Reference source not found.** The constant slope of the frequency to flow velocity line in the graph implies a constant Strouhal number. The range of lock-in will depend on the rate of change in velocity and the amplitude of vibration of the structure; that is, larger amplitude vibrations will hold lock-in for a larger wind speed range compared with smaller amplitude vibrations (Harris 1961).

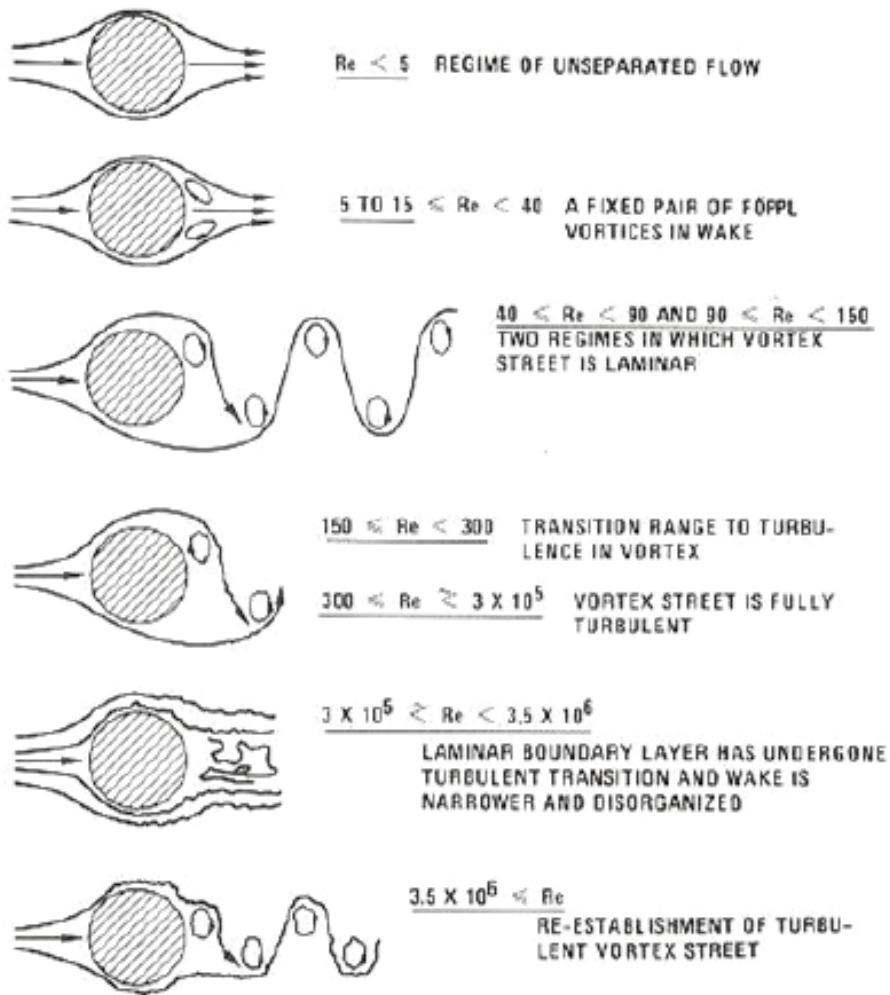


Figure 3.1 Regimes of fluid flow across circular cylinder (Lienard, 1966)

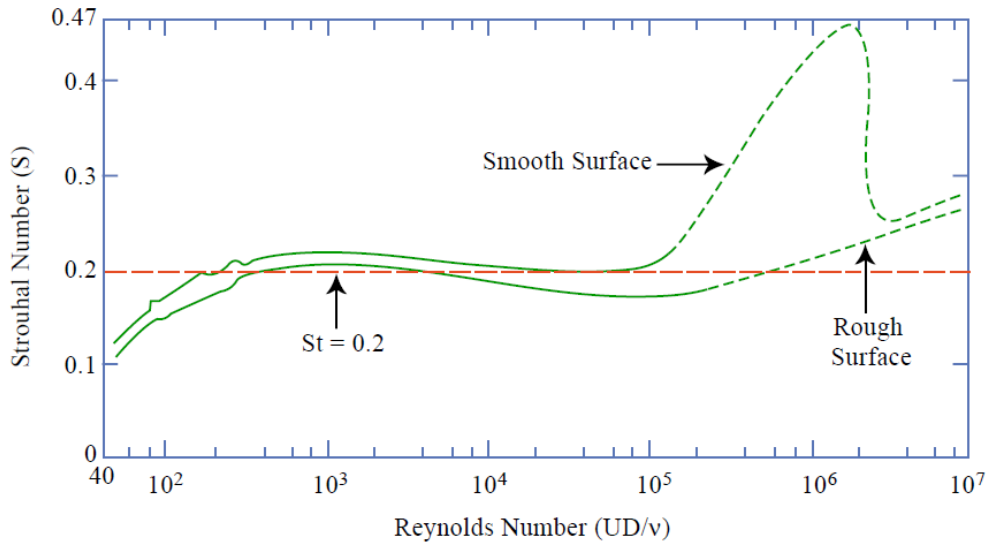


Figure 3.2 Strouhal number vs. Reynolds number (Techet, 2005)

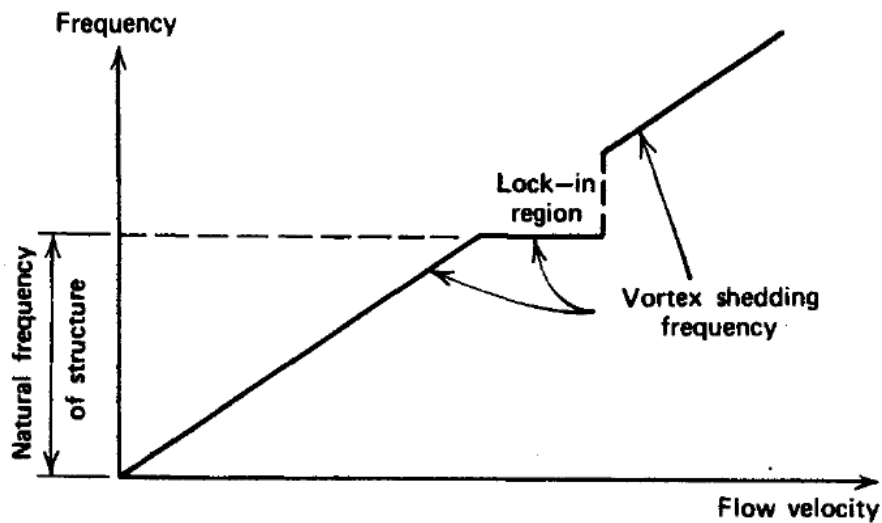


Figure 3.3 Vortex shedding frequency with wind velocity (Phares, Sarkar, Wipf & Chang 2007)

3.1.2 Iowa State University Study

The effect of vortex shedding on high-mast poles was examined in a previous study (Phares, Sarkar, Wipf, & Chang 2007) conducted by Iowa State University (ISU). ISU created a model for predicting wind loads on high-mast poles through the testing of two structures and through analysis of wind-tunnel data. The model included both vortex shedding and buffeting as wind loading variables. Buffeting loading is caused by fluctuations in the upstream wind. However, it was determined that buffeting was not a significant contributing factor in the response. For the specific poles tested, it was observed that VIV most frequently occurred at wind speeds of 3 to 8 mph, exciting the second mode of vibration. The modes of vibration are illustrated in Figure 3.4 **Figure** . The maximum displacements measured created base stresses larger than the constant amplitude fatigue limit of the structures for their design category E', which is 2.6 ksi. The measured structural damping ratios were observed to be 0.6%, 0.17%, and 0.27% for the first three modes, respectively. The values for second and third mode are lower than the design

value of 0.5% suggested in the AASHTO LTS (AASHTO 2009). The structural damping ratio describes the ability of a structure to reduce the amplitude of oscillations over time. Several recommendations were made by the ISU researchers for further work, a few being to include height, taper ratio, damping ratios, and mass per unit length in vortex shedding modeling. It was also suggested to include the data from wind climate zones to connect the modeling to existing structures.

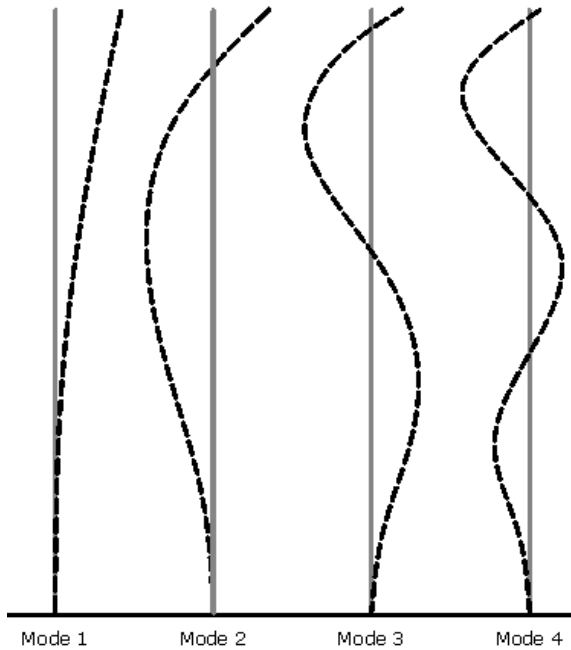


Figure 3.4 Modes of Vibration

3.1.3 University of Wyoming Study

A study was conducted at the University of Wyoming (UW) that tested VIV aerodynamic suppression devices (Ahearn 2010). Various treatments for VIV suppression were fitted to a local high-mast pole and results were tested against a non-retrofitted pole. These poles were fitted with strain gages, accelerometers, and anemometers to compare response of the treatments. The high-mast poles are located near the intersection of Interstate 80 and Highway 287, as seen in Figure 3.5.

A pluck test was performed to determine the natural frequencies of the poles and associated modal damping ratios. The pluck test required the pole to be pulled back to a bent position and then suddenly released to create a free-vibration response. Strain and acceleration data were monitored. Figure 3.6 illustrates a typical response. The Prony method was used to establish the natural frequencies and associated damping ratios. Table 3.1 illustrates the results and compares the test to the structural analysis model described below.

A model was created in the Structural Analysis Program (SAP2000, version 12) to simulate the poles being tested. A non-prismatic element was used to model the taper and the section descriptions in the program were made to account for the varying wall thickness. The experimentally determined damping ratios for each mode were used. The luminaire's effect was modeled by an eight-inch disk added to the top of the structure. The base of the structure was made to be fully fixed from rotation and displacement. This model, the pluck test results, and the data collection were used to compare to the results. Conclusions

from Ahearn showed that mode three was critical for the pole at a height of about 97 feet at wind speeds of 10 to 19 mph.

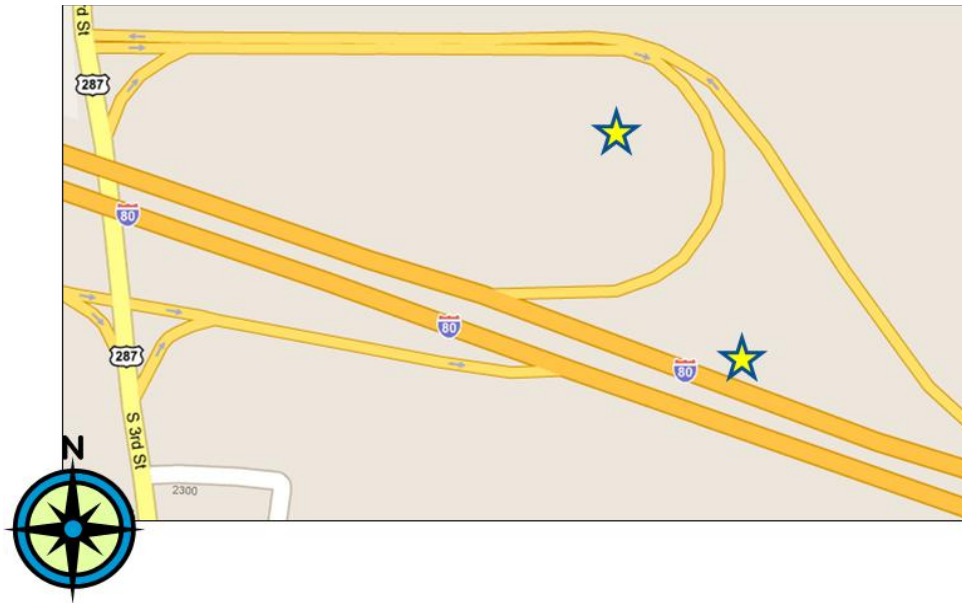


Figure 3.5 Location of Laramie High-Mast Poles

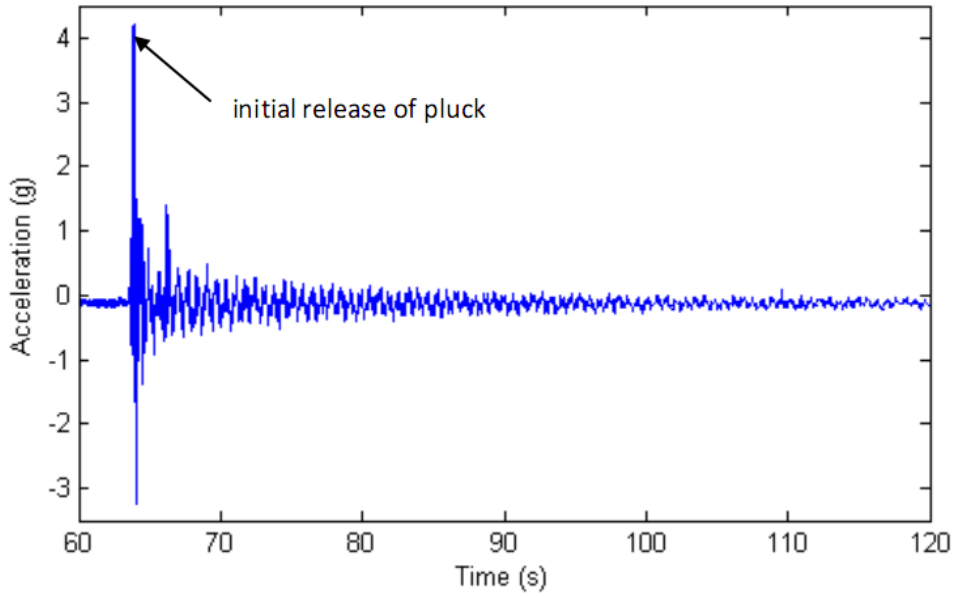


Figure 3.6 Typical Pluck Test Acceleration Data (Ahearn 2010)

Table 3.1 Natural Frequencies of Wyoming Pole (Ahearn, 2010)

Mode	1	2	3	4
SAP Natural Freq (Hz)	0.385	1.64	4.22	8.27
Actual Natural Freq (Hz)	0.34	1.5	3.9	7.5
% Difference	11.6%	8.6%	8.0%	9.3%

Table 3.2 Damping Ratios of Wyoming Pole (Ahearn 2010)

Mode	1	2	3
Damping Ratios (%)	0.5	0.3	0.1

3.2 AASHTO Specifications

The AASHTO Luminaire and Traffic Signal Specifications (LTS) provide provisions that must be met by the owner and manufacturers of highway structures in order to ensure the safety and quality of the product. Due to the failure of high-mast poles and traffic signals in certain areas of the country, changes were made in the third edition to yield the Fourth Edition (AASHTO 2001). These changes often require an increase in structure size to provide higher fatigue resistance. The more stringent requirements are applied to all areas of the country, rather than just the areas where failures occurred. The increase in size directly causes an increase in cost.

Recent failures of high-mast poles in the United States illustrate that fatigue cracking for these poles is still a significant problem. In 2003, a high-mast pole was reported to have fallen along I-29 near Sioux City, Iowa (Chang, Phares, Sarkar, & Wipf 2009). In 2004, two poles fell near the Denver International Airport (Goode & van de Lindt, 2007), and there are other reported failures in Wyoming, Illinois, Missouri, and Wisconsin (Phares, Sarkar, Wipf, & Chang 2007). Recently, the fifth edition of AASHTO LTS was released, but there were few changes in this procedure that would improve the fatigue design of high-mast poles (AASHTO 2009).

The AASHTO LTS has simple design equations to resist vortex shedding. The method only takes into account one critical velocity and mode of vibration per analysis, but it is recommended that modes 1 and 2 be tested. A reference to the National Cooperative Highway Research Program (NCHRP) Report 469 is the only procedure for considering higher modes and tapered sections:

Observations and studies indicate that tapered poles can experience vortex shedding in second or third mode vibrations and that those vibrations can lead to fatigue problems. Procedures to consider higher mode vortex shedding on tapered poles are demonstrated in NCHRP Report 469; . . . (AASHTO 2009)

The NCHRP Report 469 contains an example that considers the tapered characteristics of a pole, but only mode two is computed (NCHRP 2002). This method was applied to the Laramie pole and compared with the transfer sheet described in Section 0. Results can be seen in Section 0. To calculate the vortex-shedding induced loads, an equivalent static pressure range is determined as follows:

$$P_{vs} = \frac{0.00256V_c^2 C_d I_F}{2\beta} \text{ (psf)} \quad (2)$$

where V_c is the critical velocity in mph, C_d is the drag coefficient based on the critical velocity, I_F is the importance factor and β is the damping ratio which is recommended to be 0.5%.

3.3 CSA Specifications

The Canadian Standards Association (CSA) Highway Bridge Design Code may be used specifically for the calculation of across wind loads on slender structures, mainly VIV (CSA 2006). To complete the calculations, a stress range limit is computed using a detailed analysis, which is taken to correspond to a fatigue life over two million cycles. The base stress is determined by first loading the member with the peak inertia loads acting statically, where the magnitude of the peak inertia load per unit length at any location x along the pole for mode of vibration, i , is as follows:

$$F_i(x) = (2\pi n_i)^2 y_i(x) m(x) \quad (3)$$

where n_i is the natural frequency (cps) for mode of vibration i , $m(x)$ is the mass per unit length at location x , and $y_i(x)$ is the amplitude of vibration from vortex shedding.

The detailed analysis takes into account varying geographical conditions by requiring the use of an hourly mean reference wind pressure (q) for the design return period and a wind exposure coefficient (C_e) to calculate the design mean hourly wind speed as follows:

$$V \geq 1.24(qC_e)^{0.5} \quad (4)$$

The CSA code also considers the tapered shape of a high-mast pole to be a significant geometric factor and has separate equations to estimate vibration amplitude. The frequency of vortex shedding is considered to vary with height and is to remain in phase only over the portion of the member in which the diameter remains within $\pm\Omega\%$ of the diameter, where Ω is recommended to be 10%, as seen in Figure 3.7. Therefore, vibration amplitudes are to be computed along the entire length of the pole. The CSA code also requires a dynamic analysis of the pole to be completed in order to find the natural frequencies, mode shapes, and a generalized mass for each mode of vibration.

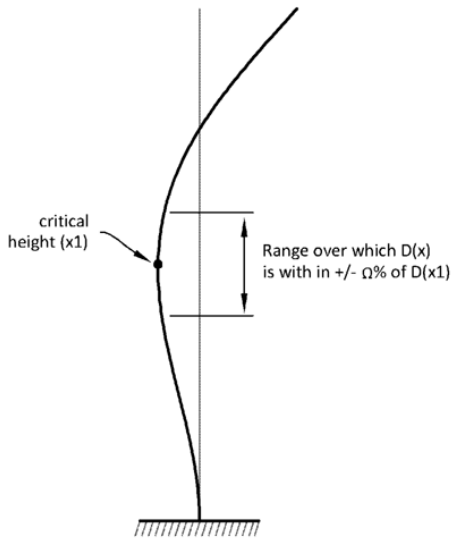


Figure 3.7 Length of in-phase VIV on a high-mast pole

To determine the amplitude of vibration from vortex shedding, the CSA code implements both a sinusoidal approach and a band-limiting model. It is recommended that the sinusoidal model only be used when the vibrations become significantly large, or greater than 2.5% of the diameter. The rationale is discussed in the commentary:

Treating vortex shedding as a sinusoidal process is an approximation leading to conservative estimates. The variation of the wind speed with height, turbulence of the natural wind, and the presence of signs and other accessories all tend to disrupt the spatial correlation of the excitation. It is generally accepted as more accurate to treat the excitation as a band-limited process and to assume that the forcing tends to become harmonic only when the motion of the member is sufficiently large to organize the shedding of vortices (CSA 2006).

The band-limiting model considers the vortices shed in a random manner distributed about the dominant frequency rather than fully harmonic. The band limiting and sinusoidal models are calculated as follows:

$$y_i(x) = a_i(x_1) \mu_i(x) \quad (5)$$

$$\text{Band limiting: } y_i(x) \leq .025D(x) \quad a_i(x_1) = 3.5 \sqrt{\frac{2\pi L}{\zeta_i \Psi(x_1)} \frac{C_L \rho D^4(x_1)}{(4\pi S)^2 GM_i}} |\mu(x_1)| \quad (6)$$

$$\text{Sinusoidal: } y_i(x) > .025D(x) \quad a_i(x_1) = \frac{\sqrt{2} \rho C_L D^2(x_1) \int_{x_1-B}^{x_1+B} D(x) |\mu_i(x)| dx}{(4\pi S)^2 \zeta_i GM_i} \quad (7)$$

where:

$a_i(x_1)$ = the modal coefficient of magnitude x_1 = location along the tapered member at which VIV is being considered

L = the correlation length ζ_i = structural damping for the i th mode

$\Psi(x_1) = \frac{dD(x_1)}{dx} + \frac{\alpha D(x_1)}{x}$ α = wind velocity profile exponent

C_L = root mean square lift coefficient ρ = air mass density

$D(x)$ = the diameter at height x S = Strouhal number

GM_i = generalized mass for mode of vibration, i $\mu_i(x)$ = amplitude of the member mode shape at location x for mode of vibration, i

B = length of member above or below x_1 for which $D(x)$ is within a certain percentage of $D(x_1)$, taken as 10% unless justified otherwise

The Strouhal number is recommended as a constant value of 0.18 for a circular cross section in a subcritical Reynolds number situation ($Re < 3 \times 10^5$).

A numerical tool spreadsheet was created to predict the base moment of high-mast poles in resonant wind situations, which is further detailed in Section 0.

3.4 Application of CSA Specifications

For the purpose of this research, the name “transfer sheet” was given to a numerical tool in which inputs of high-mast pole structural data, dynamic data, and local wind data are combined through analysis to yield an output of maximum base stress and fatigue life. Essentially, this sheet implements a transfer function that can be used to relate stochastic wind data to stochastic fatigue-related stresses.

The Phase II transfer sheet, created in Excel™, utilizes the design method outlined in the Canadian Standards Association: Highway Bridge Design Code (CSA) Section A3.2.4 (CSA 2006). The pages from this section can be found in Appendix 0 and 0. This method was chosen because of the vortex shedding loading and fatigue simulation detail included in the equations, as discussed in Section 0. The inputs for the transfer sheet can be split into the categories of high-mast structural data, dynamic data, and local data. The sheet uses a looping parameter in Excel to generate the outputs of critical wind velocity, critical mode, maximum displacement, and base moment as shown in Figure 3.8. This looping process was coded in Excel’s Visual Basic for Applications.

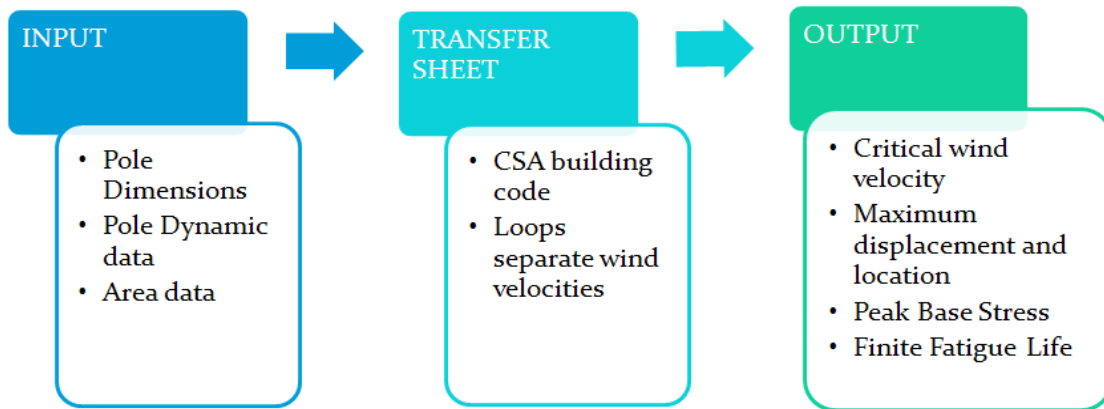


Figure 3.8 Transfer Method Process

3.4.1 Input

The structural input values in the transfer sheet are variables that are specific to certain types of high-mast poles, such as luminaire mass, base diameter, thickness, and tapering angle. The variables were made to be easily changeable so that the effects they have on displacement could be studied, however, the pole height must remain at 120 feet. This restriction can be relaxed by reprogramming in a design/evaluation application, but is considered beyond the scope of the present work. The Laramie pole tested by Ahearn was used to compare numerical and experimental results (Ahearn 2010). The WYDOT specifications of the Laramie pole can be found in Appendix 0.

The pole's modal characteristics are also inputs of the transfer sheet; these include frequencies and mode shapes, $\mu_i(x)$. As both the UW (Ahearn 2010) and ISU (Chang, Phares, Sarkar, & Wipf 2009) reports describe that modes 1 through 3 produce critical vibrations, only these modes were considered. A SAP2000 model was created by Ahearn for the Laramie high-mast pole tested as described in Section 0. The modal shapes from the SAP2000 model were used in the transfer sheet by normalizing the shape and performing a curve fit as seen in Figure 3.9. All of the trend lines produced an R^2 value of 0.99 to 1.0. The curve fit provides the mode shape amplitude at any height and were used as formulas in the subsequent computations. Although the mode shapes can be varied and can be automated in the future, the present work was limited to the 120-foot test pole.

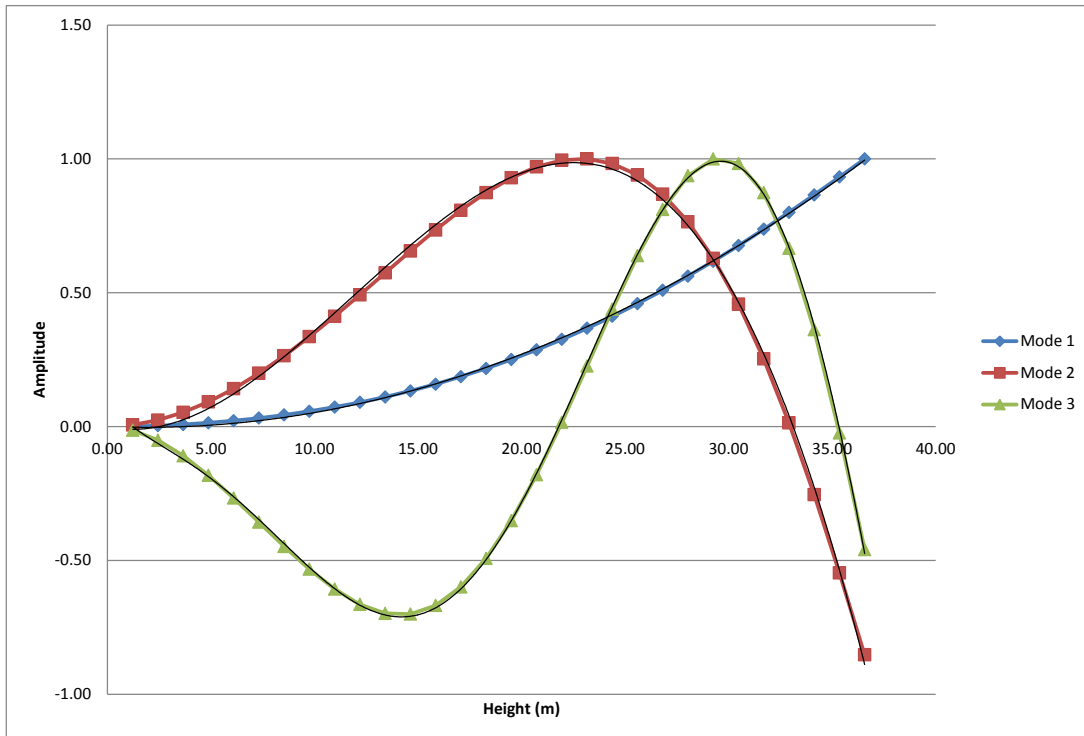


Figure 3.9 Mode Shapes for Transfer Sheet

Variables common to describing structural dynamics are included in the transfer sheet, such as Strouhal number, lift-coefficient, correlation length, natural frequencies, and modal damping ratios. The Strouhal number was taken as 0.18, the lift-coefficient as 0.5, and the correlation length as 2.5 as the CSA code suggests for circular cross sections (CSA 2006). The natural frequencies and structural damping variables for modes 1 through 3 of the pole are easily changeable inputs of the sheet. The structural damping variables were initially made to match the predictions of Ahearn from the pluck test and SAP2000, but were varied to study their effects.

Area data is the final category of input variables for the transfer sheet. The CSA code requires inputs of air mass density and wind velocity profile exponent for boundary layer effects. The air mass density was taken as $0.058 \frac{lb}{ft^3}$ and the wind velocity profile exponent as 0.143 to be consistent with the surrounding terrain.

3.4.2 Looping Process

The CSA specifications require the estimation of critical velocities and critical vibration modes in order to determine a maximum displacement and the associated base stresses. The specifications also suggest that the modal coefficient of magnitude, as described in Section 0, be calculated at all heights. The transfer sheet allows the user to skip estimation of critical velocity and critical mode, as all velocities and modes are computed from a looping process. The user can choose a large range of velocities to be tested and the modal coefficient of magnitude is automatically calculated at all heights.

Both methods, band-limiting and sinusoidal, are considered when calculating the maximum modal coefficient of magnitude. The integrated portions of the equations are estimated using trapezoidal integration and shape estimation. The CSA code explains that only areas where excitation will occur need

be considered for the modal coefficient of magnitude. Only a critical wind speed can excite a section of a specific diameter, governed by the equation:

$$V = \frac{fd}{S} \quad (8)$$

As the transfer sheet varies an upper and lower wind velocity and calculates possible excitation along all heights of the tapered pole, the equation is rearranged as follows:

$$\frac{SV_{lower}}{n_i} \leq D(x) \leq \frac{SV_{upper}}{n_i} \quad (9)$$

If the diameter at a specific height is excited by the range of wind velocity, the modal coefficient of magnitude at this height is calculated for determining the amplitude of vibration. The variation of wind speed with height due to the atmospheric boundary layer is also considered by creating a profile governed by the wind profile exponent input.

The looping process of the transfer sheet uses Visual Basic for Application (VBA) to vary a lower and upper wind speed, which is defined by the user. The bin size, i.e., difference between lower and upper velocity, and maximum velocity are both user inputs. As the wind speeds are varied, the sheet stores output from each magnitude. For example, the user may choose a bin size of 1 mph and a maximum velocity of 50 mph. The sheet begins with a lower velocity of 0 mph and an upper velocity of 1 mph and calculates the maximum displacement along the entire height of the pole. With this displacement stored, the sheet moves to the next bin of 1 to 2 mph and similarly up to 49 to 50 mph.

For each bin, the sheet also calculates peak base stress by summation of the peak inertial load, as recommended by the CSA code. The CSA equation is modified to include the luminaire as follows:

$$(\Delta f)_{peak} = \frac{\Sigma(l_i F_i(x) \Delta x + l_i F_{top})}{S} \quad (10)$$

where l_i is the moment arm to the base from each point, Δx is the increment at which forces are being calculated and F_{top} is the weight of the luminaire.

The stored maximums are then analyzed to determine maximum displacement, height of maximum displacement, base moment, and critical velocity of the first three modes of vibration. Figure 3.10 re-emphasizes the components of the transfer sheet.

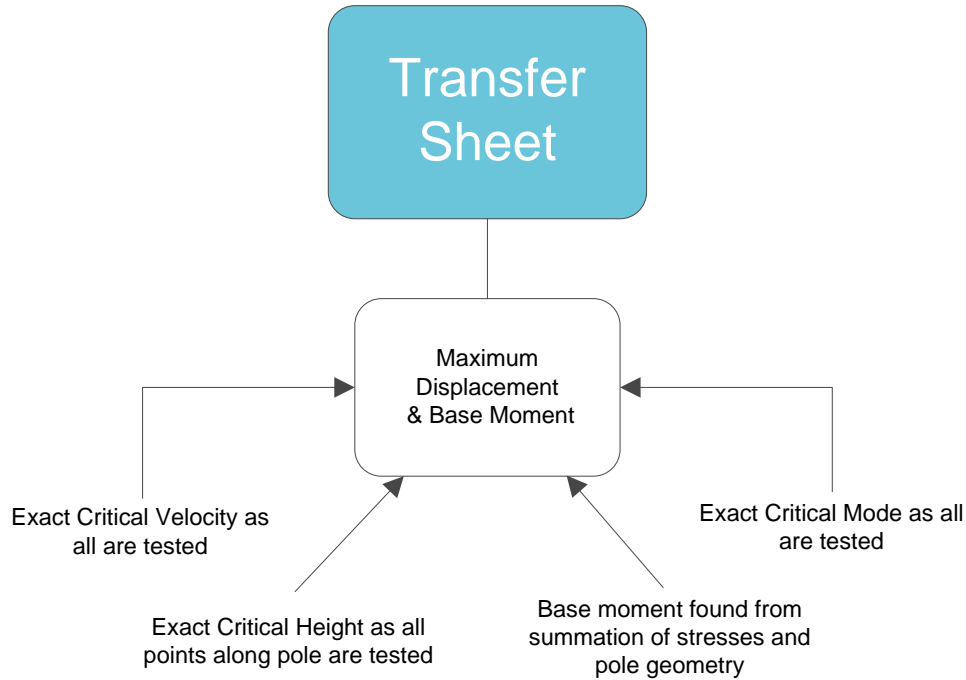


Figure 3.10 Transfer Sheet Process

3.5 Estimated Fatigue Life

The Transfer Sheet is able to use local wind data to predict fatigue life. Although a critical velocity will cause the highest amount of fatigue on a structure, all other velocities will cause stress as well. This is accounted for in the sheet. An infinite-life check is performed, as well as determination of a finite fatigue life. The procedure in the AASHTO Manual for Bridge Evaluation was used as a guideline for the calculations (AASHTO 2008). The infinite-life check compares the maximum stress range expected with the constant-amplitude threshold. The fatigue life, which is the number of stress cycles the high-mast can sustain before failure, is expressed as the total finite fatigue life in years. The sheet begins by calculating an effective stress range, $(\Delta f)_{eff}$, as follows:

$$(\Delta f)_{eff} = R_s \left(\sum \gamma_i \Delta f_i^3 \right)^{\frac{1}{3}} \quad (11)$$

where R_s is the stress-range estimate partial load factor, taken as 1 for the mean fatigue life calculation, $\sum \gamma_i$ is the percent of cycles at a particular stress range and Δf_i is the particular stress range. The particular stress range, Δf_i , is the peak base stress specific to each velocity, which is calculated in the sheet. The percent of cycles at a particular stress range, γ_i , was calculated as follows:

$$\gamma_i = \frac{n_{cycles,i}}{\sum (n_{cycles,i})} \times 100 \quad (12)$$

where $n_{cycles,i}$ is the number of cycles for each mode, i , determined by:

$$n_{cycles,i} = f_i \times T \times n_i \quad (13)$$

where f_i is the frequency being excited by the particular velocity, T is number of seconds per year, or 3.1536×10^7 , and n_i is the percent of the year that the particular frequency is being excited. This percentage was determined using the wind analysis program Windographer (Windographer 2.2 2010) and the collection of Laramie wind data (Station: Laramie General Brees Field, WsID 21834, 2004-2009). Windographer was used to sort one year of wind data into a histogram of the frequency (%) of wind velocity in one year as shown in Figure 3.11. The histogram shows that in Laramie, for 40% of the year, the average wind speeds range between 6 to 13.2 mph. Windographer adds a probability distribution function to the histogram, which is the Weibull distribution. The values for the Weibull distribution are inputs in the transfer sheet, which then determines the values of n_i .

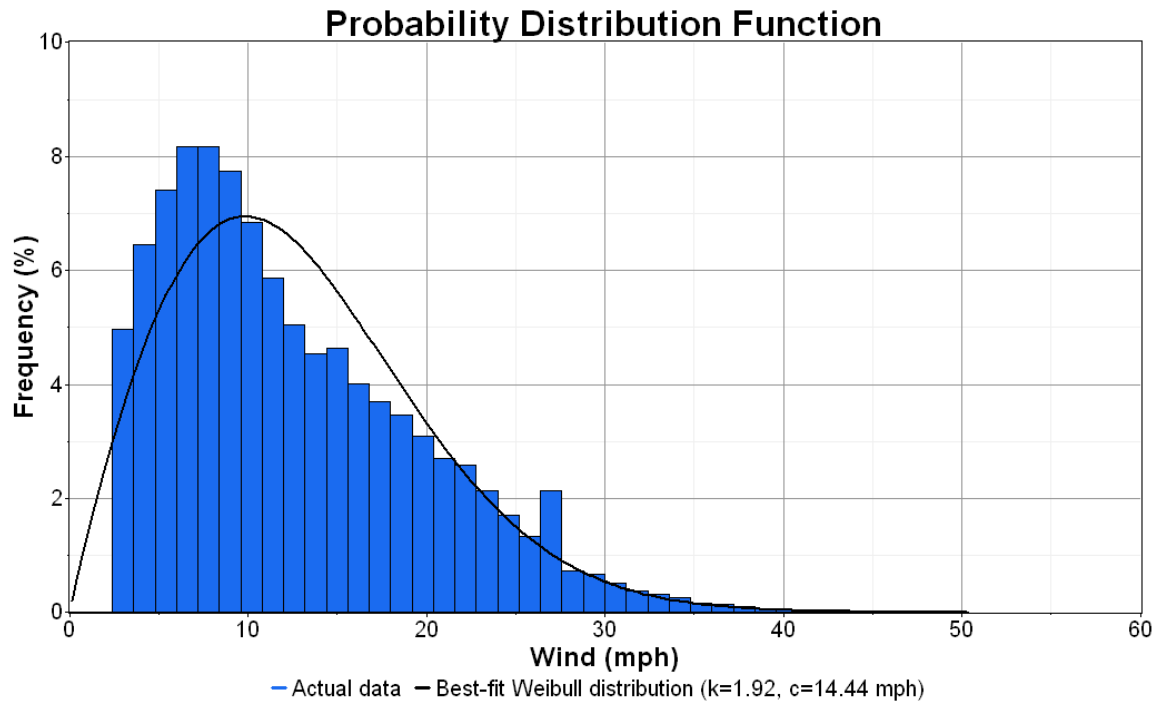


Figure 3.11 Laramie Wind Data Distribution

The infinite-life check is then calculated by the sheet starting with the calculation of the maximum stress range as follows:

$$(\Delta f)_{max} = 2.0(\Delta f)_{eff} \quad (14)$$

The sheet also estimates the finite fatigue life using the following equation from the AASHTO Manual for Bridge Evaluation (AASHTO, 2008):

$$Y = \frac{R_R A}{365n(ADTT)_{SL} \left[(\Delta f)_{eff} \right]^3} \quad (15)$$

$$Y = \infty \quad \text{if} \quad (\Delta f)_{max} \leq (\Delta F)_{max} \quad \text{or} \quad (16)$$

where R_R is the resistance factor, taken as 1 for minimum life, and A is the detail category constant, taken as $11 \times 10^8 \text{ ksi}^3$ for detail category E. The constant amplitude fatigue limit, $(\Delta F)_{TH}$, can be estimated as 4.5, as specified in the AASHTO LTS specifications for detail category E (AASHTO 2009). The two in Equation 14 is the amplification in bridge to represent the 1:10000 probability of exceed the CAFL. This was not refined for poles in this report because of the imprecise nature of the computation and project scope.

The portion of the equation

$$365n(ADTT)_{SL} \quad (17)$$

is the number of cycles per year for a bridge and is modified to be the number of cycles per year of the high-mast by determining the summation of the number of cycles per mode, $n_{cycles,i}$. The equation becomes as follows:

$$Y = \frac{R_R A}{\Sigma(n_{cycles,i}) \left[(\Delta f)_{eff} \right]^3} \quad (18)$$

3.6 Example Computations for Laramie Pole

A local pole was chosen to run through the transfer sheet in order to compare results to data collected by Ahearn (2010). Table 3.3 summarizes the general values used in the sheet to describe the pole's structural, dynamic, and area characteristics. The air density is specific to the Laramie elevation of 7,200 feet. Table 3.4 summarizes the dynamic values of the pole, which are specific to the modes. More details of the specific input are provided in Section 0.

Table 3.3 Local High-Mast Pole General Values

Description		Value
Luminaire Mass	m_{lum}	600 lb
Strouhal number	S	0.18
RMS Lift Coeff.	C_L	0.5
Band Width	B	0.25
Correlation Length	L	2.5
Air Density	ρ	0.058 lb/ft ³
wind velocity profile	α	0.143
Base Diameter	D_o	24.25 in
Tapering angle	θ	0.3342°

Table 3.4 Local High-Mast Pole Dynamic Values

Description		Mode		
		1	2	3
Structural damping	ζ_i	0.005	0.003	0.001
Natural Frequency (cps)	n_i	0.34	1.5	3.9

3.6.1 Displacement Estimation

For the first transfer sheet test (T1), the structural damping values were taken as in Table 3.4. These are the structural damping values determined by the pluck test performed by Ahearn and described in Section 0. Figures 3.12, 3.13, and 3.14 display the looping outputs for maximum displacement (in) vs. varying velocity (mph) for T1 for modes 1, 2, and 3, respectively.

Table 3.5 shows the absolute maximum displacements for each mode and the velocities and heights at which they occur. Mode 3 appears to have two velocities in which VIV can be excited; one at 11 to 12 mph, of 5.X inches, which is the maximum, and another at 19 to 20 mph, which excites a displacement of 2.7 inches. This may be due to the mode shape itself. Since the third mode shape has two points of maximum displacement, there are two sections along the pole that will shed vortices in phase to create excitation. These two locations have different diameters due to the taper and, therefore, two critical velocities.

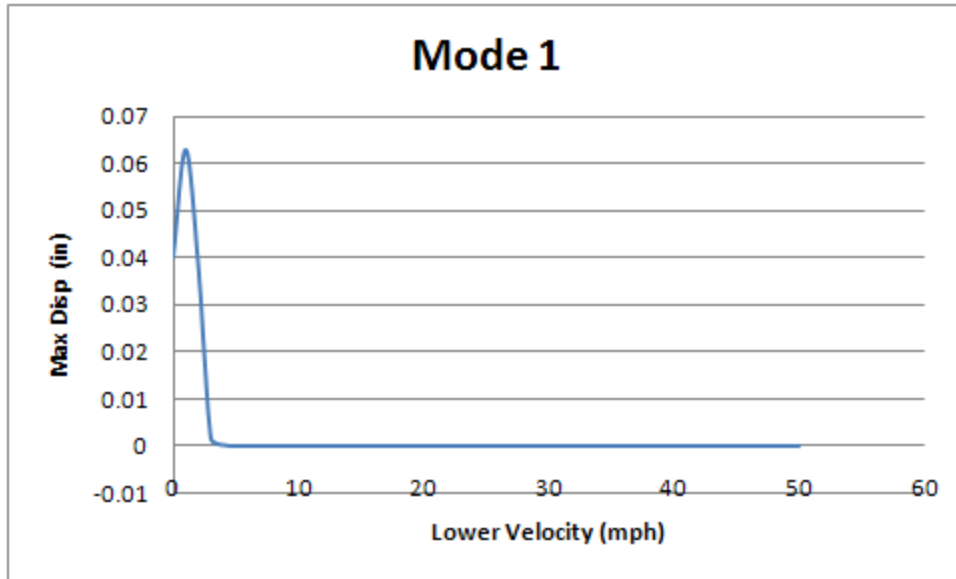


Figure 3.12 Mode 1 Results for T1 of Laramie Pole

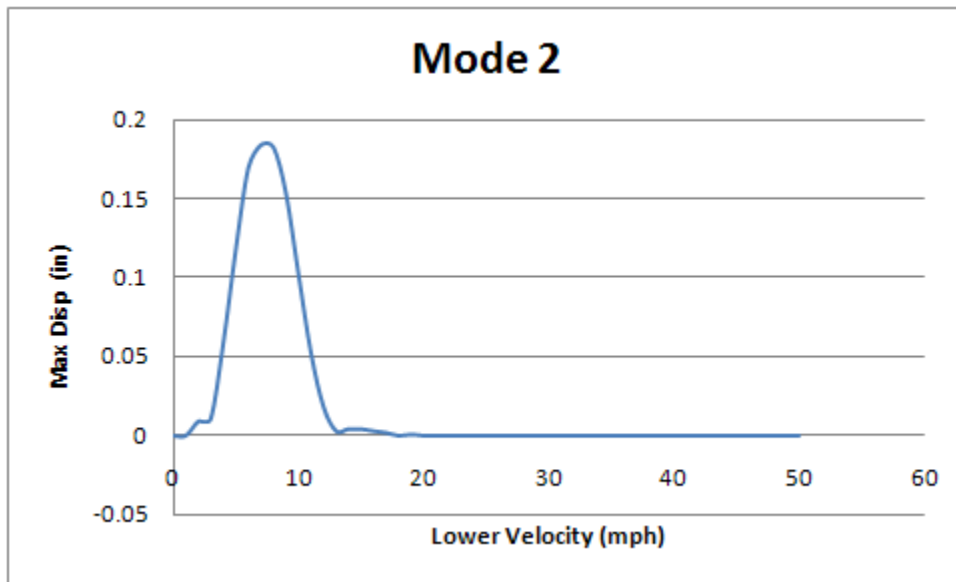


Figure 3.13 Mode 2 Results for T1 of Laramie Pole

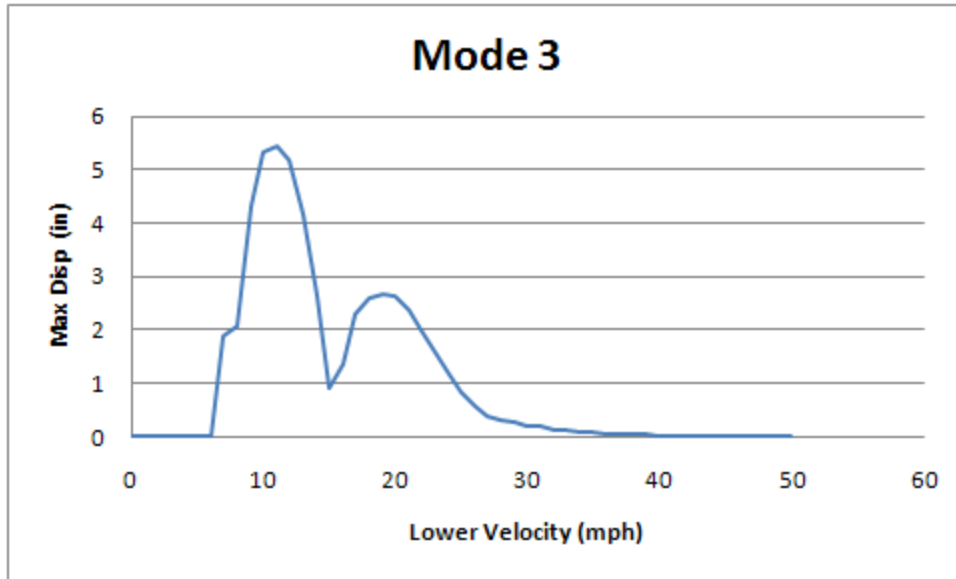


Figure 3.14 Mode 3 Results for T1 of Laramie Pole

Table 3.5 T1 Results for Laramie Pole

Mode	Critical Velocity (mph)	Maximum Displacement (in)	Critical Height (ft)
1	1 to 2	0.06	120
2	7 to 8	0.18	73.82
3	11 to 12	5.46	97.6

The results of T1 were compared with the field data collected by Ahearn on the Laramie pole. Figure 3.15 shows a collection of field data of the Laramie pole. Circular points represent along-wind data, whereas diamond points represent across-wind. Across-wind vibrations would be excited by VIV. The acceleration of the pole is directly related to its displacement; therefore, trends can be compared. Higher accelerations can be seen in both the 11-12 mph and 19-20 mph ranges as shown by the vertical, blue lines. Although it seems that a higher displacement has been caused by the 19-20 mph region, because Ahearn was not able to continuously collect data, this conclusion cannot be directly validated.

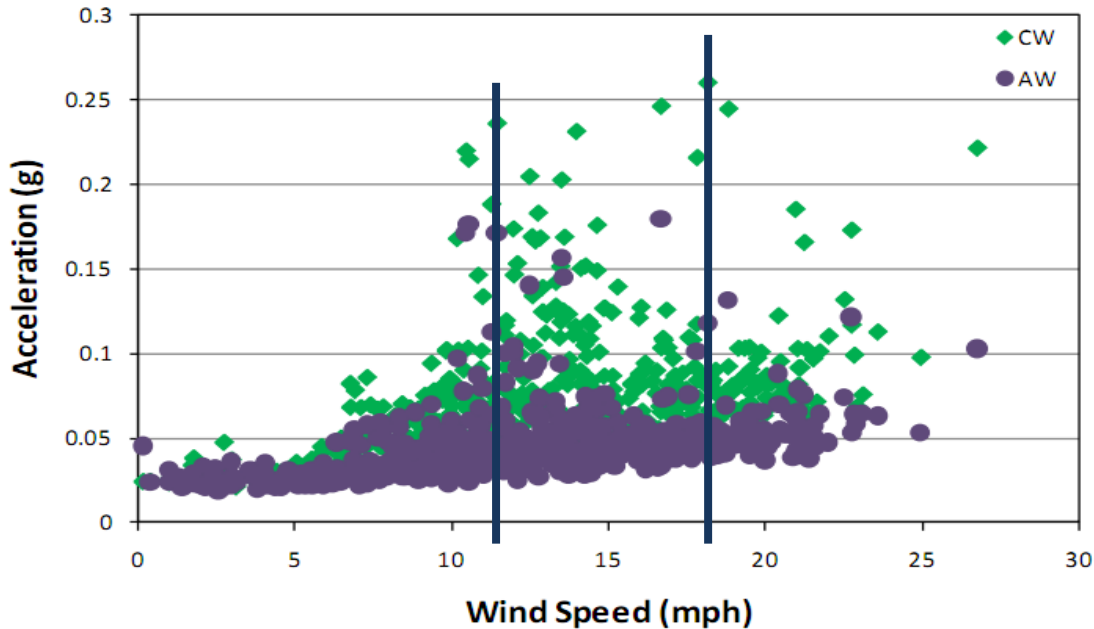


Figure 3.15 Field Data for Laramie Pole (Ahearn 2010)

Ahearn’s results align with the transfer sheet prediction in showing that Mode 3 at a height of 97 feet produced the highest displacements of the Laramie pole and was therefore the critical mode. The magnitudes of displacement computed based upon frequency and acceleration data, however, were considerably less. Ahearn recorded displacements on both a non-retrofitted pole and several retrofitted poles as described in Section 0. For a non-retrofitted pole, the maximum displacement recorded was 0.29 inches, and for a helical strake retrofitted pole, it was 0.41 inches. Ahearn concluded that although the pole retrofitted with helical strakes continued to show VIV in the third mode, due to non-continuous collection of data, it did not necessarily cause them to increase (Ahearn 2010).

The gap between the transfer sheet’s estimation of displacements and the actual recorded values is most likely caused by the input of structural damping values. As shown in Section 0, the structural damping values are a direct input to the CSA calculation of displacement. The estimation of structural damping values through a pluck test may give lower values than what would occur in an actual VIV situation. During a pluck test, the pole is pulled to a displacement and released to vibrate freely. This process lacks the presence of a critical wind speed and, therefore, the interaction of the oscillating structure with the oscillating fluid and the aerodynamic damping that may result from it.

Due to the possible error in estimation of the structural damping, higher values were put into the sheet to estimate displacement. For the second transfer sheet test (T2), structural damping values of 0.5% were used in all modes. Results are provided in Figures 3.16, 3.17, and 3.18 for modes 1, 2 and 3, respectively. Table 3.6 shows the absolute maximum displacements for each mode and the velocities and heights at which they occur. The maximum displacement is still being excited in the third mode, but the displacement is now estimated at 1.09 inches.

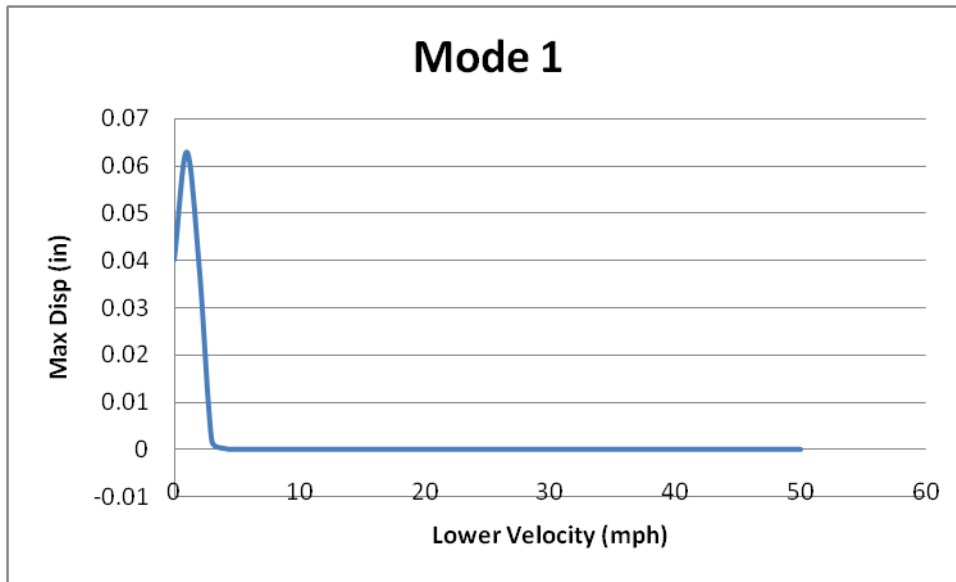


Figure 3.16 Mode 1 Results for T2 of Laramie Pole

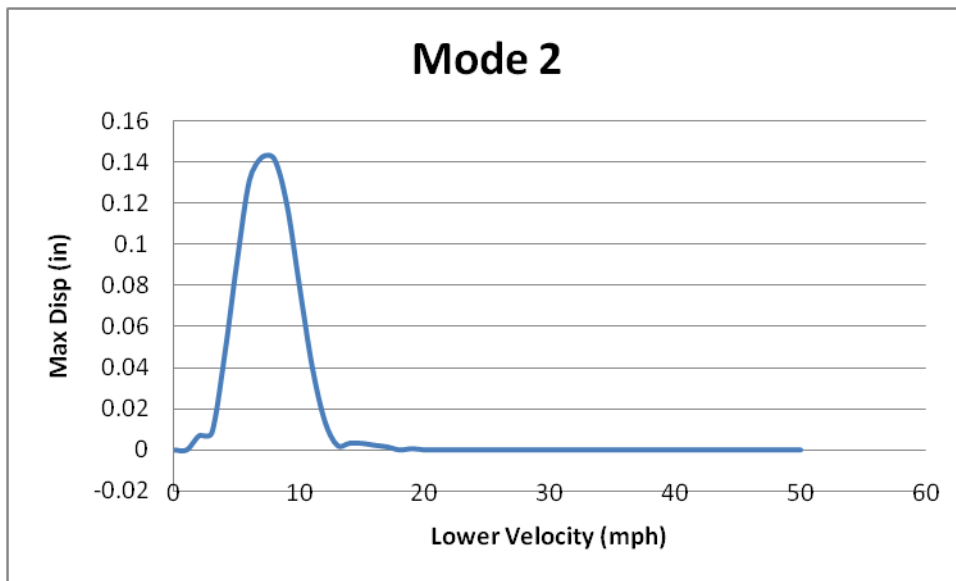


Figure 3.17 Mode 2 Results for T2 of Laramie Pole

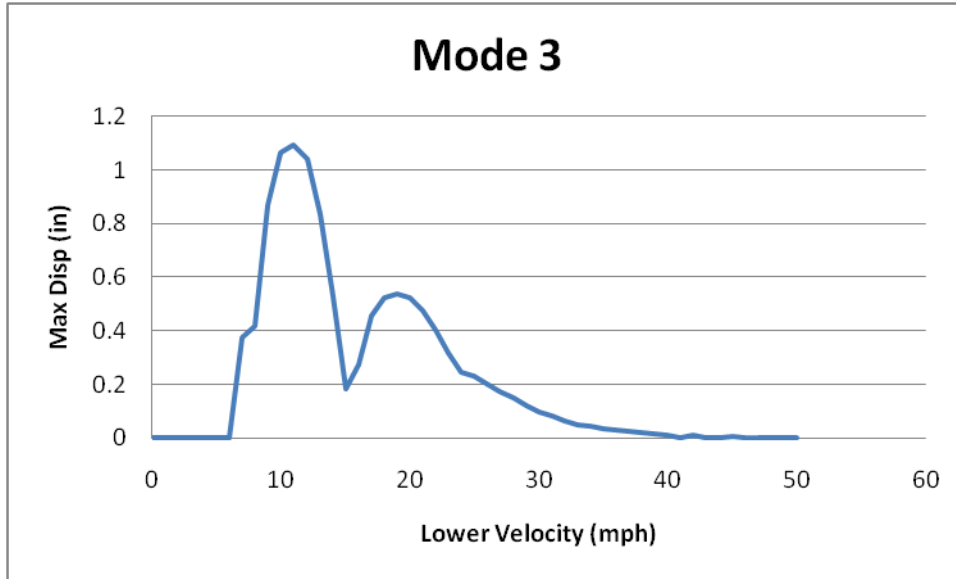


Figure 3.18 Mode 3 Results for T2 of Laramie Pole

Table 3.6 T2 Results for Laramie Pole

Mode	Critical Velocity (mph)	Maximum Displacement (in)	Critical Height (ft)
1	1 to 2	0.06	120
2	7 to 8	0.14	73.82
3	11 to 12	1.09	97.6

3.6.2 Fatigue Life Estimation

The fatigue life estimation calculations were recorded for the critical mode, Mode 3, for the Laramie pole at varying damping ratios in 3.7. At a damping ratio of 0.1%, the effective stress range expected in the life of the pole, $(\Delta F)_{\max}$, is 30.3 ksi, which predicts a finite fatigue life, Y, of less than 1 year. When the damping ratio is increased to 0.5%, the maximum stress range is lowered to 4.1 ksi, which predicts an infinite fatigue life. This illustrates the fatigue life calculations' sensitivity to damping ratio.

The sudden transition from a low fatigue life to infinite life can be explained by the S-N curve illustrated in Figure 1.1. The weld can withstand a finite number of cycles until the constant amplitude fatigue limit of 4.5 ksi is reached, in which case the weld can withstand infinite cycles. The continued calculated values without the threshold restraint are shown in the last row of Table 3.7. The relatively low fatigue lives predicted for each damping ratio can either be attributed to over-estimation of the CSA method and/or the difficulty in predicting a fatigue life for a structure with such low damping. The fatigue life prediction calculation is very sensitive to the effective stress range and number of cycles. This is why the weld should be designed to have a constant amplitude fatigue limit higher than the maximum stress range expected.

Table 3.7 Fatigue Life Estimations for Laramie Pole

Damping Ratio (ζ)	0.001	0.002	0.003	0.004	0.005	0.006	0.007
Maximum Stress Range (ΔF) _{max} ksi	30.3	10.2	6.8	5.1	4.1	3.4	2.9
Effective Stress Range (Δf) _{eff} ksi	15.2	5.1	3.4	2.6	2.1	1.7	1.5
Fatigue Life (Y)							
Minimum Life $R_R = 1$	0.01	0.08	0.3	0.68	infinite	infinite	infinite
Evaluation Life $R_R = 1.3$	0.01	0.11	0.37	0.88	infinite	infinite	infinite
Mean Life $R_R = 1.6$	0.02	0.14	0.46	1.1	infinite	infinite	infinite
Mean Life with no threshold restraint	0.02	0.14	0.46	1.1	2.13	3.67	5.82

3.6.3 Comparison to NCHRP 469 Method

As described in Section 0, the AASHTO LTS has simple design equations to address vortex shedding. The method only takes into account one critical velocity and mode of vibration per analysis, but it is recommended that modes 1 and 2 be tested. A reference to NCHRP Report 469 is the only procedure for considering higher modes and tapered sections (NCHRP 2002). The method described was used to evaluate the column stress range in order to compare to the transfer sheet's computation of maximum stress range expected, (ΔF)_{max}. Calculations are shown below. Variables in the calculations are as follows:

f_{n3}	Critical mode frequency	3.9 Hz, as calculated from transfer sheet
D	Critical diameter	0.882 ft, as calculated from transfer sheet
S_n	Strouhal number	0.18 for a cylindrical section
V_c	Critical Velocity	Calculated
C_d	Drag coefficient	1.1 for a cylindrical section
I_f	Importance Factor	1 to compare with CSA transfer sheet
B	Damping Ratio	0.005 to compare with CSA transfer sheet
P_{vs}	Equivalent static pressure range	Calculated
q_{vs}	Distributed load at critical	Calculated
S_{rcol}	Column Stress Range	Calculated

$$f_{n3} := 3.9 \text{ Hz} \quad d := 0.882 \text{ ft} \quad S_n := 0.18 \quad V_c := \frac{f_{n3} \cdot d}{S_n}$$

$$C_d := 1.1 \quad I_f := 1 \quad \beta := .005 \quad P_{vs} := \frac{0.00118 V_c^2 C_d I_f}{2 \cdot \beta}$$

$$P_{vs} = 47.402 \quad V_c = 19.11$$

Vortex shedding will occur over +/- 10% of critical diameter

$$d + .1d = 0.97 \quad d - .1d = 0.794$$

These diameters occur at the heights of 90.2 ft and 104.96 ft

$$q_{vs} := P_{vs} \cdot d \quad q_{vs} = 41.809 \text{ lb/ft}$$

$$M_{\text{base}} := q_{vs} \cdot (104.96 - 90.2) \left(\frac{104.96 - 90.2}{2} + 90.2 \right)$$

$$M_{\text{base}} = 6.022 \times 10^4 \text{ lb-ft}$$

$$M := M_{\text{base}} \cdot \frac{12}{1000} \quad M = 722.592 \text{ k-in}$$

$$I := 1683.5$$

$$S_{\text{rcol}} := \frac{M \cdot \frac{d \cdot 12}{2}}{I} \quad S_{\text{rcol}} = 2.271 \text{ ksi}$$

The calculated value of column stress range, S_{rcol} , of 2.3 ksi can be compared to the calculated values of maximum stress range, $(\Delta F)_{\text{max}}$, calculated by the CSA transfer sheet in Section 0. Using a damping ratio of 0.5%, as used in the NCHRP 469 example, the maximum stress range was calculated by the transfer sheet is 3.2 ksi. For this specific high-mast pole example, both estimates are below the acceptable value of the constant amplitude fatigue limit, 4.5 ksi; however, had the constant amplitude fatigue limit been between 2.3 and 3.2 ksi, as for design category E' (AASHTO 2008), the NCHRP 469 estimate would have been a potentially low.

3.7 Summary and Recommendations

The CSA specifications provide a more detailed and comprehensive analysis of vortex-induced vibrations on high-mast poles than the current AASHTO specifications. This is why the transfer sheet uses the CSA guidelines to calculate maximum displacement, critical mode, height, and wind speed. The transfer sheet incorporates even more detail by including local wind data to estimate critical design characteristics, displacements, base moments, and fatigue life. However, the process is highly dependent on the damping ratio, which is a difficult parameter to estimate. When using the damping ratios obtained from the field pluck test, the CSA outputs for the Laramie pole appear to be too high.

While completing the literature review for VIV, it was discovered that there is currently much discussion on the subject of self-limiting displacement of cylindrical systems. The self-limiting method seemed to be a promising method for high-mast pole wind load predictions, and was therefore further researched in Phase III.

4. PHASE III: SELF-LIMITING VORTEX-INDUCED VIBRATION

4.1 Self-Limiting Vibrations

Williamson and Govardhan in *Vortex-Induced Vibrations* posed the question, “What generic features can be discovered that are applicable to all VIV systems?” (Williamson & Govardhan 2004). These researchers, along with others, have determined that the product of mass and damping ratios can be used to model a self-limiting process that predicts the maximum load effects. This product is referred to as mass-damping ($M*\zeta$). If the limiting load effect can be accurately estimated, then the design can be based upon the maximum response. If the economics and service-level displacements are acceptable at this level of load, then the maximum response can be used.

The calculation of load effects on high-mast poles, given the structural data and wind demographics, can be a tedious process, no matter which analysis process is selected. Results are dependent on input variables, most notably modal damping, which is difficult to estimate. Load effect is inversely proportional to damping and the damping in high-mast poles is typically very small: 0.7% or less. In Phase III, experimental, analytical, and numerical research is outlined with respect to self-limiting maximum response principles. This work is related to a possible design process for high-mast poles.

4.2 Conceptual Framework for Design

For ease of reading, the following diagrams, Figures 4.1 through 4.3, contain all variables that are kept consistent in this research. The system depicted is a high-mast pole subjected to non-uniform flow. The pole is a tapered, flexible, aeroelastic cantilever.

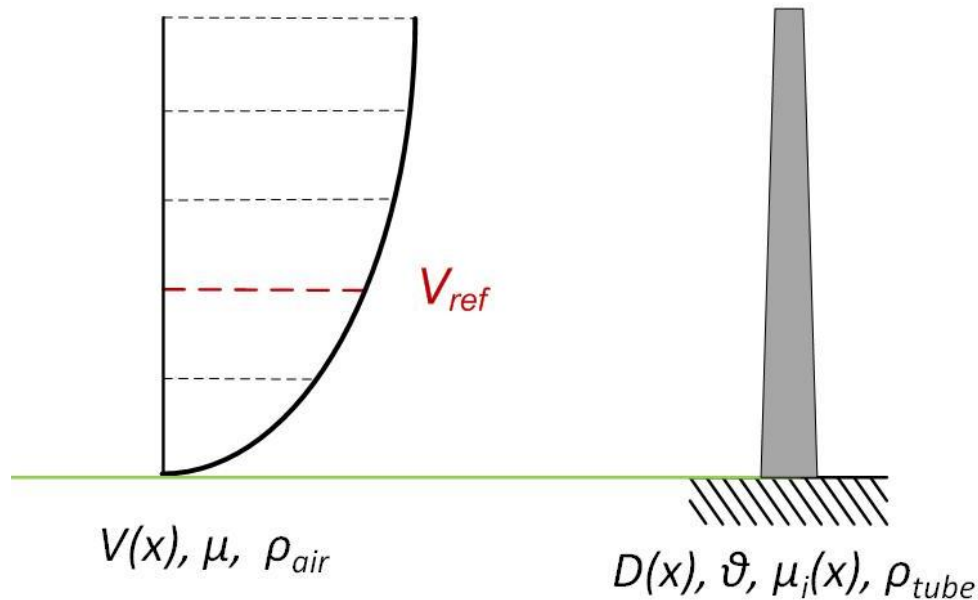


Figure 4.1 Basic System Variables

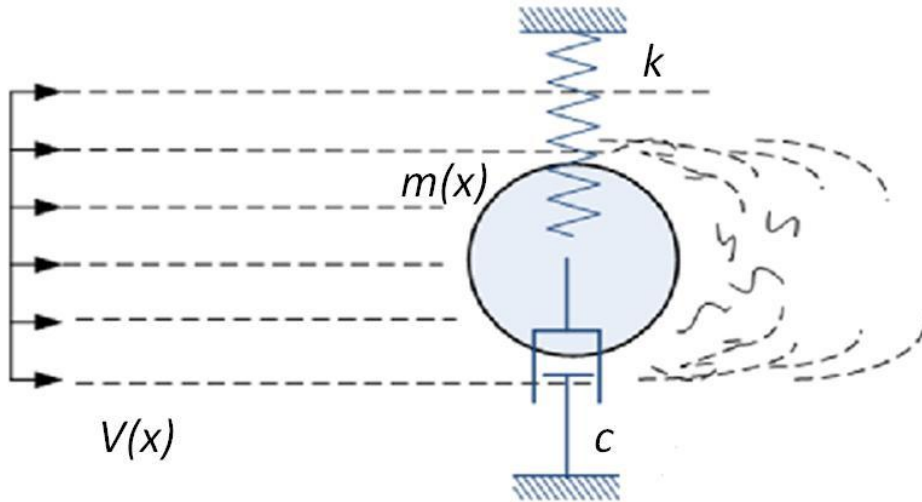


Figure 4.2 Basic System Variables (continued)

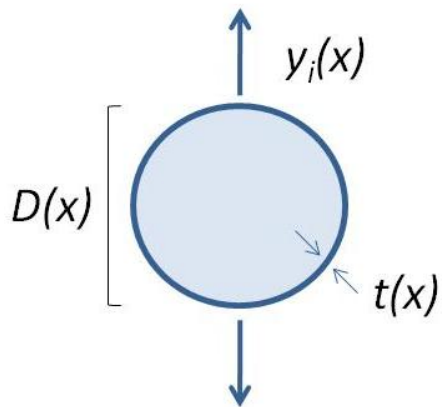


Figure 4.3 Basic System Variables (continued)

Table 4.1 lists the dimensionless variables used in self-limiting estimates.

Table 4.1 Dimensionless Variables

Mass Ratio	M^*	$\frac{\overline{m}(x)}{\pi \rho_{air} \frac{D^2}{4}} = 4 \left(\frac{t}{D(x)} \right) \left(\frac{\rho_{tube}}{\rho_{air}} \right)$
Amplitude Ratio	A^*	$\frac{y_{max}}{D(x)}$
Reynolds Number	R_e	$\frac{\rho_{air} V D}{\mu} = \frac{V D}{\nu}$
Scruton Number	S_c	$\frac{4\pi \overline{m}(x) \zeta_i}{\rho_{air} D^2} = \pi^2 (\zeta_i M^*)$
Strouhal Number	S	$\frac{f_i D}{V}$
Skop-Griffin Parameter	S_G	$2\pi^3 S^2 (M^* \zeta_i)$

where the system parameters are defined in Table 4.2.

Table 4.2 Separate Variables

Mass per Unit Length	$\overline{m}(x)$
Air Density	ρ_{air}
Tube Density	ρ_{tube}
Pole Diameter at height, x	$D(x)$
Pole Thickness at height, x	$t(x)$
Displacement at height, x	$y(x)$
Maximum Displacement	y_{max}
Wind Velocity at height, x	$V(x)$
Coefficient of Fluid Viscosity	μ
Coefficient of Kinematic Fluid Viscosity	ν
Damping Ratio for mode, i	ζ_i
Structural Frequency for mode, i	f_i
Normalizing Factor for mode, i	γ_i
Log decrement of structural damping	δ_i

4.2.1 High-Mast Pole Self-Limiting Dimensionless Variables

In this section, the self-limiting dimensionless variables discussed in Section 0 are determined for two typical poles: the Laramie high-mast pole described in Section 0 and a pole located in south-west Oklahoma. The Oklahoma pole was chosen because of its similar height to the Laramie pole, but with thickness characteristics that differ from the Laramie pole. Specifications for the Oklahoma pole are given in Appendix 0.

The base of the Laramie pole has a 2-foot diameter and 0.313-inch thickness, which tapers to a 0.6-foot diameter and 0.25-inch thickness at the top. With an air density (7200 ft elevation), ρ_{air} , of 0.058 lb/ft³ and a structural density, ρ_{tube} , of 490 lb/ft³, the mass ratio of typical high-mast poles can vary from 350 to over 1000, as illustrated in Table 4.3. The ratio is an important parameter in the prediction of maximum possible load effect. It is interesting to note that if the fluid is water, the mass ratio is typically less than 1. This clearly illustrates a significant and important difference in studying and comparing the research from hydrodynamic and aerodynamic cases.

Table 4.3 Mass Ratios for Laramie Pole

Thickness (in)	0.313	0.313	0.250	0.250	0.375	0.375
Diameter (in)	24	12	24	12	24	12
γ_{air} (lb/ft ³)	0.058	0.058	0.058	0.058	0.058	0.058
γ_{tube} (lb/ft ³)	490	490	490	490	490	490
M*	440	880	352	704	528	1056

The base of the Oklahoma pole has a 21.3-inch diameter and 0.1875-inch thickness, which tapers to a 5-inch diameter and 0.1793-inch thickness at the top. With a sea-level ρ_{air} of 0.076 lb/ft³ and a ρ_{tube} of 490 lb/ft³, the mass ratio of typical high-mast poles can vary from 227 to 967, as illustrated in Table 4.4. The mass ratios of the Oklahoma pole are less than those of the Laramie pole because of the smaller thickness and diameter.

Table 4.4 Mass Ratios for Oklahoma Pole

Thickness (in)	0.188	0.188	0.179	0.179
Diameter (in)	21.3	5	5	21.3
γ_{air} (lb/ft ³)	0.076	0.076	0.076	0.076
γ_{tube} (lb/ft ³)	490	490	490	490
M*	228	970	925	217

The Strouhal number for a multi-sided tube, such as the high-mast, is taken as 0.18, as suggested by the CSA Specifications (CSA 2006). The Scruton number for the Laramie Pole can vary from a low value of 3.5 with a low damping ratio of 0.1% to a high value of 73 with a damping ratio of 0.7%, as shown in Table 4.5. These values lead to a range of Skop-Griffin parameters of 0.7 to 14.9, which is dependent on the damping ratio. The Oklahoma pole has Skop-Griffin values that range from 0.4 to 13.6, as shown in Table 4.6. The theory of the mass ratio and Skop-Griffin parameter are discussed in Sections 0 and 0.

Table 4.5 Skop-Griffin Values for Laramie Pole

	Low $M^* = 352$							High $M^* = 1056$						
ζ (damping ratio)	0.001	0.002	0.003	0.004	0.005	0.006	0.007	0.001	0.002	0.003	0.004	0.005	0.006	0.007
$M^*\zeta$ (mass-damping)	0.35	0.70	1.06	1.41	1.76	2.11	2.46	1.06	2.11	3.17	4.22	5.28	6.34	7.39
S (Strouhal)	0.18	0.18	0.18	0.18	0.18	0.18	0.18	0.18	0.18	0.18	0.18	0.18	0.18	0.18
S_c (Scrouton)	3.5	6.9	10.4	13.9	17.4	20.8	24.3	10.4	20.8	31.3	41.7	52.1	62.5	73.0
S_G (Skop Griffin)	0.7	1.4	2.1	2.8	3.5	4.2	5.0	2.1	4.2	6.4	8.5	10.6	12.7	14.9

Table 4.6 Skop-Griffin Values for Oklahoma Pole

	Low $M^* = 217$							High $M^* = 970$						
ζ (damping ratio)	0.001	0.002	0.003	0.004	0.005	0.006	0.007	0.001	0.002	0.003	0.004	0.005	0.006	0.007
$M^*\zeta$ (mass-damping)	0.22	0.43	0.65	0.87	1.09	1.30	1.52	0.97	1.94	2.91	3.88	4.85	5.82	6.79
S (Strouhal)	0.18	0.18	0.18	0.18	0.18	0.18	0.18	0.18	0.18	0.18	0.18	0.18	0.18	0.18
S_c (Scrouton)	2.1	4.3	6.4	8.6	10.7	12.9	15.0	9.6	19.1	28.7	38.3	47.9	57.4	67.0
S_G (Skop Griffin)	0.4	0.9	1.3	1.7	2.2	2.6	3.1	1.9	3.9	5.8	7.8	9.7	11.7	13.6

For the purpose of further calculations, the mass ratio and Skop-Griffin are computed at the critical height of each pole. As calculated in Section 0, the critical height of both the Laramie pole and the Oklahoma pole is 97.6 feet. The thickness for the Laramie pole at this height is 0.2391 inches and the diameter is 10.6 inches. The thickness for the Oklahoma pole is 0.1793 inches and the diameter is 8.3 inches. These values produce a mass ratio of 762 for the Laramie pole and 557 for the Oklahoma pole. The Skop-Griffin values were calculated for a range of damping ratios, as shown in Table 4.7 and Table 4.8.

Table 4.7 Skop-Griffin Values for Critical Height of Laramie Pole

ζ (damping ratio)	0.001	0.002	0.003	0.004	0.005	0.006	0.007
S (Strouhal)	0.18	0.18	0.18	0.18	0.18	0.18	0.18
S_c (Scrouton)	7.5	15.0	22.6	30.1	37.6	45.1	52.7
S_G (Skop Griffin)	1.5	3.1	4.6	6.1	7.7	9.2	10.7

Table 4.8 Skop-Griffin Values for Critical Height of Oklahoma Pole

ζ (damping ratio)	0.001	0.002	0.003	0.004	0.005	0.006	0.007
S (Strouhal)	0.18	0.18	0.18	0.18	0.18	0.18	0.18
S_c (Scrouton)	5.50	11.00	16.50	21.99	27.49	32.99	38.49
S_G (Skop Griffin)	1.12	2.24	3.36	4.48	5.60	6.72	7.84

These values provide a context for the discussion of theoretical and empirical models. Note that research results from hydroelastic and aeroelastic studies are often combined. However, the mass-damping and Skop-Griffin parameters are significantly different between these two important applications, and the amplitudes associated with VIV are significantly different as well, which is dominant in the prediction of maximum load effects.

4.3 Theoretical Models

The Skop-Griffin parameter was derived through an attempt to estimate responses of a cylinder under VIV given the physical parameters (Griffin, 1973). Griffin notes at that year, although there were many empirical formulas available, these were not adequate for use in real engineering systems:

*First, the existing experimental observations are only qualitatively predicted.
Second, no relations have been developed between the empirical constants in the model, which vary considerably from experiment to experiment, and the physical constants of the system under study (Griffin 1973).*

Using the Van der Pol equation as the governing equation for lift force, the equation of motion, and the data collected from various experiments, relations between the empirical values and physical parameters were determined. The parameters were eventually combined and given the name Skop-Griffin parameter, S_G (Williamson & Govardhan 2004).

Another set of published articles that attempts to connect physical parameters of a system to an amplitude prediction are those of Goswami, Scanlan, and Jones (Goswami, Scanlan & Jones 1993). The work cited discusses previous attempts of purely mathematical analysis of VIV and states that, “Such a solution remains elusive to date,” (Goswami, Scanlan & Jones 1993). The seemingly impossible task of developing a theoretical model of VIV leads many researchers to use a combination of mathematical derivation and empirical estimation from experimental data. The research model is developed from the single degree of freedom (SDOF) models of Scanlan and Simiu (Simiu & Scanlan 1986) and Billah (Billah 1989), as well as collection of wind-tunnel data. The model, although accurate in predictions of varying damping systems, requires the input of many aeroelastic terms, both linear and nonlinear, which was decided to be beyond the scope of high-mast poles and of this research.

4.4 Experimental Research

Many researchers have tried to determine dimensionless variables that predict the maximum Amplitude Ratios A^* (Table 4.9). One of the more popular findings is the Skop-Griffin parameter (S_G), which is defined in Table 4.9. Figure 4.4 shows a frequently cited version of the Griffin plot with data taken from marine cylindrical tube experiments. The data are presented with an early version of the Skop-Griffin parameter, $\frac{\zeta_s}{\mu}$ where

$$\mu = \frac{\pi \rho_{tube} D^2}{8\pi^3 S^2 m} = \frac{1}{2\pi^3 S^2 M^*} \quad (19)$$

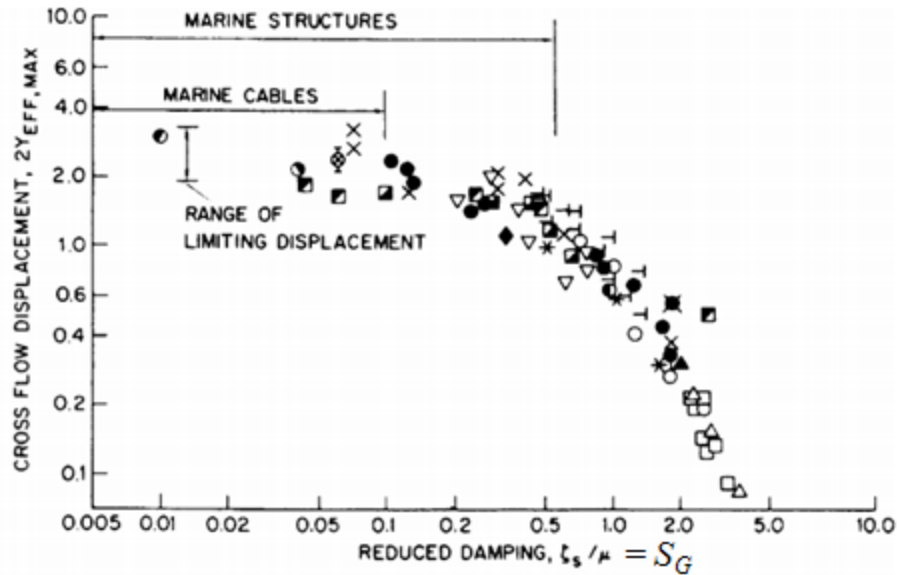


Figure 4.4 Griffin-Plot with Early Skop-Griffin Parameter (Griffin 1980)

Griffin noted the difference of behavior when experiments are conducted in air as shown in Figure 4.5 (Griffin 1984). The results show that the amplitude is independent of mode but highly sensitive to change in the reduced damping parameter chosen. The data shown are typical for cylinders tested in air and behave similar to the data toward the right side of Figure 4.4. Several versions of best-fit lines have been estimated for aerodynamic tested data, such as the one shown in Figure 4.5, and are discussed in Section 0.

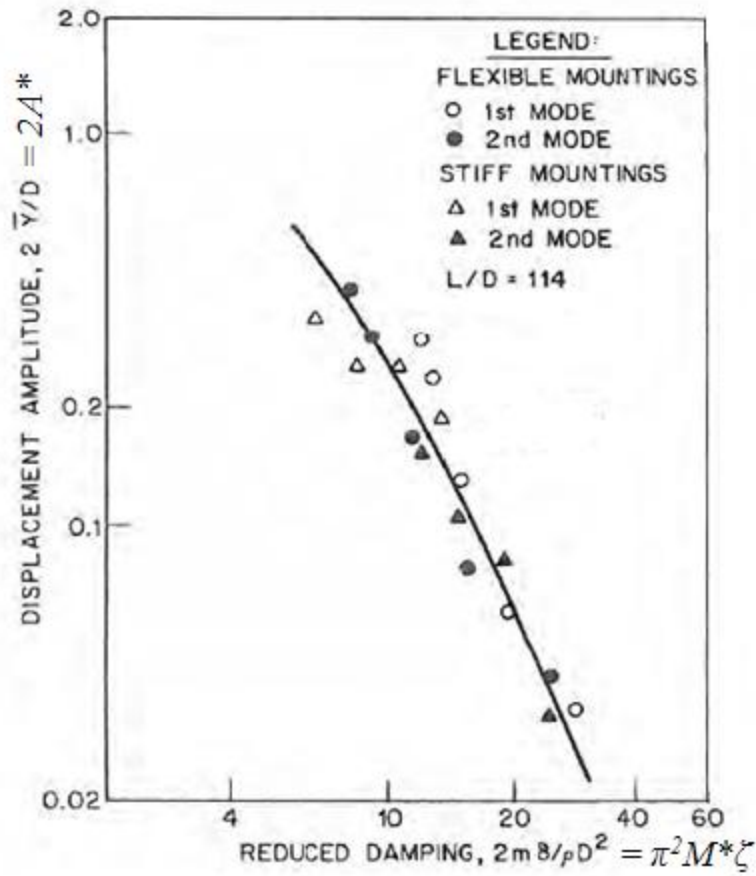


Figure 4.5 Displacement Amplitude for Flexible Cylinders in a Wind Tunnel (Griffin 1984)

In an effort to illustrate the reliability of the Skop-Griffin parameter, Williamson and Govardhan plotted a number of different experimental data, including those using air as a medium and those using water. The outcome is illustrated in Figure 4.6. The data are from the experiments of Skop and Balasubramanian in 1997 and those detailed in Table 4.9. The added best-fit line is discussed in Section 0.

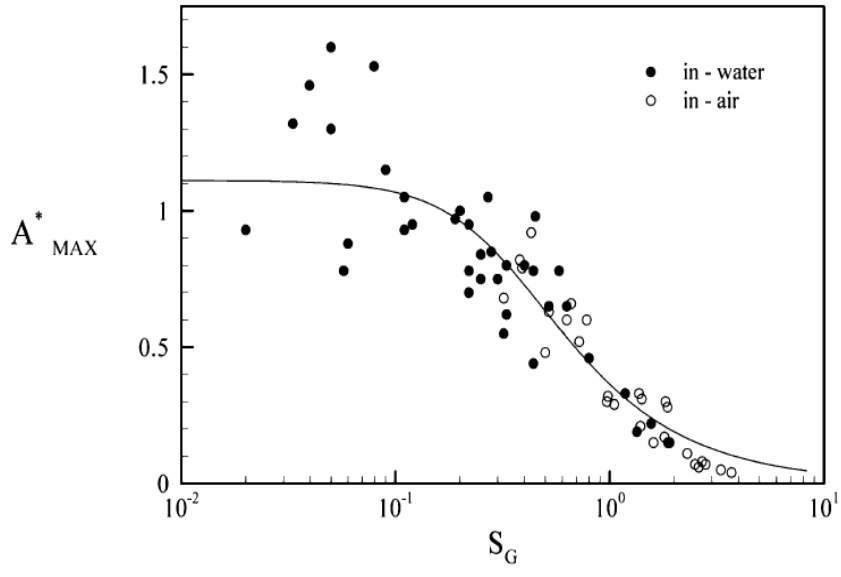


Figure 4.6 Griffin-Plot with Data (Williamson & Govardhan 2004)

Table 4.9 Peak Amplitude Ratio Data (Williamson & Govardhan 2004)

Investigators	Year	Medium	Re	$m^* \zeta$	A^* (peak)
<i>(A) Elastically-mounted rigid cylinders (Y-only)</i>					
Angrilli et al.	1974	Water	2,500–7,000	0.049	0.54
Dean et al. (1)	1977	Water	2,800–10,200	0.0055	0.94
Moe & Overvik	1982	Water	6,000–30,000	0.013	1.09
Anand & Torum	1985	Water	6,500–35,000	0.013	1.07
Sarpkaya	1995	Water	6,000–35,000	0.052	0.95
Gharib et al.	1998	Water	11,000–40,000	0.094	0.84
Hover et al. (2)	1998	Water	3,800	0.040	0.80
Khalak & Williamson	1999	Water	5,000–16,000	0.0047	1.18
Govardhan & Williamson	2000	Water	2,900–19,000	0.0027	1.19
Vikestad et al.	2000	Water	14,000–65,000	0.012	1.13
Owen et al.	2001	Water	1,650–7,500	0.036	0.84
Jauvtis & Williamson	2003a	Water	5,000–13,000	0.0048	1.13
<i>(B) Elastically mounted rigid cylinders (XY-motion) (3)</i>					
Jauvtis & Williamson	2003c	Water	7,200–15,400	0.0064	1.50
<i>(C) Cantilevers and Pivoted Cylinders</i>					
Vickery & Watkins (4)(5)	1964	Water	7,000	0.016	1.46
King (5)	1974	Water	6,000–22,500	0.020	1.60
Pesce & Fujarra (5)	2000	Water	6,000–40,000	0.013	1.32
Fujarra et al. (5)(6)	2001	Water	1,000–2,500	0.023	0.78
Flemming & Williamson (7)	2003	Water	500–2,000	0.032	1.53
<i>(D) Forced oscillations of cylinders (Amplitude limit of positive excitation)</i>					
Mercier	1973	Water	2,000–33,000		1.10
Sarpkaya	1978	Water	5,000–25,000		0.90
Hover et al.	1998	Water	3,800		0.82
<i>(E) Low-Re experiments</i>					
Anagnostopoulos & Bearman	1992	Water	90–150	0.179	0.55
<i>(F) Direct Numerical Simulation (DNS)</i>					
Blackburn & Karniadakis (8)	1993	2-D Code	200	0.012	0.64
Newman & Karniadakis (8)	1995	2-D Code	200	0.00	0.65
Shiels et al.	2001	2-D Code	100	0.00	0.59
Fujarra et al.	1998	2-D Code	200	0.015	0.61
Guilmineau & Queutey	2000	2-D Code	100	0.179	0.54
Blackburn et al.	2001	2-D Code	430–560	0.122	0.47
Evangelinos & Karniadakis	1999	3-D Code	1,000	0.00	0.74
<i>(G) Turbulence Models (LES and RANS)</i>					
Saltara et al. (LES)	1998	2-D Code	1,000	0.013	0.67
Guilmineau & Queutey (RANS)	2002	2-D Code	3,800	0.013	0.98

Notes regarding these collected data.

(1) Amplitude response plots show multiple peaks and large scatter.

(2) Virtual free-vibration experiments using real-time force-feedback control system.

(3) Cases where oscillating mass and natural frequency in both directions are identical.

(4) Vickery & Watkins performed experiments with an adjustable cantilever/pivoted cylinder, and not simply a pivoted cylinder (as usually quoted).

(5) The peak A/D here is less than the tip amplitude, and uses a modal parameter as defined in Griffin, Skop & Ramberg (1975).

(6) Restricted to transverse Y-motion only.

(7) Pivoted cylinder with two degrees of freedom.

(8) X-Y motions were simulated (two degrees of freedom).

Williamson and Govardhan also compiled data from previous research to investigate the existence of a critical mass ratio. The data were also combined from sources listed in Table 4.10 with symbols corresponding as follows:

- △ Khalak & Williamson (1999)
- Govardhan & Williamson (2000)
- Anand (1985)

Another well-known collection of aerodynamically tested data was by Blevins (1984) and is shown in 4.7. The data include a range of systems, as well as modes, and is collapsed by another damping parameter. The damping parameter can be simplified to $M^*\zeta$. The theory line is discussed in Section 0 (Blevins 1984).

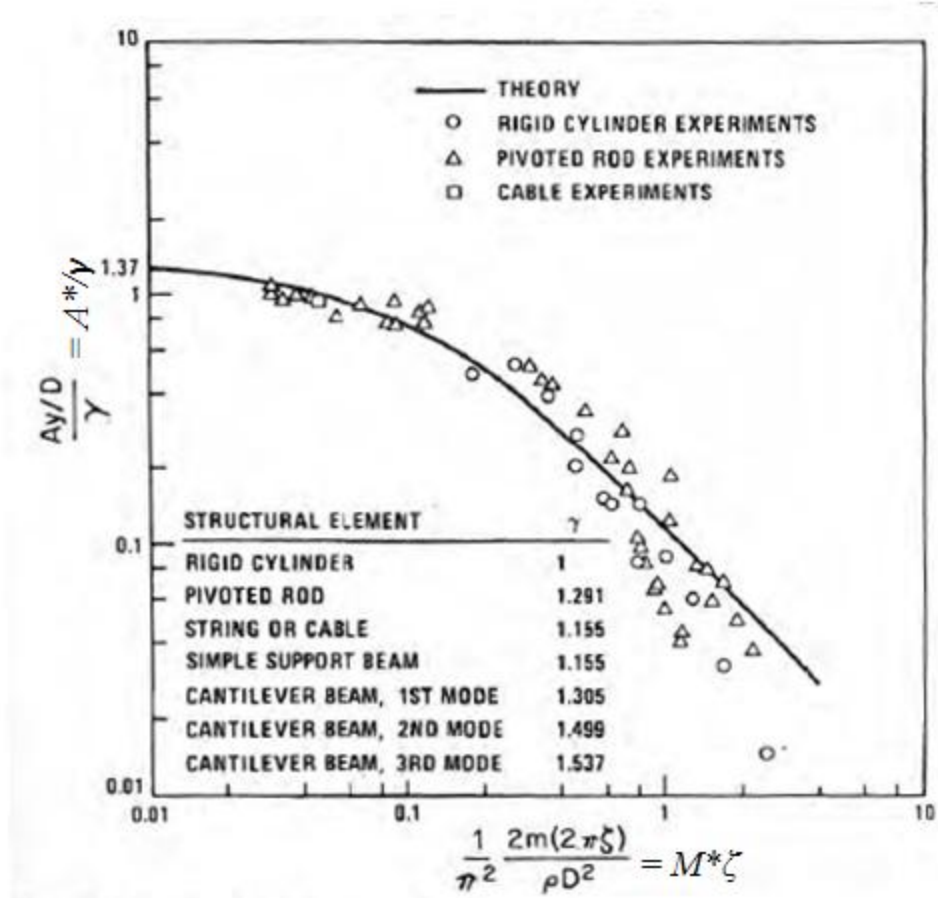


Figure 4.7 Maximum Amplitude of VIV as a function of Damping (Blevins 1984)

4.4.1 Empirical Models

The following section summarizes the empirical models that have been made to fit the experimental research discussed in Section 0. Some of the models have been simplified, as shown in Equation 20b, to illustrate the use of the dimensionless variables described in Table 4.1.

For Figure 4.5 (Griffin 1984)

$$A^* = \frac{1.29\gamma_i}{\left[1 + 0.43 \left(4\pi \frac{S^2 \bar{m} \delta}{\rho D^2}\right)\right]^{3.35}} \quad (20)$$

where

γ_i = normalizing factor
 δ = log decrement of structural damping
 ρ = fluid density

$$A^* = \frac{1.29\gamma_i}{\left[1 + 0.43(S_G)\right]^{3.35}} \quad (20b)$$

For Figure 4.6 (Williamson & Govardhan 2004)

$$A^* = \frac{B}{\sqrt{C + S_G^2}} \quad (21)$$

where

B, C = constants related to the force coefficient, determined by best-fit as 0.385 and 0.12 for the data

For Figure 4.7 (Blevins 1984)

$$A^* = \frac{0.07\gamma}{(\delta_r + 1.9)S^2} \left(0.3 + \frac{0.72}{(\delta_r + 1.9)S}\right)^{\frac{1}{2}} \quad (22)$$

where

$$\delta_r = \frac{2m(2\pi\zeta)}{\rho D^2} = S_c$$

The dimensionless variables used to collapse the A^* plots all simplify to the expression of:

$$a \times M^* \zeta \quad (23)$$

where a is a constant variable usually containing π and/or the Strouhal number. Because of these common variables, it is not surprising that Griffin should state that the best-fit lines are, "...virtually identical prediction curves derived by different methods," (Griffin 1984). Even the CSA prediction method discussed in sections 0 and 0 can be simplified if the integral in the modal coefficient of magnitude is assumed to be a mode shape weighted diameter variable. The amplitude ratio could be determined as,

$$A^* = \frac{1}{2.86S_G} \quad (24)$$

4.4.2 Empirical Models for Laramie and Oklahoma Poles

The empirical models listed in Section 0 were applied to both the Laramie and Oklahoma high-mast poles for a range of damping ratios from 0.1% to 0.7%. The specifications for these poles are available in appendices 0 and 0. The empirical predictions are shown in Figure 4.8 and Figure 4.9.

For the Laramie pole, the highest amplitude ratio predicting empirical model is Blevin's. The CSA transfer sheet predicts values even higher. The lowest amplitude ratio predicting model is the Griffin model. The one field data point in Figure 4.8 represents the maximum amplitude of vibration measured by Ahearn for the Laramie pole at an estimated damping ratio of 0.1%. Although the data point appears to be low compared with the empirical models, since Ahearn was not able to collect data continuously, there may have been higher amplitudes of vibration in the pole. The estimation of damping ratio is also difficult, as discussed in Section 0.

For the Oklahoma pole, the highest amplitude ratio predicting model is the Griffin model, until the S_G parameter is above 4, in which case Blevin's model becomes the highest. The CSA transfer sheet predicts values below Blevin's model for the Oklahoma pole. The Williamson model predicts the lowest amplitude ratio values for the Oklahoma pole up to an S_G value of 6.

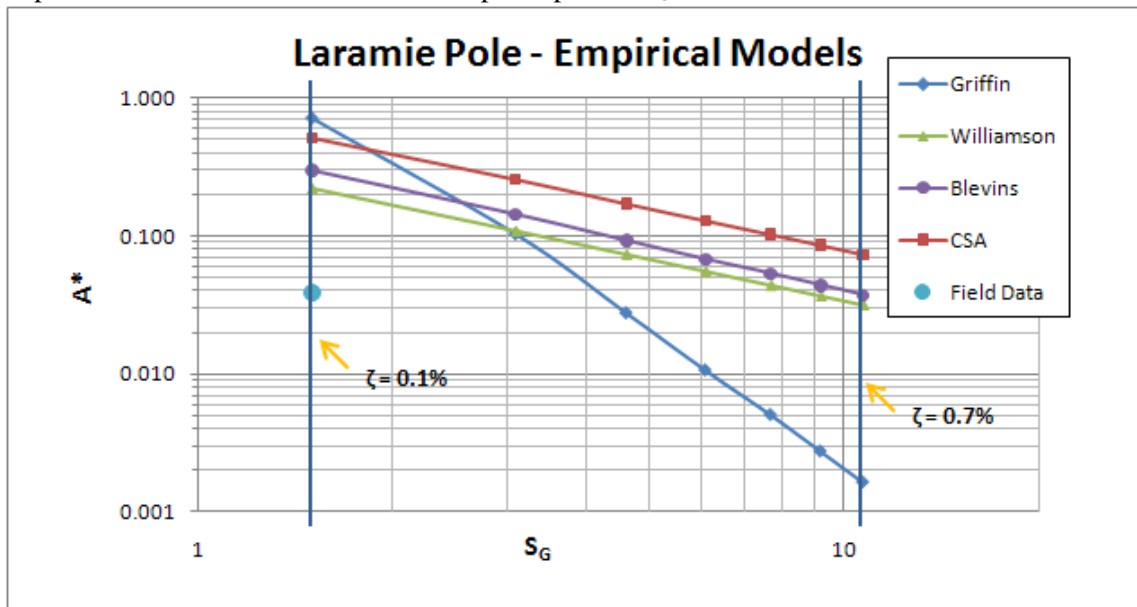


Figure 4.8 Empirical Models for Laramie High-Mast

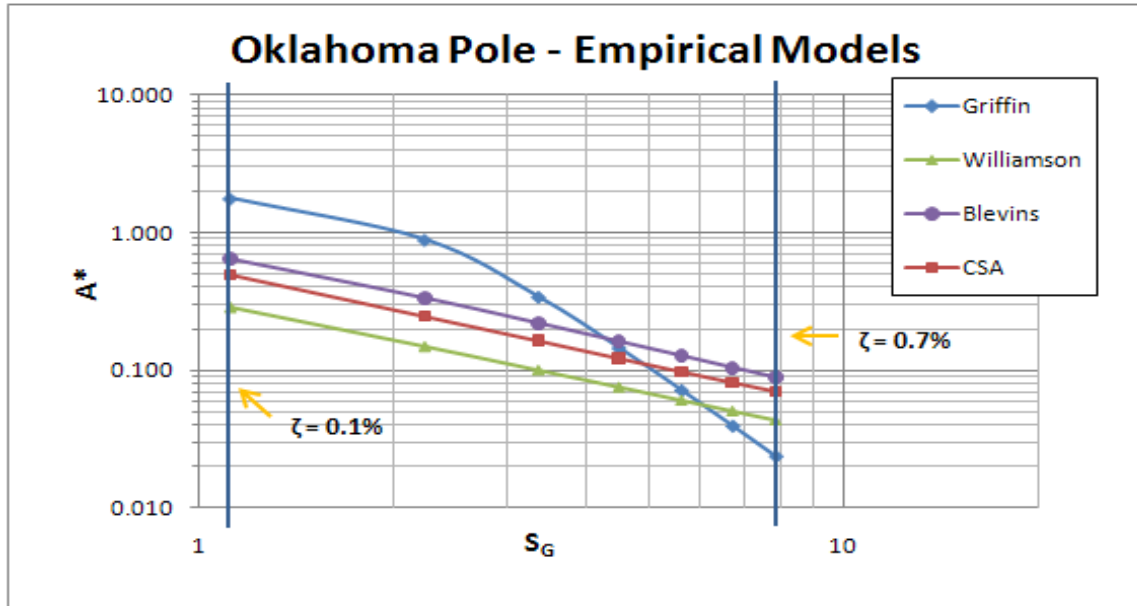


Figure 4.9 Empirical Models for Oklahoma High-Mast

4.4.3 Stress Range Estimations from Self-Limiting VIV Amplitudes

Figure 4.10 and Figure 4.11 show the pole peak base stress estimated by the empirical models. As for the computations of maximum amplitude ratio, a range of damping ratios between 0.1% to 0.7% were used. The figures are proportional to the maximum amplitude ratio figures because the maximum displacement is proportional to the peak base stress. The NCHRP example calculations for the Laramie pole were also added to Figure 4.10.

To evaluate the accuracy of each of the models, they are compared to the CSA model and the constant amplitude fatigue threshold of the high-mast pole design category, which is 4.5 ksi. For the Laramie pole, the CSA model predicts that the peak base stress will fall under 4.5 ksi as long as the damping ratio is above 0.4%. The other models predict closely to the CSA model, excluding the Griffin model with its slight vertical shift. For example, the Blevins and Williamson models predict that a damping ratio between 0.2% and 0.3% would predict adequate stress ranges.

The Oklahoma pole empirical predictions show different results. The Williamson model suggests that the peak base stress would not fall below 4.5 ksi unless a damping ratio of at least 0.5% is met. The Blevins model suggests that even at 0.7%, the peak base stress is not below 4.5 ksi. This illustrates the sensitivity of each model to the mass-damping parameter.

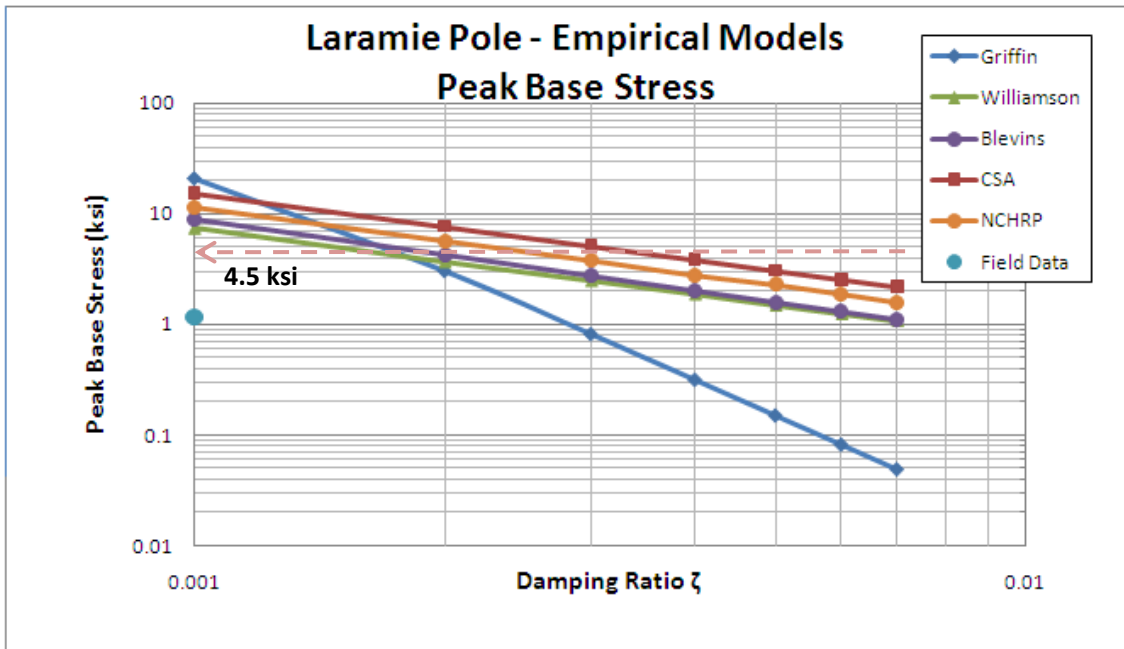


Figure 4.10 Empirical Model Peak Base Stress for Laramie High-Mast

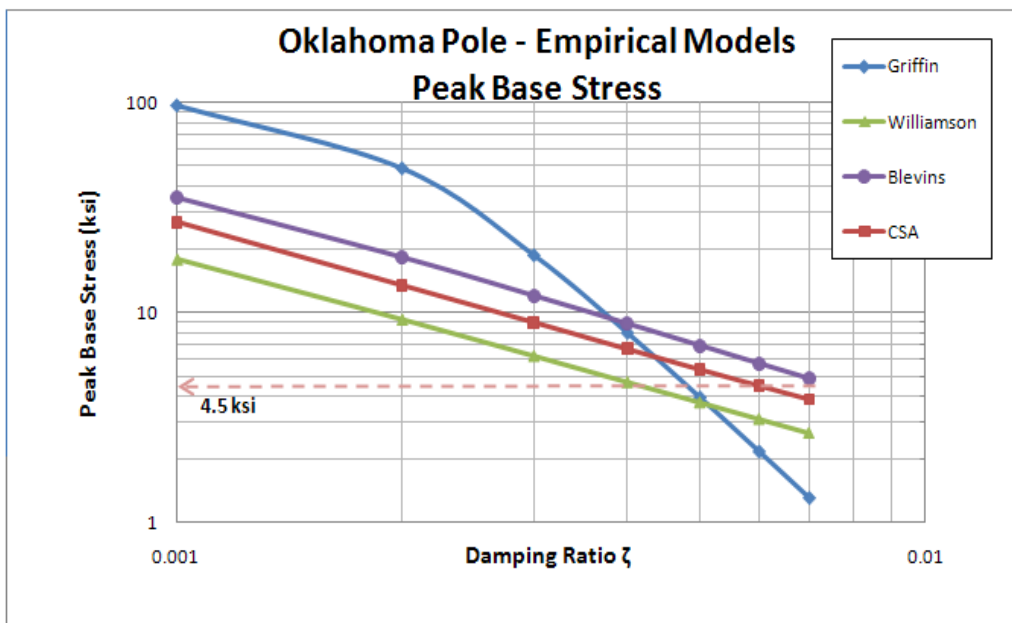


Figure 4.11 Empirical Model Peak Base Stress for Oklahoma High-Mast

4.5 Summary and Recommendations

The use of self-limiting estimations for the design of high-mast poles shows potential. All three of the empirical models tested give reasonable results. As a method for peak base stress, the self-limiting methods required much less input than the CSA transfer sheet used in Phase II. However, all of the empirical models are inversely proportional to the damping ratio, which, as discussed in Section 0, is very difficult to estimate.

In order to establish a design procedure, more pole data needs to be collected to validate the accuracy of an empirical model. By collecting data from poles with varying mass-damping parameters, a design model can be created. This would allow a user to calculate a maximum amplitude ratio based upon the damping ratio, and from this, a peak base stress based upon modal analysis.

5. SUMMARY AND RECOMMENDATIONS

5.1 Summary

In Phase I of this research, the previous studies of Price (Price 2009) were continued through the sending of surveys to state bridge engineers for the collection of more data. The data collected were locations of cracked traffic-signal and high-mast poles across the country. The data collected were organized by state and compared to wind power (WPC) maps. The data collected agreed with Price's prediction that, although traffic-signal pole cracking primarily occurred in high WPC areas, high-mast cracking did not. This led to the research of vortex-induced vibrations (VIV) in Phase II.

After a comparison of the current AASHTO specifications (AASHTO 2009) and the CSA specifications (CSA 2006) in their design of high-mast poles to resist VIV, it was determined that the latter dedicated more detail to the analysis. Therefore, the CSA equations were chosen to create a numerical tool called a transfer sheet. The transfer sheet uses input of structural and dynamic pole characteristics, as well as local wind data, to create output of the critical wind speed, critical mode, critical height, peak stress range, and estimated fatigue life of the pole. A high-mast pole in Laramie, Wyoming, was run through the transfer sheet, as well as a year's worth of wind data from a local wind station. The output was compared with the data collection from a previous UW study by Ahearn (Ahearn 2010). The comparison showed that the transfer sheet estimations of critical mode and height were accurate; however, the estimations of maximum displacement seemed to be high. This was difficult to conclude, however, as Ahearn was unable to collect data consistently and the pole may have seen higher displacements.

Review of past research led to the study of developing a possible design criteria based on self-limiting vibrations in high-mast poles. Three empirical models were chosen to estimate the maximum amplitude ratio of the Laramie pole and a pole located in Oklahoma. The Oklahoma pole was chosen because of its height, which is the same as the Laramie pole, and its thickness and diameter, which were less than the Laramie pole. Although the three empirical models estimated reasonable amplitude ratios for both poles, they were not consistent between each. Therefore, it was concluded that in order to establish a design procedure, an empirical model needs to be developed based on the collection of more high-mast data.

5.2 Recommendations

Although the research of Price has been continued through the collection of more data, there are still many states missing in the survey (Price 2009). The high amount of cracking locations reported in Colorado need to be more deeply investigated due to the low reliability rating of the area. Surveys need to be sent to the states that have not replied with data in order to further prove Price's predictions. (Johnson 2011)

The accuracy of the CSA transfer sheet could not be validated in Phase II. If compared strictly to the data collected by Ahearn, the sheet would appear to be overestimating the responses (Ahearn 2010). However, since Ahearn was not able to continuously collect data, this conclusion cannot be made. The transfer sheet output needs to be compared to a more complete data collection in order to be fully validated.

The subject of VIV on cylindrical sections is very popular in current research. With the construction of more wind tunnels for data collection, more empirical models will be created. The literature review completed for Phase III did not include all published articles that are available on this subject. It is recommended that poles with varying mass-damping characteristics be continuously monitored, in which case the data could be used to create an empirical equation for design.

6. BIBLIOGRAPHY

- Station: Laramie General Brees Field, WsID 21834. (2004-2009). Weather Source .
- Windographer 2.2. (2010). Mistaya Engineering.
- AASHTO. (2001). *Standard specifications for structural supports for highway signs, luminaires, and traffic signals* (Vol. 4th). Washington, District of Columbia: American Association of State Highway and Transportation.
- AASHTO. (2008). *Manual for Bridge Evaluation*. Washington, District of Columbia: American Association of State Highway and Transportation.
- AASHTO. (2009). *Standard specifications for structural supports for highway signs, luminaires, and traffic signals* (Vol. 5th). Washington, District of Columbia: American Association of State Highway and Transportation.
- AASHTO. (2010). *LRFD Bridge Design Specifications*. Washington, District of Columbia: American Association of State Highway and Transportation.
- Ahearn, E. (2010). *Reduction of Wind-Induced Vibrations in High-Mast Light Poles*. Laramie: University of Wyoming.
- Billah, K. (1989). *A Study of Vortex-Induced Vibration*. Princeton, NJ: Princeton University.
- Blevins, R. (1984). *Flow-Induced Vibration*. Malibar, Florida: Kreiger.
- Brakke, B. (2009, July 23). "Request for Information Regarding Sign/Signal Support Structures and Highmast Lighting Towers." Message to Dr. Jay Puckett . E-Mail.
- Chang, B., B. Phares, P. Sarkar, & T. Wipf. (2009). "Development of a procedure for fatigue design of slender support structures subjected to wind induced vibration." *TRB 2009 Annual Meeting CD-ROM*.
- CSA. (2006). *Canadian Highway Bridge Design Code*. Mississauga, Ontario, Canada: Canadian Standards Association .
- EIS, W. E. (2004). *Wind Energy Maps*. Retrieved 2011, from <http://windeis.anl.gov/guide/maps/index.cfm>
- Elliott, D., C. Holladay, W. Barchet, H. Foote, & W. Sandusky. (1986). *Wind Energy Resource Atlas of the United States*. (N. R. Labratory, Producer) Retrieved 2011, from <http://rredc.nrel.gov/wind/pubs/atlas/>
- Goode, J. & J. van de Lindt. (2007). Development of a Semiprescriptive Selection Procedure for Reliability-Based Fatigue Design of High-Mast Lighting Structural Supports. *Journal of Performance of Constructed Facilities*, 193-206.
- Goswami, I., R. Scanlan, & N. Jones. (1993). Vortex-Induced Vibration of Circular Cylinders. II: New Model. *Journal of Engineering Mechanics*, 2288-2302.

- Griffin, O. (1973). A Model for the Vortex-Excited Resonant Response of Bluff Cylinders. *Journal of Sound and Vibration*, 225-233.
- Griffin, O. (1980). Vortex-Excited Cross-flow Vibrations of a Single Cylindrical Tube. *ASME Journal of Pressure Vessel Technology*, 102, 158-66.
- Griffin, O. (1984). *Vibrations and Flow-Induced Forces Caused by Vortex Shedding*. Washington, DC: Marine Technology Division, Naval Research Laboratory.
- Harris, C.M. (1961). *Shock and Vibration Handbook*. New York: McGraw-Hill Book Company.
- Johnson, R. (2011). "Study of the Effect of Wind Power and Vortex-Induced Vibrations to Establish Fatigue Design Criteria for High-Mast Poles," in partial fulfillment of the requirement for the master's degree, University of Wyoming, Laramie, WY.
- Lienard, J. (1966). *Synopsis of Lift, Drag and Vortex Frequency Data for Rigid Circular Cylinder*. Washington State University, College of Engineering, Research Division Bulletin 300.
- Lienhard, J.H. (1966). *Synopsis of Lift, Drag and Vortex Frequency Data for Rigid Circular Cylinders*. Washington State University, College of Engineering, Research Division Bulletin 300.
- NCHRP. (2002). *NCHRP Report 469: Fatigue-Resistant Design of Cantilevered Signal, Sign, and Light Supports*. Washington, D.C.: National Academy Press.
- Phares, B., P. Sarkar, T. Wipf, & B. Chang. (2007). "Development of Fatigue Design Procedures for Slender, Tapered Support Structures for Highway Signs, Luminaries, and Traffic Signals Subjected to Wind-Induced Excitation from Vortex-Shedding and Buffeting." *Midwest Transportation Consortium*.
- Price, R.P. (2009). *Use Of Wind Power Maps To Establish Fatigue Design Criteria For Cantilever Traffic Signal Structures*. January: Proceedings Annual Transportation Research Board.
- Simiu, T. & R. Scanlan. (1986). *Wind Effects on Structures*. New York, NY: John Wiley and Sons.
- Techet, A. (2005). *Design Principles for Ocean Vehicles*. Retrieved 2011, from MIT OpenCourseWare: <http://ocw.mit.edu/courses/mechanical-engineering/2-22-design-principles-for-ocean-vehicles-13-42-spring-2005>
- Williamson, C. & R. Govardhan. (2004). "Vortex-Induced Vibrations." *Annu. Rev. Fluid Mech.*, 413-55.

7. APPENDIX

7.1 WIND POWER CLASSIFICATION MAPS

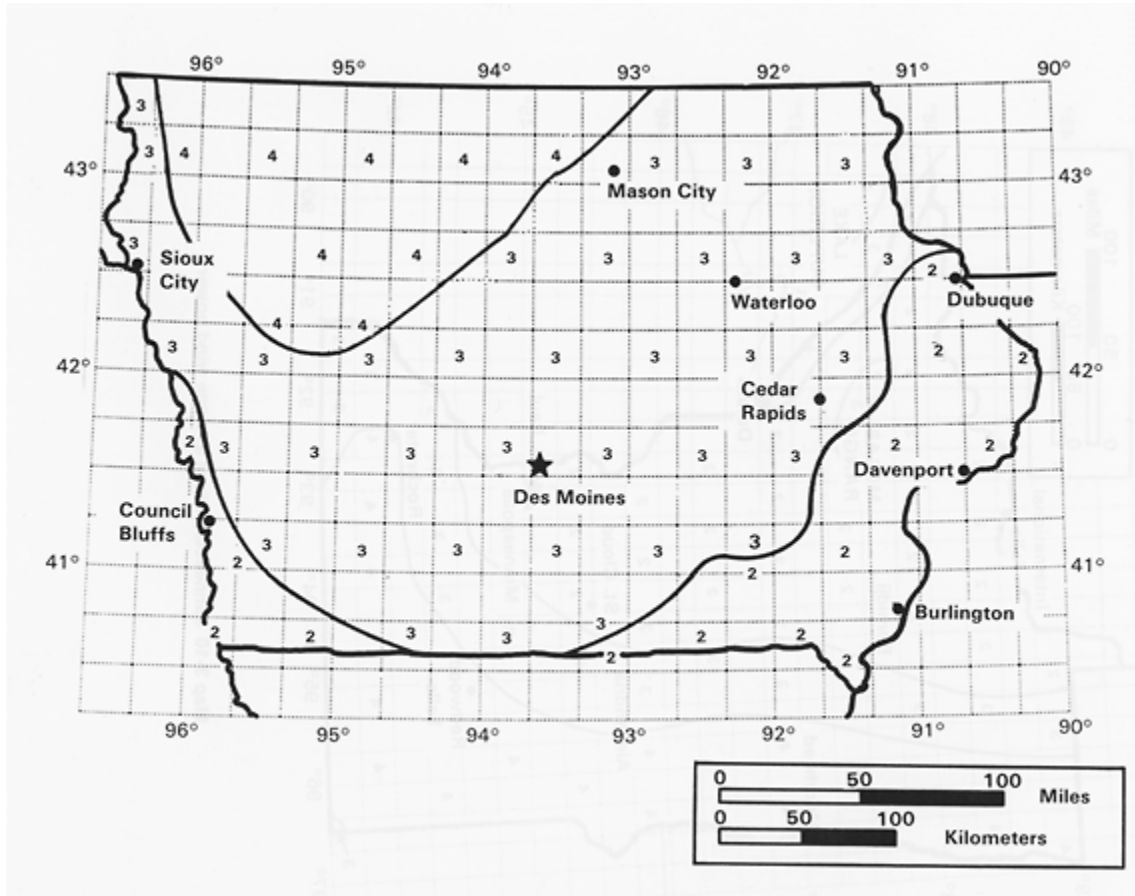


Figure 7.1 Iowa WPC (Elliott, Holladay, Barchet, Foote, & Sandusky 1986)

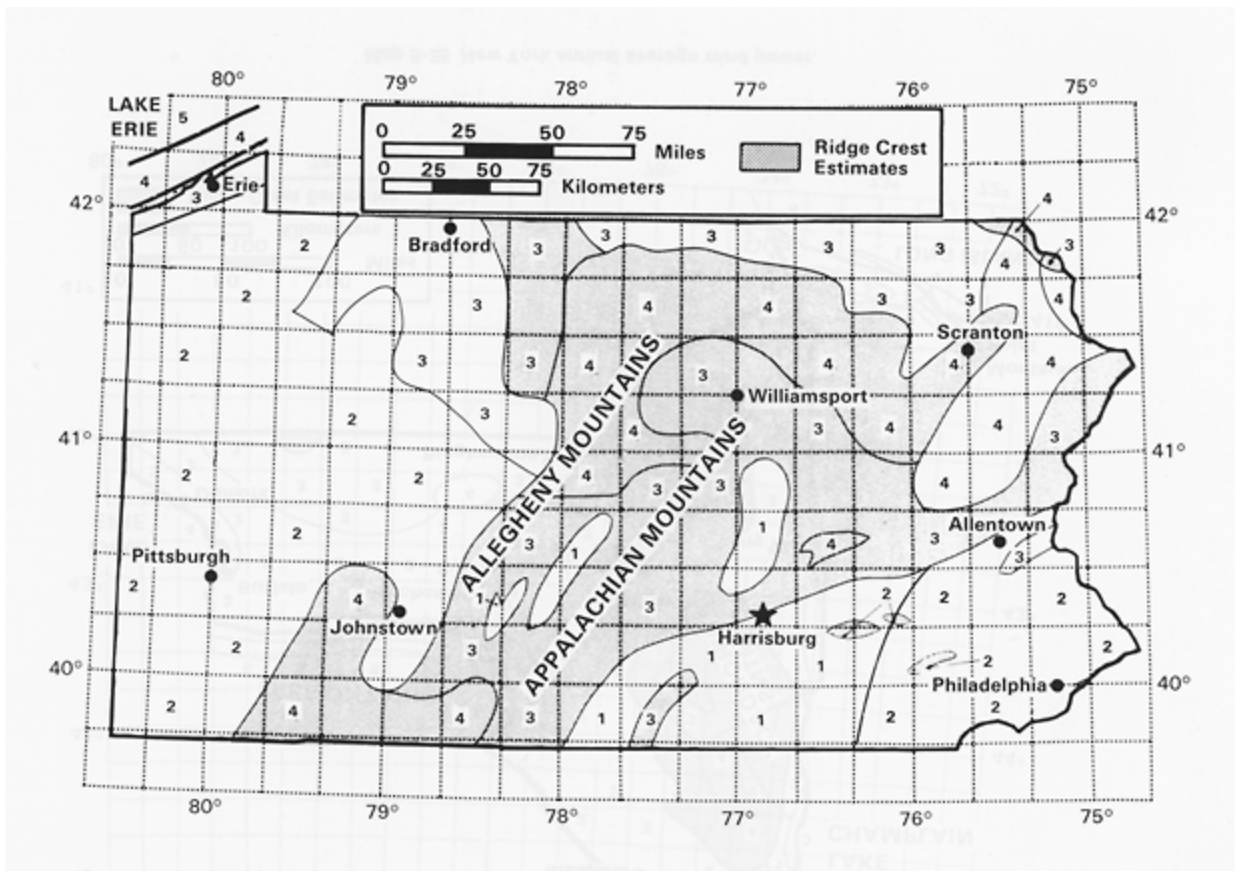


Figure 7.2 Pennsylvania WPC (Elliott, Holladay, Barchet, Foote, & Sandusky 1986)

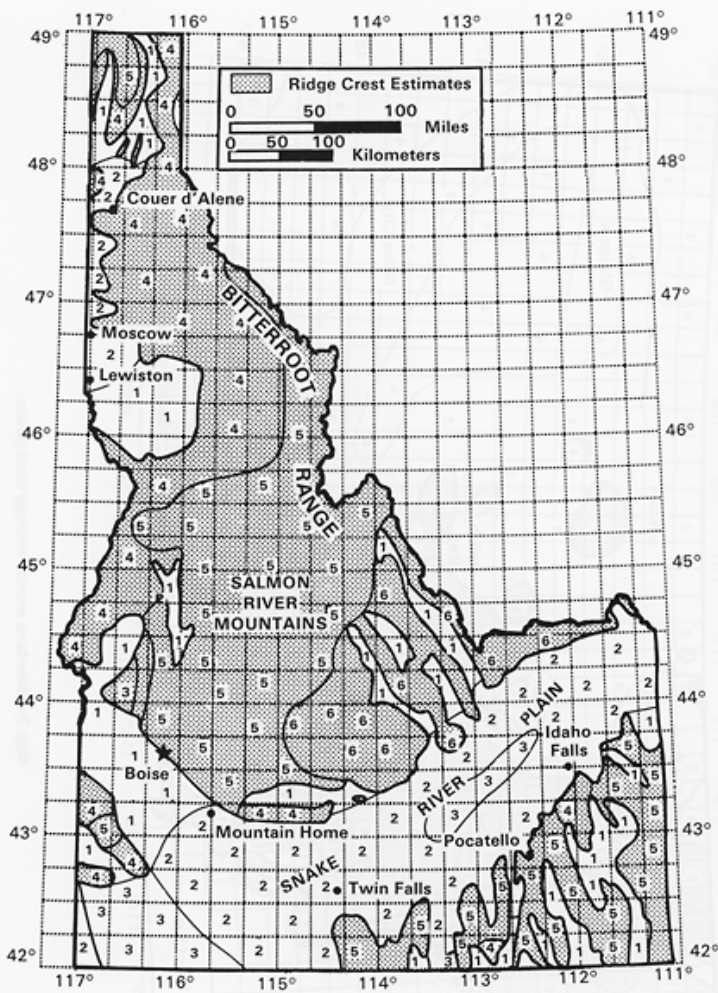


Figure 7.3 Idaho WPC (Elliott, Holladay, Barchet, Foote, & Sandusky 1986)

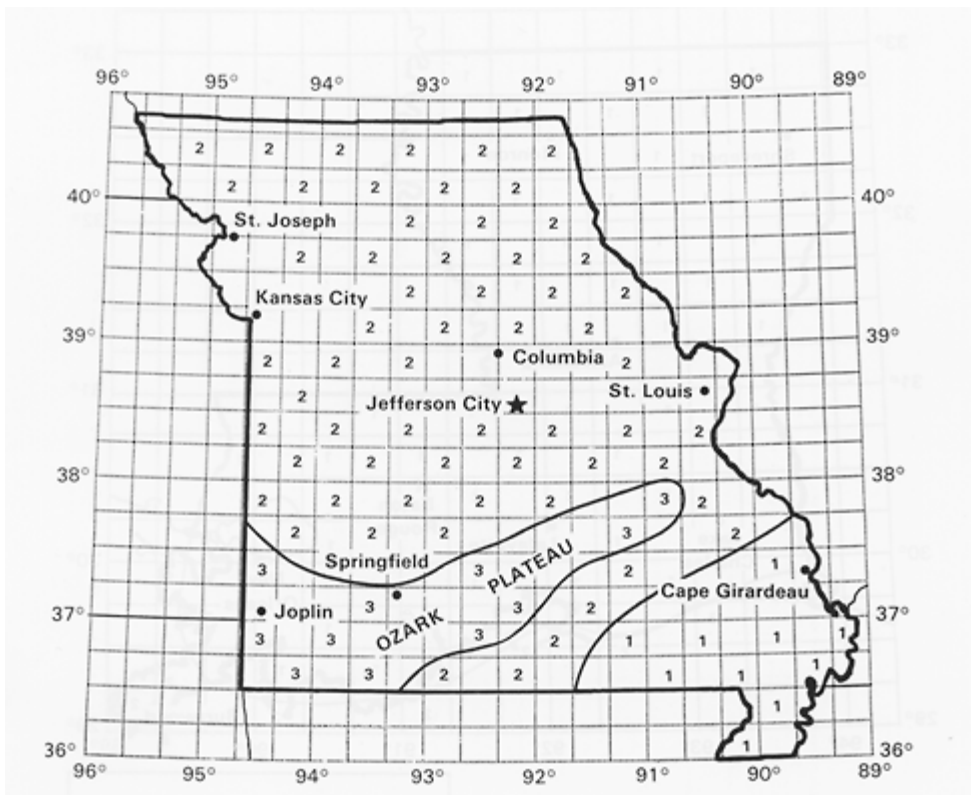


Figure 7.4 Missouri WPC (Elliott, Holladay, Barchet, Foote, & Sandusky 1986)

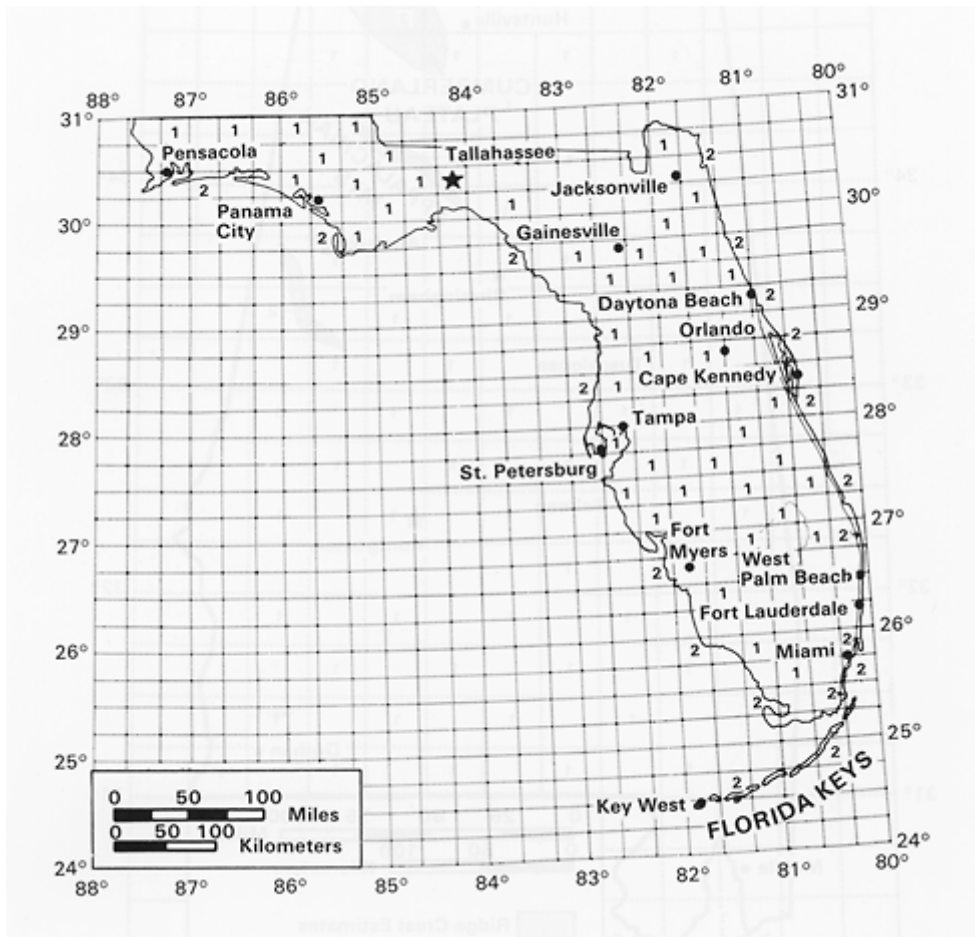


Figure 7.5 Florida WPC (Elliott, Holladay, Barchet, Foote, & Sandusky 1986)

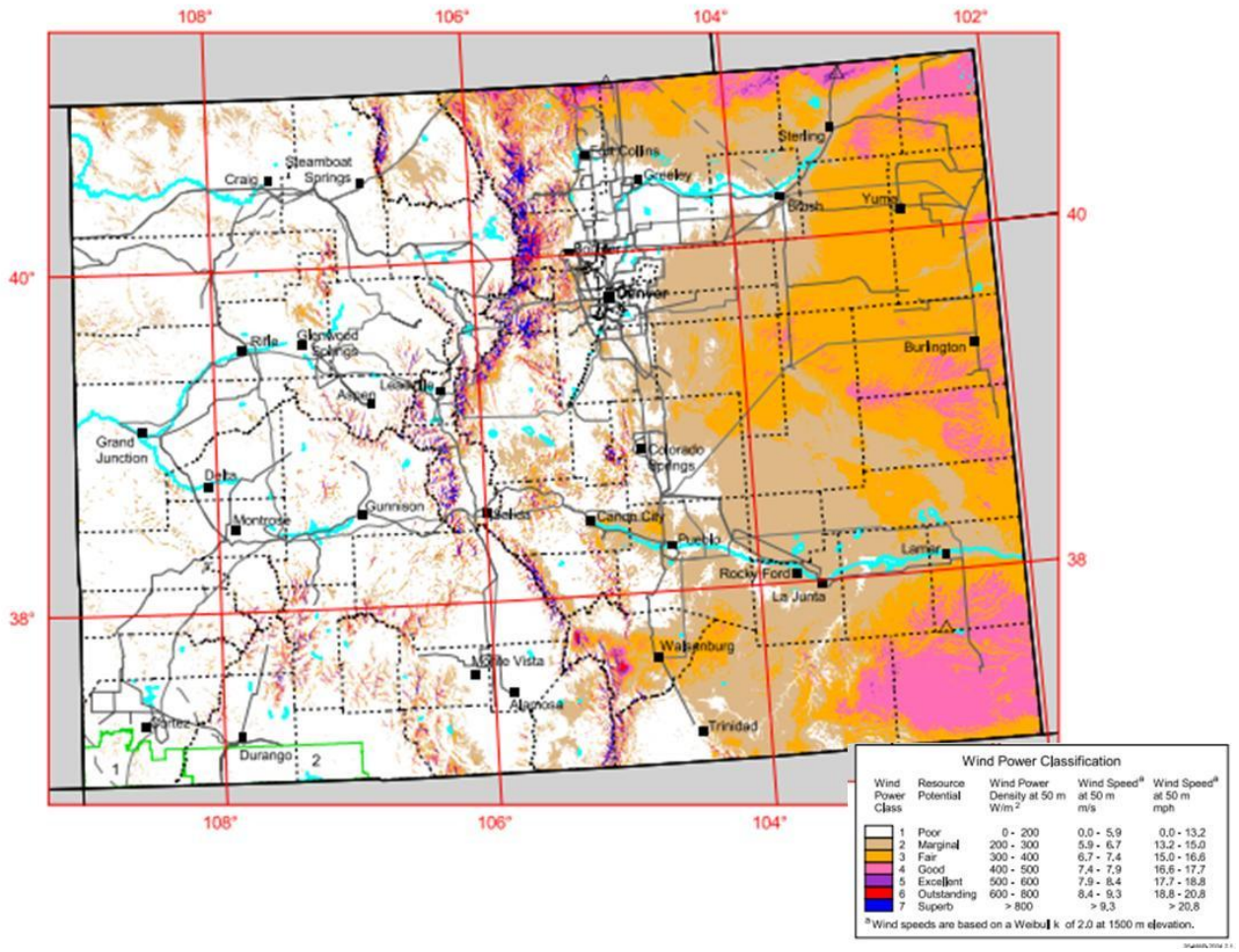


Figure 7.6 Colorado WPC (EIS, 2004)

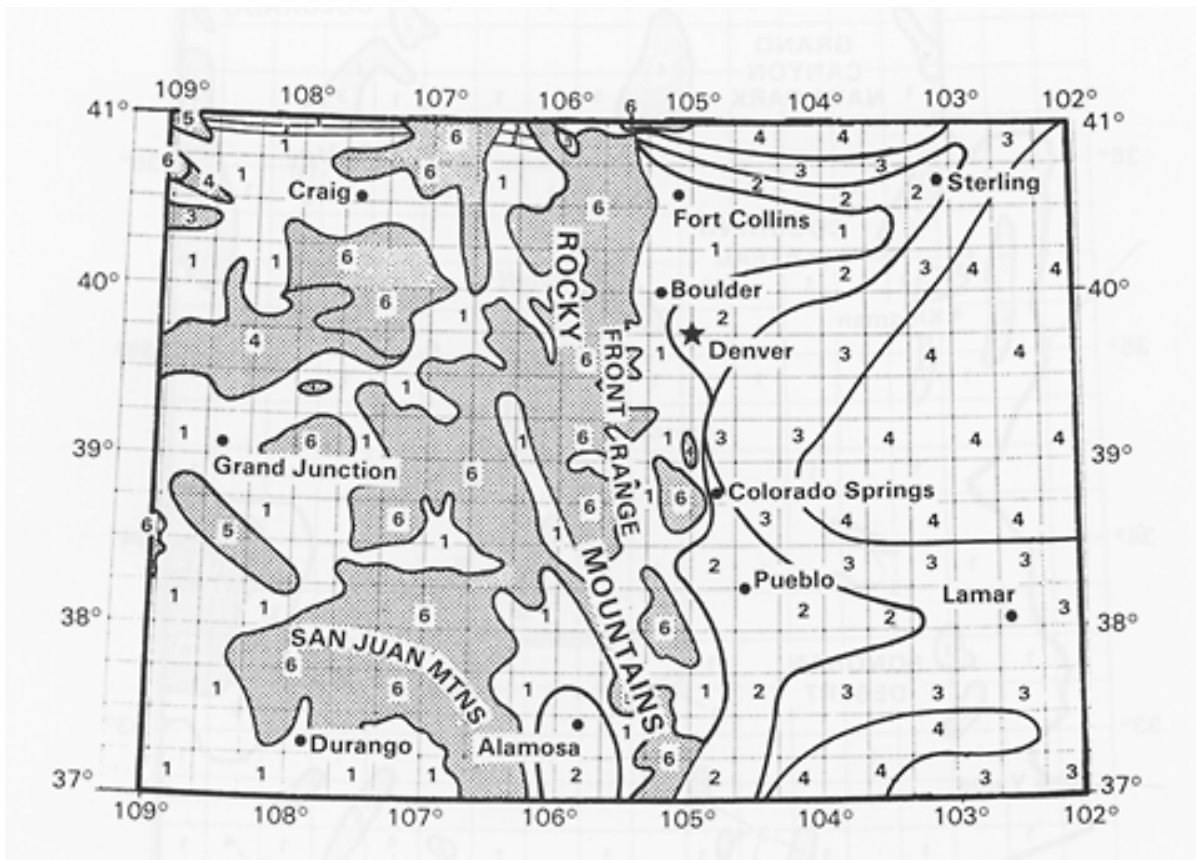
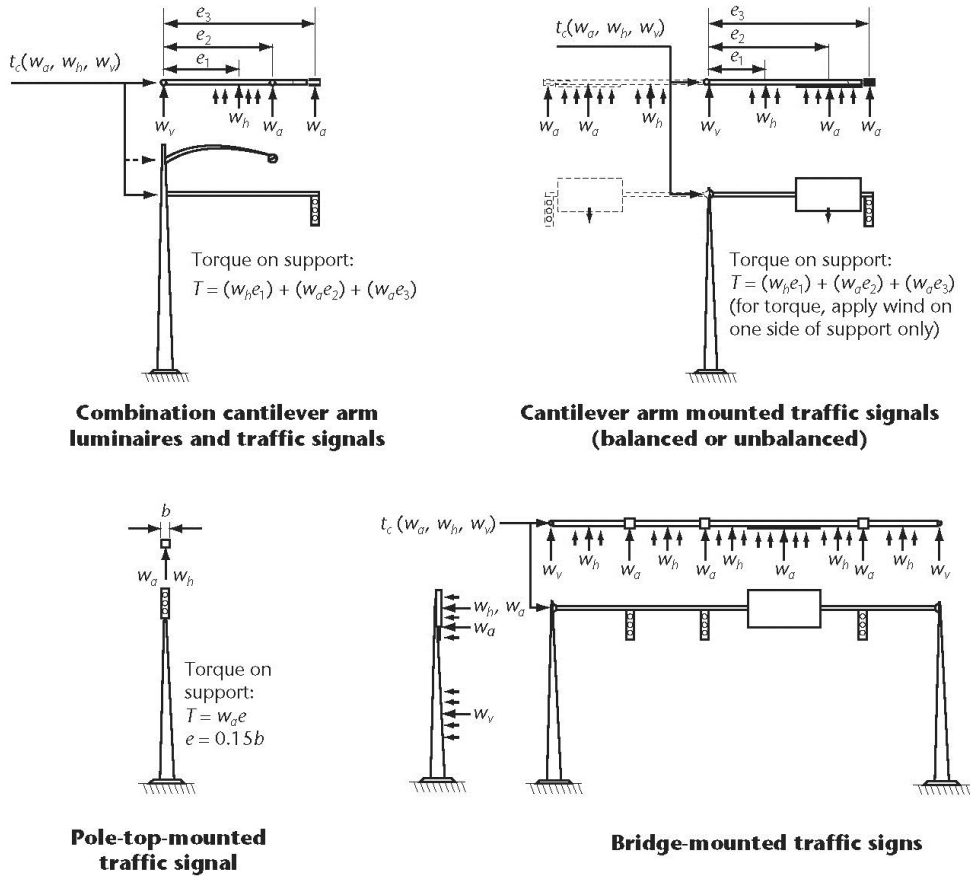


Figure 7.7 Colorado WPC (Elliott, Holladay, Barchet, Foote, & Sandusky 1986)

7.4 CSA Canadian Highway Bridge Design Code Relevant Sections



Note: Resultant wind forces are applied at the centroid of each component.

Figure A3.2.1 (Concluded)

A3.2.4 Across-wind loads

A3.2.4.1 General

The dynamic effects of across-wind loads induced by vortex shedding excitation on slender structural members shall be considered at the FLS.

The stress range shall be taken as twice the maximum stress calculated in accordance with Clause A3.2.4.3.2. The stress range limit shall be taken as that corresponding to a fatigue life of over 2 000 000 cycles for the appropriate material and detail unless a detailed fatigue damage analysis shows that a different limit is appropriate.

A3.2.4.2 Vortex shedding excitation

The significance of vortex shedding excitation for a slender structural member shall be examined in accordance with Clause A3.2.4.3 as follows:

(a) For members with a constant diameter or frontal width:

$$n_i < n_e = SV/D$$

where

n_i = natural frequency of member for mode of vibration, i , Hz

n_e = frequency at which vortex shedding occurs for a member with a constant diameter or frontal width, Hz

S = Strouhal number for the cross-sectional geometry, as specified in Table A3.2.4

V = hourly mean wind speed at the location of the member being considered, m/sec

$$= 1.24\sqrt{qC_e}$$

where

q = hourly mean reference wind pressure for the design return period, Pa

C_e = wind exposure coefficient specified in Clause 3.10.1.4

D = constant diameter or frontal width of member, m

The height above ground used to calculate C_e shall correspond to the height above ground of the location of coordinate x . The location at which n_e is calculated shall be taken as the top of the member.

(b) For members with a tapered diameter or frontal width:

$$n_i < n_e(x) = SV/D(x)$$

where

n_i = natural frequency of member for mode of vibration, i , Hz

$n_e(x)$ = frequency at which vortex shedding excitation occurs at location x for a member with a tapered diameter or frontal width, Hz

S = Strouhal number for the cross-sectional geometry, as specified in Table A3.2.4

V = hourly mean wind speed at the location of the member being considered, m/sec

$$= 1.24\sqrt{qC_e}$$

where

q = hourly mean reference wind pressure for the design return period, Pa

C_e = wind exposure coefficient specified in Clause 3.10.1.4

$D(x)$ = diameter or frontal width of a tapered member at location x , m

where

x = coordinate describing location along the member

$n_e(x)$ shall be calculated at sufficient locations along the member to determine at which locations vortex shedding excitation can occur.

Table A3.2.4
Vortex shedding data
 (See Clause A3.2.4.2.)

	S	\tilde{C}_L	B	L
Circular cross-section				
Subcritical $R_e < 3 \times 10^5$	0.18	0.50	0.10	2.5
Supercritical and transcritical $R_e \geq 3 \times 10^5$	0.25	0.20	0.30	1.0
Square cross-section	0.11	0.60	0.25	3.0
Multi-sided members and rolled structural shapes	0.15	0.60	0.25	2.75

Note: The Reynolds number, R_e , shall be calculated as $(VD/1.5) \times 10^5$.

Legend:

- B = band width, i.e., a measure of the variability of the vortex shedding frequency
 \tilde{C}_L = root-mean-square (RMS) lift coefficient for the cross-sectional geometry
 L = correlation length, i.e., the length (as a ratio of the diameter) over which the vortices act in phase
 S = Strouhal number

A3.2.4.3 Structural response to vortex shedding excitation

A3.2.4.3.1 Displacements

The magnitude of the peak member displacement, $y_i(x)$, due to vortex shedding excitation at any location, x , along the member for mode of vibration, i , shall be taken as follows:

(a) For a member with a constant diameter or frontal width:

$$y_i(x) = a_i \mu_i(x)$$

where

$y_i(x)$ = peak member displacement due to vortex shedding excitation at location x for mode of vibration, i , m

a_i = modal coefficient of magnitude of the oscillatory displacement for mode of vibration, i , for a member with a constant diameter or frontal width, m

$$= \frac{3.5 \tilde{C}_L \rho D^4 \pi^{0.25} C}{\sqrt{B \zeta_i} (4\pi S)^2 G M_i} \quad \text{if } y_i(x) \leq 0.025 D$$

$$= \frac{\sqrt{2}(\rho) \tilde{C}_L D^3 \int_0^H |\mu_i(x)| dx}{(4\pi S)^2 \zeta_i G M_i} \quad \text{if } y_i(x) > 0.025 D$$

where

$$C = \sqrt{\frac{(H/D)^2 \int_0^H x^{3\alpha} \mu_i^2(x) dx}{1 + H/2LD}} \quad \text{if } y_i(x) > 0.025 D$$

where

α = wind velocity profile exponent, taken as 0.36 for city centres and industrial areas, 0.25 for suburban and well-wooded areas, and 0.15 for open country with scattered trees

ζ_i = structural damping for the i th mode, expressed as a ratio of critical damping

GM_i = generalized mass for mode of vibration, i , kg

$$= \int_0^H m(x) \mu_i^2(x) dx$$

where

$m(x)$ = mass per unit length of member at location x , kg/m

H = length of member, m

$\mu_i(x)$ = amplitude of the member mode shape at location x for mode of vibration, i

= air mass density, taken as 1.29 kg/m³

(b) For a member with a tapered diameter or frontal width:

$$y_i(x) = a_i(x_1) \mu_i(x)$$

where

$a_i(x_1)$ = modal coefficient of magnitude of the oscillatory displacement due to vortex shedding excitation at location x_1 for mode of vibration, i , for a member with a tapered diameter or frontal width

$$= 3.5 \sqrt{\frac{2\pi L}{\zeta_i \psi(x_1)} \frac{\tilde{C}_i \rho D^4(x_1)}{(4\pi S)^2 GM_i}} |\mu_i(x_1)|$$

$$= \frac{\sqrt{2\rho} \tilde{C}_i D^2(x_1) \int_{x_1-b}^{x_1+b} D(x) |\mu_i(x)| dx}{(4\pi S)^2 \zeta_i GM_i} \quad \text{if } y_i(x) > 0.025 D(x) \text{ at any location } x$$

where

x_1 = location along a tapered member at which vortex shedding excitation is being considered

$$\psi(x_1) = \frac{dD(x_1)}{dx} + \frac{\alpha D(x_1)}{x}$$

b = length of the member above or below location x_1 for which $D(x)$ is within a certain percentage of $D(x_1)$ (the percentage shall be taken as 10% unless a smaller value can be justified)

For a tapered member, $a_i(x_1)$ shall be calculated for all locations, x_1 , along the member at which vortex shedding excitation can occur for mode of vibration, i , as determined in accordance with Clause A3.2.4.2. The largest value of $a_i(x_1)$ calculated shall be used for determining $y_i(x)$ and the peak inertia loads specified in Clause A3.2.4.3.2.

A3.2.4.3.2 Stresses

The maximum stresses in a member due to vortex shedding excitation shall be calculated by loading the member with the peak inertia loads acting statically. The magnitude of the peak inertia load per unit length at any location x along the member for mode of vibration, i , shall be taken as

$$F_i(x) = (2\pi n_i)^2 y_i(x) m(x)$$

where

$F_i(x)$ = peak inertia load at location x for mode of vibration, i , N/m

The calculation of the peak inertia loads shall take into account the mass of all components attached to the member.

A3.2.4.3.3 Damping ratios

Unless experimentally determined values are available, the value of ζ_i for members in all modes of vibration shall be taken as 0.0075 for steel and aluminum members and 0.015 for concrete members.

7.5 CSA Canadian Highway Bridge Design Commentary Relevant Sections

Annex CA3.2

Commentary on Annex A3.2 — Wind loads on highway accessory supports and slender structural elements

CA3.2.1 General

Only drag- and vortex shedding-induced loads are considered to be important for most support structures and structural elements. Nevertheless, for some exceptionally slender and flexible prismatic elements, such as ties and iced cables, galloping excitation due to negative aerodynamic damping may be important. This excitation mechanism is described in Harris and Crede (1976). The load factors for wind effects on sign support structures and structural elements are provided in Table 3.1. These load factors are less than those for bridges as given in Table 3.1, reflecting the conservatism inherent in the pressure and gust coefficients used in the design of sign support structures, as well as the less severe consequences of failure.

CA3.2.2 Horizontal drag load

Horizontal drag coefficients presented in Table A3.2.2 are adapted with some modification from AASHTO. As indicated, the drag coefficient for rounded shapes depends on the Reynolds number. The onset of critical flow conditions, leading to reduced values of C_h for cylindrical shapes, occurs from $D(qC_e)^{0.5} = 3.6$. This corresponds to the Reynolds number of 3×10^5 .

The values of C_h provided for truss-type supports are most applicable for solidity ratios (defined as the ratio of exposed frontal area to gross frontal area) from approximately 0.2 to 0.3. For higher solidity ratios, these values are conservative. For solidity ratios of less than 0.2, use should be made of experimental data (Cohen 1960) or, alternatively, the overall drag should be taken as the sum of the loads on individual members. An allowance for shielding, as indicated in Table C3.6, is appropriate.

Horizontal drag coefficients for members, sign panels, barriers, and other shapes not included in Table A3.2.2 may, in accordance with Clause 3.10.1.7, be established from representative wind tunnel tests in which comparative tests are made on similar shapes included in this table. For free-swinging traffic signals, wind loads calculated using the drag coefficient given in Table A3.2.2 may be modified on the basis of experimental data.

CA3.2.3 Horizontal drag on highway accessory supports

The provisions of Clause A3.2.3 have been adapted from AASHTO. The wind loads W_a , W_h , W_p , and W_v for components of the structure are obtained by multiplying F_h calculated in Clause 3.10.2.2 by the exposed frontal area of the respective component. The ice accretion load to be used in combination with that of wind is prescribed in Clause 3.12.6.

CA3.2.4 Across-wind loads

CA3.2.4.1 General

When the wind blows across a slender structural member, vortices are shed alternately from one side and then the other, giving rise to a fluctuating force acting at right angles to the wind direction. This organized pattern of vortices is referred to as the von Karman vortex street. A structural member may be considered slender in this context if the aspect ratio exceeds 20. For lightly damped members, which are free to oscillate, large amplitude vibrations in the plane normal to the wind may develop when the vortex shedding is in resonance with one of the natural frequencies of vibration. Although this is most likely to occur for the lower modes of vibration, vortex shedding induced effects for very flexible members may also be important for higher modes. The character of the vortex shedding forces for circular cylinders

depends on the Reynolds number, $Re = VD/\nu$, where ν is the kinematic viscosity. The shedding tends to be organized at subcritical and transcritical Reynolds numbers (Davenport *et al.*, Harris and Crede 1976). In the critical range, namely for $3 \times 10^5 \leq Re \leq 3 \times 10^6$, vortex shedding tends to be irregular unless the structural motion is sufficiently large to organize the fluctuating flow around the body. This phenomenon, referred to as "locking in", becomes important for lightly damped members.

Although nearly periodic in a smooth airstream, vortex shedding in turbulent boundary layer flow conditions that are characteristic of natural wind tends to become less regular, with energy distributed over a band of frequencies around n_e . The presence of turbulence effectively reduces the extent of the member over which the vortex shedding forces remain correlated (Davenport *et al.*, Harris and Crede 1976, Vickery 1968, 1972). A reduction of the aspect ratio has somewhat similar effects (Vickery 1968).

Several measures that may be considered should vortex shedding induced effects prove to be excessive. These include

- (a) strengthening and/or stiffening the member;
- (b) increasing the mass;
- (c) increasing the damping; and
- (d) changing the aerodynamic characteristics by, e.g., increasing the taper or adding aerodynamic spoilers.

Of these alternatives, increasing the damping of the member is the most desirable solution. The effective damping can be increased using visco-elastic materials or special dynamic absorbers (Harris and Crede 1976).

CA3.2.4.2 Vortex shedding excitation

The excitation due to vortex shedding is treated as a time-varying load of frequency $n_e = SV/D$. Resonant vibrations are assumed to occur when the frequency of vortex shedding coincides with a natural frequency of the member. The evaluation of vortex shedding-induced effects requires a dynamic analysis of the member to determine its natural frequencies and associated mode shapes of vibration. All modes of vibration for which vortex shedding-induced resonant vibrations occur at wind speeds equal to or less than that corresponding to the design mean hourly reference wind pressure, namely, $V \leq 1.24 (qC_e)^{0.5}$, must be considered. In the case of a member with a constant cross-section, resonant vibrations for a particular mode of vibration with natural frequency, n_i , occur at a specific or critical wind speed, namely, $V_{cr} = D n_i/S$. In the case of a tapered member, the frequency of vortex shedding at a particular wind speed varies over the length of the member. As the wind speed increases, resonant excitation occurs first at the smaller diameter portion of the member and then shifts to portions with larger diameter. Consequently, vortex shedding effects associated with a particular mode of vibration with frequency, n_i must be examined for a range of critical wind speeds. Defining D_{min} and D_{max} as the minimum and maximum cross-sectional dimensions, respectively, this range is expressed as

$$\frac{n_i D_{min}}{S} \leq V_{cr} \leq \frac{n_i D_{max}}{S}$$

CA3.2.4.3 Structural response to vortex shedding excitation

For the harmonic sinusoidal model, the RMS (root-mean-square) time-varying vortex shedding induced load acting at a particular location, x , along a member is expressed as

$$F_s(x, t) = (1/2) \rho V^2 \tilde{C}_l D(x) \sin[2\pi n_e(x) t]$$

where

- ρ = air mass density, taken as 1.29 kg/m³
- V = the mean wind speed at location x , m/sec
- \tilde{C}_l = RMS lift (across-wind) force coefficient for the cross-sectional geometry as specified in Table A3.2.4

- x = coordinate describing length along the member
 $D(x)$ = the diameter or frontal width of a member at location x , m
 $n_e(x)$ = frequency at which vortex shedding occurs at location x , Hz
 t = time, s

For members of constant diameter or frontal width, the magnitude of the excitation is taken to be invariant with x and proportional to the velocity pressure at the top of the member. This is a conservative assumption since V approaches zero at ground level. It is also conservative to treat $F_s(x,t)$ as a spatially coherent excitation, that is, acting in phase along the entire length of the member (Figure CA3.2.1 (a)). In reality, this begins to occur only at large amplitudes of motion.

The variation of the wind speed with height, the turbulent flow functions normally experienced, and the presence of signs and other accessories all tend to disrupt the spatial correlation of the excitation.

For structures with varying diameter or frontal width, the magnitude of the excitation will vary along the length of the member. The vortex shedding excitation at location x_1 is taken to remain in phase over the portion of the member for which the diameter or frontal width remains within $\pm \Omega$ percent of $D(x_1)$ and is taken to be zero over the remainder of the member (Figure CA3.2.1 (b)). A default value of $\Omega = \pm 10\%$ is prescribed in Clause A3.2.4.3.1, which is higher than the value of $\Omega = \pm 5\%$ prescribed in the *National Building Code of Canada* (NBC 1980) for tapered chimney stacks, observation towers, and buildings. This is because the majority of members covered by Clause A3.2.4 fall into the subcritical R_e range, which leads to a somewhat longer correlation length in comparison with that of members covered by the NBC.

The value of $\Omega = \pm 10\%$ is applicable for peak response amplitudes greater than 2% of D .

For a band limited random forcing model with a Gaussian load spectrum, the induced load is described in references (Davenport *et al.*, Harris and Crede 1976, Vickery and Clark 1972). The band limited random forcing model differs from the sinusoidal model by

- (a) allowing for a random (rather than harmonic) vortex lift force. This employs a different forcing function than the sinusoidal model;
- (b) allowing for the energy associated with the vortex shedding to be distributed about the dominant frequency (rather than concentrated on the dominant frequency). This employs a bandwidth term, B , which is a measure of the distribution of the energy;
- (c) allowing for the three-dimensional nature of the flow — the loss of correlation of the lift forces along the length of the member. This employs a term for the correlation length, L , which is a measure of the length, in diameters, that the vortices remain correlated (in phase);
- (d) allowing for the turbulence of natural wind (turbulence leads to a reduction in the vortex shedding correlation length and leads to a small reduction in the strength of the shedding forces); and
- (e) allowing for the variation of wind speed with height. This employs the power law wind-velocity-profile-exponent, α_s to obtain an apparent taper between the wind and the member.

Treating vortex shedding as a sinusoidal process is an approximation leading to conservative estimates. The variation of the wind speed with height, turbulence of the natural wind, and the presence of signs and other accessories all tend to disrupt the spatial correlation of the excitation. It is generally accepted as more accurate to treat the excitation as a band-limited random process and to assume that the forcing tends to become harmonic only when the motion of the member is sufficiently large to organize the shedding of vortices (Davenport *et al.*, Harris and Crede 1976, Vickery and Clark 1972, Wootton 1969). This tends to occur when the peak amplitude of the motion is of the order of 2.0% to 2.5% of the diameter or the width of the cross-section, and greater.

For the evaluation of the vortex shedding-induced response in a particular mode of vibration, the direction of the vortex shedding excitation at any location, x , is taken in the direction of the motion of the member at that location. This is a simplification, as the direction of the vortex shedding force at large body amplitudes is more likely to be in the direction of the local time derivative or velocity of the body motion. For the purpose of evaluating the generalized force, GF_i , associated with a particular mode of vibration, both assumptions lead to the same RMS and peak values. Typical illustrations are presented in Figure CA3.2.1.

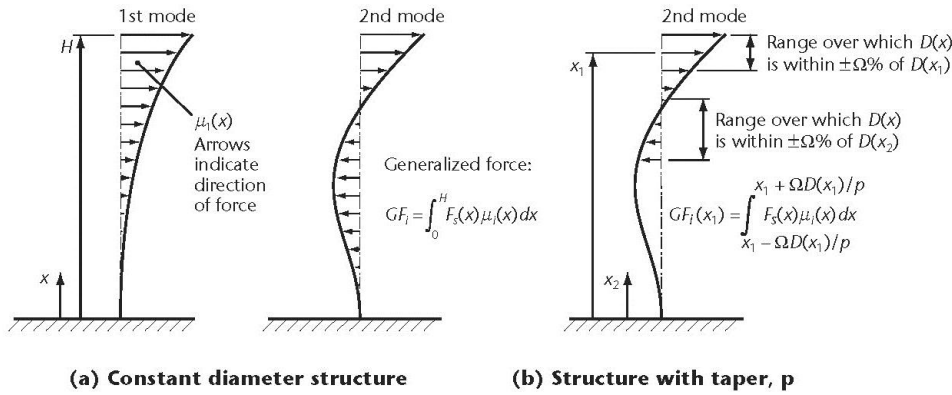


Figure CA3.2.1
Typical vortex shedding-induced responses in two modes of vibration

The designer should follow a more rigorous analysis or consider representative wind tunnel model tests in cases where vortex shedding effects, computed on the above prescribed basis, govern the design.

CA3.2.4.3.1 Displacements

The maximum displacements of the member due to the excitation described in this Clause are determined from a steady-state forced vibration analysis. This analysis is carried out by examining the vortex shedding-induced response associated with the various modes of vibration of the member. Following this approach, the peak displacement of a member at location x oscillating sinusoidally in its i th mode of vibration is expressed as

$$y_i(x) = a_i \mu_i(x)$$

where

a_i = modal coefficient of magnitude of the oscillatory displacement for mode of vibration, i , m

$\mu_i(x)$ = amplitude of the member mode shape at location x for mode of vibration, i

The modal coefficient a_i contains a peak factor of $\sqrt{2}$ for sinusoidal forcing and 3.5 for band limited random forcing (Davenport *et al.*).

The peak factor is defined as the ratio of the peak response to the RMS response. For sinusoidal forcing, the variability in the shedding of the vortices is caused by the unsteadiness of the wake of the member and the movement of the structure itself. For band-limited random forcing, the variability in the shedding of the vortices also includes the unsteadiness of the oncoming flow due to turbulence and gusts in the wind.

For both constant diameter and tapered members, peak displacements are first calculated using the band-limited random forcing model. If the peak displacements calculated are in excess of 2.5% of the diameter at the location of vortex shedding excitation (a limit of 0.7% of the RMS displacements is multiplied by a peak factor of 3.5 to obtain the 2.5% figure [Davenport *et al.*]), then the amplitudes are sufficiently large to cause "locking-in" and the sinusoidal model should be used.

In the evaluation of a_i for a member with a constant D , the integration of $\mu_i(x)$ is over the entire length of the member. The absolute value of $\mu_i(x)$ is used, since the vortex shedding force at location x is in the same direction as $\mu_i(x)$.

In the case of a member with varying D , a_i is no longer single valued but depends on the location along the member at which the frequency of vortex shedding excitation for a certain wind speed coincides with n_i . Consequently, a_i must be determined for all locations along the member at which

vortex shedding excitation can occur as determined by Clause A3.2.4.2. The maximum value of a_i will produce the most severe force effects for the i th mode of vibration. In the case of a detailed fatigue analysis, however, contributions to fatigue damage for the entire range of a_i each associated with a different wind speed, namely $V = n_i D(x)/S$, must be considered.

For sinusoidal forcing, the integration required for the evaluation of a_i at a particular location $x = x_1$ is carried out over the part of the member for which $D(x)$ is within $\pm\Omega$ percent of D at $x = x_1$. In the case of a member with a uniform taper, p , the indicated limits of integration become

$$x_1 + b = x_1 + \frac{\Omega D(x_1)}{p} \quad \text{and} \quad x_1 - b = x_1 - \frac{\Omega D(x_1)}{p}$$

In the case of a nonuniformly tapered member, the local variation of D around $x = x_1$ can be approximated by a linear taper p .

A good approximation for tapered members is to neglect the variation of D over the limits of integration. With this assumption the modal coefficient for a member with a taper p for the i th mode becomes

$$a_i(x_1) = \frac{2\sqrt{2}\Omega p \tilde{C}_L D^4(x_1)}{\rho(4\pi S)^2 \zeta_i G M_i} |\mu|_{ave}$$

where

$$G M_i = \int_0^H m(x) \mu_i^2(x) dx$$

and $|\mu|_{ave}$ is the average of the absolute values of the mode shape over the portion of the member centred on x_1 , for which $D(x)$ is within $\pm\Omega$ percent of $D(x_1)$. Except near the node points, which do not contribute to maximum values, $|\mu|_{ave} \propto |\mu(x_1)|$.

The location along the member leading to the maximum value of $a_i(x)$ for mode, i , can be found from

$$\frac{d}{dx} a_i(x) = \frac{d}{dx} [D^4(x) \mu(x)] = 0$$

For a free-standing tapered member, the region of maximum excitation for the fundamental mode is at approximately three-quarters of the height and moves downward for higher modes of vibration.

Although the evaluation of a_i for a particular mode of vibration must be carried out over the entire member, the response is normally governed by the excitation from its main components. For example, in the case of lighting standards, the response in particular modes of vibration is dominated by shedding from the pole, with the excitation on the luminaire bracket being of far lesser significance. As a good first approximation, the evaluation of the various modal coefficients can thus be confined to locations along the pole.

CA3.2.4.3.2 Stresses

Although smaller diameter components of the member, typically luminaire brackets, may be neglected in the evaluation of the maximum value of the modal coefficient, a_i , for a particular mode of vibration, such components must be included in the evaluation of $F_i(x)$.

References

Other publications

Associate Committee on the National Building Code of Canada. 1980. Chapter 4 of the *Supplement to the National Building Code of Canada*. NRC No. 17724.

- Cohen, E. 1960. "Wind Loads on Towers." *Meteorological Monographs*, Vol. 4, No. 22.
- Davenport, A.G. *et al.* "New Approaches to Design Against Wind Action." Unpublished Text. Boundary Layer Wind Tunnel Laboratory, University of Western Ontario, London, Ontario.
- Harris, Cyril, M., and Crede, Charles, E. 1976. *Shock and Vibration Handbook*. Section 29, "Vibration of Structures Induced by Wind," Part II, 2nd Edition, McGraw-Hill Book Co.
- Vickery, B.J. 1968. "Load Fluctuations in Turbulent Flow." *ASCE, Journal Eng. Mech. Div.*, Vol. 94, February.
- Vickery, B.J., and Clark, A.W. 1972. "Lift of Across Wind Response of Tapered Stacks." *ASCE, Journal Struct. Div.*, Vol. 98, January.
- Wootton, L.R. 1969. "The Oscillation of Large Circular Stacks in Wind." *Proceedings I.C.E.*, August.